

TAX1BP3 Loss Is an Autosomal Recessive Cause of Arrhythmogenic Cardiomyopathy and
TRPV4-mediated Arrhythmogenesis

by

Robin Morgan Perelli

Department of Cell Biology
Duke University

Defense Date: October 11, 2024

Approved:

Andrew Landstrom, Advisor

Christopher Nicchitta, Co-Chair

Howard Rockman, Co-Chair

Nenad Bursac

Amy Bejsovec

Dissertation submitted in partial fulfillment of the requirements for the degree of Doctor
of Philosophy in the Department of Cell Biology in The Graduate School of
Duke University
2024

ABSTRACT

TAX1BP3 loss is an autosomal recessive cause of arrhythmogenic cardiomyopathy and TRPV4-mediated arrhythmogenesis

by

Robin Morgan Perelli

Department of Cell Biology
Duke University

Defense Date: October 11, 2024

Approved:

Andrew Landstrom, Advisor

Christopher Nicchitta, Co-Chair

Howard Rockman, Co-Chair

Nenad Bursac

Amy Bejsovec

An abstract of a dissertation submitted in partial fulfillment of the requirements for the degree of
Doctor of Philosophy in the Department of Cell Biology in The Graduate School of
Duke University
2024

Copyright by
Robin Perelli
2024

Abstract

Arrhythmogenic cardiomyopathy (ACM) is one of the leading causes of sudden cardiac death in children and is characterized by the fibrofatty replacement of the myocardium, predominantly of the right ventricle. Sixty percent of patients with ACM have a known genetic cause, but for the remainder, the etiology is unknown. This lack of mechanistic understanding has slowed development of disease-modifying therapies, and children with ACM have a high degree of morbidity and mortality. We identified a kindred with multiple members affected by ACM co-segregating with biallelic variants in the gene *TAX1BP3*, which encodes tax1-binding protein 3 (TAX1BP3). iPSC-CMs derived from this kindred demonstrated increased intracellular lipid droplets, increased transient receptor potential vanilloid type 4 (*TRPV4*) expression, and inducible TRPV4 current. This was associated with a change in TRPV4 trafficking, depletion of the intracellular sarcoplasmic reticulum Ca^{2+} store and increased ryanodine receptor 2 (RyR2)-mediated store Ca^{2+} leak and delayed afterdepolarizations—a known mechanism of Ca^{2+} -mediated arrhythmogenesis. Similarly, *Tax1bp3* cardiac-specific knockout mice had increased Ca^{2+} leak and were predisposed to ventricular arrhythmias compared with control mice. Ca^{2+} leak in both the iPSC-CMs and isolated mouse ventricular myocytes was rescued by small molecule TRPV4 inhibition. This strategy also effectively reduced Ca^{2+} leak in a Plakophilin 2 (PKP2) p.His773AlafsX8 iPSC-CM model of ACM. We conclude that TAX1BP3 is associated with rare autosomal recessive ACM through TRPV4-mediated Ca^{2+} leak from RyR2. Further, TRPV4 current inhibition has the potential to be a new therapeutic target for ACM.

Lastly, in order to more effectively test potential therapeutics *in vivo*, we sought to develop an animal model with a higher phenotypic penetrance. Because exercise is a risk factor for arrhythmia induction and can accelerate ACM disease progression, we chose to develop an exercise model with the *Tax1bp3*^{-/-} mice. We found that consistent swimming exercise over a

period of 6 weeks increased the percentage of mice with inducible ventricular tachycardia but did not cause cardiac remodeling. Since ACM is characterized by an arrhythmogenic phase that precedes fibrofatty infiltration, this mouse model could serve as a means of studying the effects of exercise on electrical remodeling and the early stages of ACM.

In summary, this dissertation describes 1) the identification of a novel gene associated with ACM, *TAX1BP3*, 2) the development of new *in vitro* and *in vivo* ACM models and 3) identifies a new potential ACM disease mechanism: calcium leak that is mediated by TRPV4. These findings implicate TRPV4 inhibition as a possible treatment for ACM—a deadly disease with limited therapies.

Contents

Abstract.....	iv
List of Tables	ix
List of Figures.....	x
List of Abbreviations	xii
Acknowledgements.....	xiv
1. Introduction	1
2. Materials and Methods	3
2.1 Clinical and human genetic methods	3
2.1.1 Clinical evaluation	3
2.1.2 Exome sequencing	3
2.1.3 Chromosomal microarray analysis.....	4
2.1.4 Sequence homology and domain mapping	4
2.1.5 RT-qPCR.....	4
2.1.6 In silico variant pathogenicity modeling.....	5
2.2 Induced pluripotent stem cell methods	5
2.2.1 Peripheral blood mononuclear cell proliferation	5
2.2.2 Generation of iPSCs.....	6
2.2.3 iPSC culture and differentiation of cardiomyocytes	6
2.2.4 Fat accumulation in iPSC-CMs.....	7
2.2.5 Western blot.....	7
2.2.5 Immunofluorescence (IF).....	8
2.2.6 Lentiviral overexpression of TAX1BP3	9

2.2.7 Patch clamp.....	9
2.2.8 RNA-sequencing.....	10
2.3 Tax1bp3 knockout mouse methods.....	11
2.3.1 Generation of Tax1bp3 knockout mouse.....	11
2.3.2 Mouse experimental design.....	11
2.3.3 Ventricular myocyte isolation.....	12
2.3.4 Immunofluorescence.....	12
2.3.5 Echocardiography.....	13
2.3.6 Histology.....	13
2.3.7 Mouse intracardiac electrophysiology.....	14
2.3.8 Mouse swimming.....	15
2.4 Ca ²⁺ imaging and analysis.....	15
2.5 Statistical analysis.....	16
3. TAX1BP3 is associated with autosomal recessive pediatric-onset ACM.....	18
3.1 Clinical evaluation.....	18
3.2 Genetic evaluation.....	23
4. Novel iPSC-CM model of arrhythmogenic cardiomyopathy.....	30
4.1 Generation of iPSC-CM ^{M78T/del}	30
4.2 iPSC-CM ^{M78T/del} have increased intracellular lipid droplet accumulation.....	33
4.3 iPSC-CM ^{M78T/del} demonstrates pro-arrhythmogenic Ca ²⁺ leak from the sarcoplasmic reticulum.....	35
5. Inducible, cardiac-specific Tax1bp3 knockout mouse model.....	46
5.1 Inducible, cardiac-specific Tax1bp3 knockout mice have increased Ca ²⁺ leak and ventricular arrhythmias.....	46

6. TRPV4 current is activated in iPSC-CM ^{M78T/del} and changes localization	55
6.1 TRPV4 current is activated in iPSC-CM ^{M78T/del}	55
6.2 TRPV4 localizes to the dyad in Tax1bp3 ^{-/-} mice	56
7. Small molecule TRPV4 inhibition rescues Ca ²⁺ leak in vitro and in vivo	60
7.2 Ca ²⁺ leak and delayed afterdepolarizations can be suppressed by TRPV4 inhibition	60
7.3 TRPV4 inhibition rescues Ca ²⁺ leak in Tax1bp3 ^{-/-} mice	62
8. TRPV4 inhibition reduces Ca ²⁺ leak in iPSC-CMs derived from a PKP2-positive ACM donor	64
9. Development of a novel arrhythmogenic exercise mouse model	69
10. Conclusions and future directions	76
References.....	81
Biography	93

List of Tables

Table 1: Kindred clinical and genetic information	26
Table 2: In silico variant prediction aggregate analysis of the TAX1BP3-M78T variant.....	29
Table 3: Canonical Wnt signaling mRNA expression in iPSC-CM RNA-sequencing	56
Table 4: Mouse swimming schedule	71

List of Figures

Figure 1: Pedigree of TAX1BP3 M78T/del Kindred	19
Figure 2: Clinical evaluation by cardiac MRI	20
Figure 3: Additional Cardiac MRI imaging.....	21
Figure 4: ECG Evaluation	22
Figure 5: ECG with ventricular tachycardia.....	23
Figure 6: TAX1BP3 variant locations	25
Figure 7: CMA findings demonstrating loss of <i>TAX1BP3</i> heterozygosity.....	26
Figure 8: Sanger sequencing validation and <i>TAX1BP3</i> expression.....	28
Figure 9: Validation of iPSCs.....	31
Figure 10: Validation of iPSC-CMs	32
Figure 11: Reduced TAX1BP3 protein expression in iPSC-CM ^{M78T/del}	33
Figure 12: Lipid accumulations in fat-stressed iPSC-CMs	34
Figure 13: RNA expression in fat-stressed iPSC-CMs	35
Figure 14: iPSC-CM ^{M78T/del} have differences in Ca ²⁺ handling.....	38
Figure 15: No change in NCX, SERCA2a, PLN, or p-PLN protein expression or SERCA and NCX activities	40
Figure 16: iPSC-CM ^{M78T/del} have greater Ca ²⁺ leak.....	41
Figure 17: iPSC-CM ^{M78T/del} have spontaneous Ca ²⁺ release and inducible sustained cellular arrhythmias	42
Figure 18: TAX1BP3 lentivirus overexpression in iPSC-CM ^{M78T/del}	44
Figure 19: TAX1BP3 overexpression rescues Ca ²⁺ leak.....	45
Figure 20: Generation of <i>Tax1bp3</i> ^{-/-} mice	47

Figure 21: Full Western blot of Tax1bp3 reduced ventricular protein expression in <i>Tax1bp3</i> ^{-/-} mice	48
Figure 22: <i>Tax1bp3</i> ^{-/-} mouse transthoracic echocardiograms demonstrate no differences compared to controls.....	49
Figure 23: <i>Tax1bp3</i> ^{-/-} mouse histology demonstrates no significant differences compared to controls.	50
Figure 24: <i>Tax1bp3</i> ^{-/-} have increased Ca ²⁺ leak	51
Figure 25: Ca ²⁺ transient dynamics in <i>Tax1bp3</i> ^{-/-} mice.....	52
Figure 26: Electrocardiograms in <i>Tax1bp3</i> ^{-/-} mice demonstrate no differences compared to controls	53
Figure 27: <i>Tax1bp3</i> ^{-/-} mice have increased inducible ventricular tachycardia	54
Figure 28: Increased TRPV4 activity in iPSC-CM ^{M78T/del}	57
Figure 29: TRPV4 localization changes in iPSC-CM ^{M78T/del}	58
Figure 30: Trpv4 localization changes in <i>Tax1bp3</i> ^{-/-} mice	59
Figure 31: TRPV4 inhibition with HC-067047 rescues Ca ²⁺ leak and DADs	63
Figure 32: TRPV4 inhibition rescues Ca ²⁺ leak in <i>Tax1bp3</i> ^{-/-} mice.....	62
Figure 33: Figure 34: PKP2-fs iPSC and iPSC-CM validation.....	66
Figure 34: TRPV4 inhibition rescues Ca ²⁺ leak in PKP2-fs iPSC-CMs	67
Figure 35: Proposed mechanism of TAX1BP3-mediated arrhythmia development.....	68
Figure 36: <i>Tax1bp3</i> ^{-/-} exercise study design	70
Figure 37: Swimming exercise tolerance	71
Figure 38: Transthoracic echocardiograms before and after swimming	72
Figure 39: Surface ECGs after swimming.....	73
Figure 40: <i>Tax1bp3</i> ^{-/-} mice have increased ventricular tachycardia with swimming exercise.....	74

List of Abbreviations

ACM: arrhythmogenic cardiomyopathy

AVERP: AV node effective refractory period

BSA: Bovine serum albumin

CMA: Chromosomal microarray analysis

CMRI: Cardiac magnetic resonance imaging

CNV: Copy number variation

DADs: Delayed afterdepolarizations

DMSO: Dimethyl sulfoxide

DSP: Desmoplakin

ECG: Electrocardiogram

EF: Ejection fraction

ES: Exome sequencing

EP: Electrophysiology

FBS: Fetal bovine serum

GAPDH: Glyceraldehyde 3-phosphate dehydrogenase

HRP: Horseradish peroxidase

IPSCs: induced pluripotent stem cells

IPSC-CMs: induced pluripotent stem cell-derived cardiomyocytes

LTCC: L-type calcium channel

LV: Left ventricle

NCX: Sodium calcium exchanger

PBMCs: Peripheral blood mononuclear cells

PBS: Phosphate-buffered saline

PFA: Paraformaldehyde

PKP2: Plakophilin 2

PVC: Premature ventricular complex

RV: Right ventricle

RYR2: Ryanodine receptor 2

SERCA2A: Sarcoplasmic/endoplasmic reticulum Ca²⁺-ATPase

SR: Sarcoplasmic reticulum

SRE: Spontaneous release event

SNRT: Sinus node recovery time

TAX1BP3: Tax1-binding protein 3

TNNT2: Cardiac troponin T

TRPV4: Transient receptor potential vanilloid 4

UDN: Undiagnosed diseases network

VT: Ventricular Tachycardia

WT: Wild type

Acknowledgements

I gratefully acknowledge the support of the patients and family members that agreed to participate in this study. I thank the Duke University School of Medicine for the use of the Sequencing and Genomic Technologies Core Facility, which provided RNA-sequencing services; for the use of the Duke Cardiovascular Research Center core, which provided mouse echocardiography and measurements, and for the use of the Duke Light Microscopy Core, which provided the Zeiss Axio Imager Z2 Upright Microscope for brightfield imaging. I thank Maik Dahlhoff for providing the mutant mouse/ line ($Tax1bp3^{tm1c(EUCOMM)Hmgu}$), the European Mouse Mutant Archive (EMMA), and the University of Veterinary Medicine, Vienna, Austria, from which the mouse line was distributed (EM:13461). Biorender software was also used for making the model figure.

I thank the following individuals for their contributions to this work: Heidi Cope, Enya R. Dewars, Alexander S. Behura, Anna Q. Ponck, Angelina M. Sala, Zhushan Zhang, Mary E. Moya-Mendez, Amy Berkman, Gabrielle G. Monaco, Molly C. Sullivan, Jordan E. Ezekian, Qixin Yang, Bo Sun, Leonie M. Kurzlechner, Tulsi Asokan, Andrew M. Breglio, M. Jay Campbell, Zebulon Z. Spector, Catherine W. Rehder, the Undiagnosed Diseases Network, Paul C. Tang, Cynthia A. James, Hugh Calkins, Vandana Shashi, and Andrew P. Landstrom.

More specifically for some of the data included in this dissertation, I would like to thank Zhu Zhang for performing the patch clamp experiments; Alexander Behura, Amy Berkman, Mary Moya-Mendez, and Angelina Sala for assisting with aspects of the calcium imaging and/or analysis; Qixin for the whole blood qPCR; Enya Dewars for technical assistance; Anna Ponck for the cyrosectioning and histological staining; Heidi Cope, Vandana Shashi, and the Undiagnosed Diseases network for the exome sequencing and genetic analysis of the *TAX1BP3* kindred; Gabrielle Monaco for the volcano plots; Leonie Kurzlechner for the iPSC validation IF images;

Tulsi Asokan for assistance with the isolated mouse ventricular myocyte IF; and Andrew Breglio for the mouse swimming study design.

I would also like to thank my committee members Marc Caron, Chris Nicchitta, Nenad Bursac, Howard Rockman, and Amy Bejsovec for their guidance and feedback. Special thanks to the Duke undergraduates Alexander Behura, Anna Ponek, and Angelina Sala for their support on this project. Thank you to all members of the Landstrom lab (past and present) for their friendship and assistance. Thank you to my mentor, Andrew Landstrom, for the mentorship, expertise, and encouragement throughout graduate school.

I would also like to express my immense gratitude to my family and friends for their constant support. Lastly (but most emphatically), I would like to thank my husband, Chris Kozlowski, for his unwavering encouragement.

1. Introduction

Arrhythmogenic cardiomyopathy (ACM), also known as arrhythmogenic right ventricular cardiomyopathy, is a primary disease of the heart muscle in which fibrofatty tissue replaces healthy myocardium and is associated with heart failure, life-threatening ventricular arrhythmias, and sudden cardiac death (Austin, Trembley et al. 2019). ACM has a frequency of 1:2,000 to 1:5,000 in the population and is one of the most common causes of sudden death in children and young adults, especially athletes (Corrado, Basso and Judge 2017, Krahn, Wilde et al. 2022). ACM is considered a genetic disease, and the mode of inheritance is typically autosomal dominant, although rare autosomal recessive forms can occur (McKoy, Protonotarios et al. 2000, Bennett, Haqqani et al. 2019). 80% of known ACM variants localize to genes that encode components of the cardiac desmosomes—macromolecular complexes of intercellular adhesion junctions between cardiac myocytes (Bennett, Haqqani et al. 2019, James, Jongbloed et al. 2021). While 60% of individuals with ACM host variants in known disease-associated genes, for the remaining 40% of patients, the cause is unknown (Ackerman, Priori et al. 2011). There are currently no treatments to reverse or halt disease progression. Although gene therapy is on the horizon for patients with pathogenic variants in desmosomal gene *PKP2* (Bradford, Zhang et al. 2023, van Opbergen, Narayanan et al. 2024), this treatment would not be applicable for the majority of ACM patients. Thus, there is a critical need for improved mechanistic understanding of ACM pathogenesis to facilitate the development of novel therapies.

ACM has four phases: 1) the concealed phase where there are no structural changes but sudden cardiac death is possible 2) the overt phase where arrhythmias and ventricular (typically of the right ventricle) structural changes may be seen with imaging 3) end-stage disease with ventricular dysfunction and 4) ventricular failure similar to dilated cardiomyopathy (Tadros, Miyake et al. 2023). Life-threatening arrhythmias are often the first presenting symptom in ACM

(Orgeron and Calkins 2016). A well-established mechanism of arrhythmogenesis is intracellular Ca^{2+} leak (Moccia, Lodola et al. 2019). Tight regulation of Ca^{2+} inside the cardiomyocyte is critical for the coordinated contraction of the cell. When the cardiomyocyte depolarizes, Ca^{2+} enters the cell through the L-type Ca^{2+} channel and binds to the ryanodine receptor (RyR2) on the sarcoplasmic reticulum (SR). RyR2 then opens, allowing the intracellular store of Ca^{2+} to be released and then bind to troponin C which causes contraction of the myofilaments. Aberrant Ca^{2+} can leak from RyR2 can lead to spontaneous depolarizations (delayed afterdepolarizations (DADS)) which, at the tissue level, can lead to triggered arrhythmias (Wehrens, Lehnart et al. 2003).

Here, we describe variants in *TAX1BP3*, a gene previously never associated with autosomal recessive ACM. Using patient-derived induced pluripotent stem cell-derived cardiomyocytes and a cardiac-specific *Tax1bp3* knockout mouse model, we find that loss of TAX1BP3 is associated with increased SR-mediated Ca^{2+} leak, delayed after depolarizations, and triggered arrhythmias. We demonstrate that increased TRPV4 activity is a major driver of this phenotype and show that pharmacologic blockade of TRPV4 rescues the Ca^{2+} leak that underlies arrhythmogenesis.

2. Materials and Methods

2.1 Clinical and human genetic methods

2.1.1 *Clinical evaluation*

Participants were diagnosed by their local providers with ACM based on the modified Task Force criteria (Marcus, McKenna et al. 2010). Specifically, pertinent demographics, personal and family history, and physical examination were performed by both board certified pediatric medical geneticists and pediatric cardiologists. Standard 12-lead ECG analysis, echocardiographic testing, and cardiac MRI (CMRI) were obtained. Initially, ACM gene-panel analysis included the following genes: *CTNNA3*, *DES*, *DSC2*, *DSG2*, *DSP*, *FLNC*, *JUP*, *LDB3*, *LMNA*, *PKP2*, *PLN*, *RYR2*, *SCN5A*, *TGFB3*, *TMEM43*, and *TTN*.

2.1.2 *Exome sequencing*

Exome sequencing (ES) was performed at the Undiagnosed Disease Network (UDN) sequencing core laboratory in the Baylor College of Medicine, with methods previously published (Yang, Muzny et al. 2013). The sibship was evaluated at the UDN at the Duke/Columbia site. For the younger affected brothers and both parents, the ES underwent a secondary analysis through a phenotype-agnostic research pipeline at the Duke/Columbia UDN clinical site, with methods described previously (Shashi, Schoch et al. 2019). To confirm the absence of the identified missense variant in ostensibly healthy individuals, the publicly-available Genome Aggregation Database (gnomAD) was used as a control cohort which is comprised of a total of 15,708 genomes and 125,748 exomes from 141,456 individuals (Lek, Karczewski et al. 2016). The variant was cross-referenced in ClinVar (National Center for Biotechnology Information) (Landrum, Lee et al. 2018). Sanger sequencing confirmation of the *TAX1BP3* locus was performed on all kindred. For this, genomic DNA was extracted according to the ReliaPrep™ Blood gDNA Miniprep System kit

(A5082, Promega). Primers are available on reasonable request. Polymerase chain reaction (PCR) was conducted using the 2.0X Taq Red Master Mix kit (42-138, Genesee) and the subsequent product was sequenced using direct Sanger sequencing with BigDye Terminator v1.1 (43-374-50, Applied Biosystems) according to the manufacturer's protocol and electrophoresed on an 3730xl DNA Analyzer (3730XL, Applied Biosystems).

2.1.3 *Chromosomal microarray analysis*

Chromosomal microarray analysis (CMA) was performed using the Affymetrix Cytoscan HD array (901835) at the clinical cytogenetics laboratory at Duke University. This array includes about 2.7 million genetic markers incorporating 743,304 single nucleotide polymorphism probes as well as 1,953,246 non-polymorphic copy number variation (CNV) probes with a median spacing of 0.88 kb. Genomic linear positions are given relative to NCBI build 37 (hg19).

2.1.4 *Sequence homology and domain mapping*

TAX1BP3 consensus sequence (NP_055419.1) was obtained from the Ensembl browser (Cunningham, Achuthan et al. 2018). Primary sequence conservation among 194 independent *TAX1BP3* orthologues was compared to determine degree of conservation across species using the National Center for Biotechnology Information (NCBI). Percent identity was calculated as the proportion of species with predicted *TAX1BP3* orthologues containing an identical amino acid at a given position relative to human.

2.1.5 *RT-qPCR*

Whole blood was collected via peripheral phlebotomy into Paxgene Blood RNA tubes (762165, BD Biosciences). Total RNA was extracted using Quick-RNA™ Whole Blood (R1201,

Zymo Research). The concentrations of RNA were measured using Nanodrop One (ND-ONE-W, Thermo Fisher Scientific). cDNA was synthesized by iScript Reverse Transcription Supermix for RT-qPCR (1708841, Bio-Rad Laboratories). Quantitative real-time polymerase chain reaction (qRT-PCR) was performed on a 7300 Real Time PCR system (Applied Biosystems) using the SYBR™ Green PCR Master Mix (4309155, Invitrogen) according to the manufacturer's protocol. Relative quantification was normalized against *RPL32*. At least three independent experimental replicates were performed, each with at least three internal technical replicates.

2.1.6 *In silico* variant pathogenicity modeling

In silico variant pathogenicity prediction was performed using PolyPhen-2 (Adzhubei, Schmidt et al. 2010), SIFT (Vaser, Adusumalli et al. 2016), PANTHER (Tang and Thomas 2016), Provean (Choi 2012), and MUpro (Cheng, Randall and Baldi 2006), and Revel (Ioannidis, Rothstein et al. 2016) prediction tools.

2.2 Induced pluripotent stem cell methods

2.2.1 *Peripheral blood mononuclear cell proliferation*

Peripheral blood samples were diluted in an equal volume of 1X Phosphate buffered saline (PBS) with 2% FBS and added to SepMate tubes (85450, Stemcell Technologies) loaded with Lymphoprep (07851, Stemcell Technologies). Following manufacturer's protocol, isolated peripheral blood mononuclear cells (PBMCs) were cultured in Erythroid Expansion Media: Stemspan SFEM II (09655, Stemcell Technologies) with Erythroid Expansion Supplement (02692, Stemcell Technologies) and 100µg/ml Primocin (ant-pm-1, InvivoGen). The PBMCs were grown

for 24 hours before being re-plated, the media was changed every 2 days, and cells were cultured for a total of 6 days before being cryopreserved.

2.2.2 Generation of iPSCs

Human induced pluripotent stem cells (iPSCs) were generated from the expanded PBMC lines through the Human Stem Cell Core at Baylor College of Medicine. To initiate reprogramming, approximately 1×10^5 erythroid progenitors were spininfected at $1,040 \times g$ for 90 minutes with non-integrating Sendai viruses expressing OCT4, SOX2, KLF4, and C-MYC by CytoTune-iPS 2.0 (A16517, Invitrogen). Clonal human iPSC colonies were derived under feeder-free conditions using hESC-qualified Matrigel (354230, Corning) and ReproTeSR medium (05926, Stemcell Technologies). Individual colonies were manually picked and expanded in TeSR-E8 medium (05990, Stemcell Technologies) (Chen, Gulbranson et al. 2011). Lines of iPSCs were validated by colony morphology, g-banding karyotyping (Baylor Medical Genetics Lab) to confirm normal diploid chromosomes and were tested for mycoplasma. Two clones of iPSCs for each donor were used for downstream experiments to control for interline variability.

2.2.3 iPSC culture and differentiation of cardiomyocytes

iPSCs were plated in mTeSR media (85857, StemCell Technologies) with 10% CloneR (StemCell Technologies) on a 2% Matrigel-coated (354230, Corning) 6 well plate (353036, Corning). After 24 hours, mTeSR without CloneR was used and changed daily. Cells were passaged by release from the Matrigel coating with ReLeSR (05873, StemCell Technologies). iPSCs were seeded to Matrigel-coated wells. iPSCs were differentiated into iPSC-CMs utilizing a method adapted from Burridge et al, 2014 (Burridge, Matsa et al. 2014). Day 0 of differentiation began when iPSCs were 80-90% confluent with the addition of 60ng/ μ l Activin A (78001.1,

StemCell Technologies), 12uM CHIR 99021 (13122, Cayman Chemical), 50ug/ml Ascorbic Acid (Tocris Bioscience, Bristol, UK) in RPMI 1640 with 2% B27 without insulin (A1895602, Life Technologies) (RPMI/B27-). On day 1 and day 2, the cells were given RPMI/B27- with 5µM IWR1 (StemCell Technologies) and 50µg/ml Ascorbic Acid. On day 4, the media was changed to RPMI/B27- with 5µM IWR1. From day 6 onwards the cells are given RPMI 1640 (11875199, Thermofisher Scientific) with 2% B27 with insulin (17504044, Life Technologies) every other day and observed for beating. iPSC-CMs were used for downstream experiments after day 30 of differentiation.

2.2.4 Fat accumulation in iPSC-CMs

To drive fatty acid oxidation from glycolysis, we supplemented insulin, dexamethasone, and 3-isobutyl-1-methylxanthine (IBMX, 3F media) to iPSC-CMs (Kim, Wong et al. 2013). This media was applied when the iPSC-CMs were day 30 of differentiation and treated for 30 days every other day. To visualize fat accumulation, the iPSC-CMs were stained with Nile Red and co-stained with TNNT2. Cells were imaged using a Zeiss LSM 510 confocal microscope: 4.5mm x 4.5mm areas were imaged by taking a 5 x 5 tile scan at 10X magnification.

2.2.5 Western blot

iPSC-CMs were lysed with RIPA buffer and 60µg of lysate loaded onto a polyacrylamide gel and run for 35min at 200V at 4C. Proteins were transferred to a polyvinylidene fluoride (PVDF) membrane using the Trans-Blot Turbo System (1704150, BioRad). The membrane was blocked for 1 hour at room temperature with 5% milk. The membrane was blotted overnight at 4C with the appropriate primary antibodies: rabbit anti-TAX1BP3 (1:1000, 11692-1-AP, Proteintech), mouse anti-SERCA2 (1:500, sc-376235, Santa Cruz Biotechnology), mouse anti-NCX (1:1000, MA3-926,

ThermoFisher Scientific), mouse anti-phospholamban (1:1000, MA3-922, ThermoFisher Scientific), rabbit anti-phospho-phospholamban ser16 (1:1000, 07-052, Sigma Aldrich). The membrane was blotted with goat anti-mouse and anti-rabbit HRP secondaries (1:2000) for 1 hour at room temperature. Clarity Western ECL substrate was added before imaging (32106, ThermoFisher Scientific). The membranes were then reblotted with mouse anti-GAPDH (1:2000, AKR-001, Cell Biolabs)

2.2.5 Immunofluorescence (IF)

To fix the iPSC-CMs, 4% paraformaldehyde (PFA) was applied for 15 minutes. 0.5% Triton X-100 (v/v, in PBS) was added for 15 minutes to the slide for permeabilization. A blocking solution of 3% (w/v) bovine serum albumin in PBS was added for 30 minutes. The primary antibody solution of 1:300 mouse anti-TNNT2 (TNNT2, ab209813, Abcam), 1:1000 anti-Nanog (sc-374001, Santa Cruz Biotechnology), or 1:1000 anti-Oct3/4 (sc-5279, Santa Cruz Biotechnology) into 1% BSA in PBS and incubated at 4°C overnight. The secondary antibody solution of Alexa Fluor 488-conjugated AffiniPure donkey anti-mouse IgG (715-545-150, Jackson Immunoresearch) was diluted 1:1000 in PBS and incubated with the cells at room temperature for an hour. Nile Red Stain (ab228553, Abcam) was also added 1:4 to the entire secondary solution if required. The cells were covered in VECTASHIELD Vibrance Antifade Mounting Medium with DAPI (H-1700-10, Vector Laboratories) and stored at 4°C. For Nile Red image analysis, 5x5 10x tilescans with z-stacks to include all cells were obtained per dish. Fluorescence of TNNT2 signal (green) and Nile Red (red) was thresholded and quantified using FIJI, and the percentage of Nile Red was normalized to the percentage of TNNT2 to account for variability in cell number.

For Trpv4 and RyR2 IF, isolated ventricular myocytes were plated onto 200µg/ml laminin coated coverslips for one hour before the same fixation and staining as described above. Rabbit

anti-Trpv4 (ACC-034, Alomone Labs) was used at 1:500 and mouse-anti Ryr2 (CBL173, EMD Millipore) was used at 1:400. 1:10000 Hoechst 33258 (Thermofisher Scientific, H21491) was incubated for 5 minutes prior to mounting with Permount Mounting Medium (Thermofisher Scientific, SP15100). Z-stacks were obtained of the entire cell at 63X with a Zeiss Laser Scanning Confocal 510 Meta Microscope (Carl Zeiss AG).

2.2.6 Lentiviral overexpression of TAX1BP3

Plasmids were cloned and packaged into lentiviruses by Vectorbuilder. 1) TAX1BP3: pLV[Exp]-EF1A>hTAX1BP3[NM_014604.4]/T2A/mCherry (Vector ID: VB240130-1297nsb) 2) TAX1BP3-M78T: pLV[Exp]-EF1A>hTAX1BP3[NM_014604.4]*/T2A/mCherry (Vector ID: VB240129-1391zaq) 3) Control (mCherry alone): pLV[Exp]-EF1A>mCherry (Vector ID: VB900088-2479xcj).

iPSC-CMs were transduced by each respective lentivirus with an MOI of 5 and 2.5 $\mu\text{g/ml}$ Polybrene (Vectorbuilder). Media was replaced after 24 hours. Cells were observed for mCherry fluorescence and used for downstream experiments 4-8 days following transduction. For calcium imaging, only cells that had red fluorescence were selected for line scans.

2.2.7 Patch clamp

Whole cell voltage-clamp experiments were performed to record membrane current using a MultiClamp-700A amplifier with Digidata 1322A interface and Clampex software (Axon Instruments) as described previously (Zhang, Huang et al. 2017). The cover-glass with iPSC-CM cells was continuously perfused (at 2ml/min, room temperature) with external solution containing (in mM): 150 NaCl, 6 CsCl, 5 CaCl₂, 1 MgCl₂, 10 HEPES, 10 glucose, (pH 7.4 with NaOH). The patch pipettes had a resistance of 3~6 M Ω when filled with pipette solution contained (in mM) 100

Cs-aspartate, 20 CsCl, 1 MgCl₂, 4 Na₂-ATP, 10 HEPES, 10 EGTA, and 0.08 CaCl₂ (pH 7.2 with CsOH). To block LTCC, Nifedipine (10 μ M) was added in external solution. Cells were held at a potential of 0 mV, and ramps from +100 mV to -100 mV with a duration of 400 ms were applied at a frequency of 0.1 Hz. Data were acquired at sample rate of 10 kHz (filtered at 1 kHz). After stabilization, a TRPV4 specific agonist GSK 1016790A (1 μ M, Sigma-Aldrich) was used to stimulate TRPV4 current (I_{TRPV4}). Membrane currents were normalized by cell membrane capacitance(pA/pF) and leak subtracted. The differences (at +/- 80mV) before and after GSK 1016790A administration were compared in WT and mutant iPSC-CM cells (Liao, Wu et al. 2020). Action potentials were recorded in TAX1BP3^{WT/WT} and TAX1BP3^{M78T/del} iPSC-CMs. Patch-clamp experiments were performed in whole cell current-clamp mode using a MultiClamp-700A amplifier with Digidata 1322A interface and Clampex software (Axon Instruments). Cells on cover-glass were continuously perfused (at 2ml/min) with Tyrode's solution containing (in mM): 140 NaCl, 5.4 KCl, 2 CaCl₂, 1 MgCl₂, 10 HEPES, 10 glucose, pH 7.4.). The patch pipettes had a resistance of 6~10 M Ω when filled with pipette solution contained (in mM) 130 K-aspartate, 6 NaCl, 3 Mg-ATP, 0.4GTP,10 HEPES, 5 EGTA, and pH 7.2 (with KOH). Experiments were performed at 35.0 +/- 0.5 C°. Data were acquired at sample rate of 10 kHz (filtered at 1 kHz) and analyzed with pCLAMP 10 software (Axon Instruments).

2.2.8 RNA-sequencing

Bulk RNA-sequencing was conducted on RNA from iPSC-CMs which included 3 iPSC experimental replicates (three different passages) per clone for each of the 2 clones per line. RNA was extracted using Direct-Zol RNA Purification Kit (R2052, Zymo Research). The Sequencing and Genomics Technologies Core Facility at Duke University performed RNA-sequencing. mRNA was enriched from total RNA and reversed transcribed into cDNA to build sequencing libraries

using the Kapa mRNA HyperPrep Kit from Roche (Code: KK8581). Libraries were pooled to equimolar concentration and sequenced on the NovaSeq 6000 S1 flow cell to produce 50 bp paired-end reads.

RNA-seq data was processed using the fastp toolkit (Chen, Zhou et al. 2018) to trim low-quality bases and sequencing adapters from the 3' end of reads, then mapped to GRCh38 (downloaded from Ensembl, version 106) (Kersey, Staines et al. 2012) using the STAR RNA-seq alignment tool (Dobin, Davis et al. 2013), and reads aligning to a single genomic location were summarized across genes. For genes having an overlap of at least 10 reads, gene counts were normalized and differential expression was carried out using the DESeq2 (Love, Huber and Anders 2014) Bioconductor (Huber, Carey et al. 2015) package implemented for the R programming environment. Consistent with the recommendation of the DESeq authors, independent filtering (Ignatiadis, Klaus et al. 2016) was utilized prior to calculating adjusted p-values (Benjamini and Hochberg 1995) and moderated log₂ fold-changes were derived using the ashR package (Stephens 2016).

2.3 Tax1bp3 knockout mouse methods

2.3.1 Generation of Tax1bp3 knockout mouse

Mice with the *Tm1c* allele with loxP sites flanking *Tax1bp3* exons 2-4 were obtained by the European Mouse Mutant Archive (EMMA). These mice were crossed with alpha-MHC-MerCreMer mice to create an inducible, cardiac-specific *Tax1bp3* knockout line. Pups injected with 100µl of 10mg/ml tamoxifen (T5648, Sigma-Aldrich) at 1.5 months once a day for 3 days for induction of Cre. Experiments were conducted when mice were 5.5-6 months of age.

2.3.2 Mouse experimental design

Mice were kept in standard house conditions with standard light cycles with standard *ad lib* food and water. All mice were treated in accordance with the Duke University School of Medicine Institutional Animal Care and Use Committees and reflected proposed guidelines for rigor and reproducibility in preclinical animal studies (Ginsburg, Shah and McCarthy 2007, Bolli 2017). Exclusion criteria were 1) non-experimental mice used for mating and 2) mice that were homozygous for Cre or WT for Cre for both alleles. All experimental protocols were prospectively written. All studies were conducted blinded to mouse genotype unless otherwise noted. No randomization was performed. Littermate *Tax1bp3^{+/+}* mice that were heterozygous for MCM allele and treated with tamoxifen were used for controls for all experiments. Both males and females were utilized in equal proportions. Unless otherwise noted, for all studies, mice were anesthetized in an induction chamber with 2% isoflurane mixed with 1 L/min 100% O₂ for 10-15 minutes until the withdrawal reflex was absent (R583S Vaporizer, RWD Life Science, San Diego, CA).

2.3.3 *Ventricular myocyte isolation*

Langendorff perfusion protocol was adapted from O'Connell et al (O'Connell, Rodrigo and Simpson 2007). Briefly, mouse hearts were rapidly excised and aorta cannulated and perfused with Tyrode solution (130 mM NaCl, 5.4 mM KCl, 2 mM NaHCO₃, 1.2 mM MgSO₄, 10 mM HEPES, and 15 mM Glucose, pH 7.35) for 5 minutes before being transferred to a Langendorff apparatus for perfusion with 2.4mg/ml Collagenase II in Tyrode for 7-10 minutes. The heart was then removed and placed in stopping buffer (10% FBS in Tyrode), pulled apart, and manually triturated. Large debris was separated and the single cell suspension supernatant was then used for either Ca²⁺ imaging or immunofluorescence experiments.

2.3.4 Immunofluorescence

Isolated ventricular myocytes were plated onto 200 μ g/ml laminin coated coverslips for one hour before fixing in 4% paraformaldehyde (PFA) was applied for 10 minutes. 0.5% Triton X-100 (v/v, in PBS) was added for 10 minutes to the slide for permeabilization. A blocking solution of 3% (w/v) bovine serum albumin in PBS was added for 30 minutes. Rabbit anti-TRPV4 (ACC-034, Alomone Labs) was used at 1:500 and mouse-anti RyR2 (CBL173, EMD Millipore) was used at 1:400 and incubated overnight at 4 degrees Celsius. Secondaries were used at 1:1000 and incubated for 1 hour at room temperature (Alexa Fluor 594-AffiniPure Goat Anti-Rabbit IgG and Alexa Fluor 488-AffiniPure Goat Anti-mouse IgG, Jackson ImmunoResearch, 111-585-003 and 715-545-150). 1:10000 Hoechst 33258 (Thermofisher Scientific, H21491) was incubated for 5 minutes prior to mounting with Permount Mounting Medium (Thermofisher Scientific, SP15100). Z-stacks were obtained of the entire cell at 63X with a Zeiss Laser Scanning Confocal 510 Meta Microscope (Carl Zeiss AG).

2.3.5 Echocardiography

Conscious mice were briefly restrained by hand or placed on chamber to remove chest and abdominal hair by either a clipper or depilatory cream and perform echocardiographic imaging. Ultrasonic gel and/or 70% ETOH was applied on the imaging surface to enhance image quality. Two-dimensional (2D) guided B-mode and M-mode echocardiography was performed using an echocardiograph machine (Vevo 2100 High Resolution Imaging System, VisualSonics, Toronto, ON, Canada). All imaging and subsequent echo-based measurements were conducted blinded to genotype.

2.3.6 *Histology*

Rapidly excised mouse hearts were perfused with 5 mL of cold 1X PBS followed by 5 mL 4% PFA (158127, Sigma-Aldrich) until the heart stiffens. Hearts were then put in 4% PFA, incubated at 4°C overnight, washed 2X in cold PBS, and covered in 100 mM glycine (VWR) in 1 mM EDTA (T9650, Sigma-Aldrich). Following incubation at 4 °C, the heart was washed in ice cold PBS then submerged in 30% sucrose (MP Biomedicals) in PBS and incubated at 4°C until tissue sank. Hearts were placed in casts (Polysciences, Warrington, PA), filled with O.C.T. solution (4583, Sakura Finetek) for embedding and put on the dry ice until covered and frozen. 10 µm frozen sections were prepared on a Leica microtome (Leica Biosystems, Nussloch, DE). To determine the morphology of the heart, the hematoxylin and eosin staining was performed on sections following the manufacturer's protocol (ab24880, Abcam). To determine the collagenous connective tissue fibers of the heart, the Masson's Trichrome staining was performed on sections following the manufacturer's protocol (ab1500686, Abcam). For visualizing fat accumulation, Oil Red-O was performed on sections following the manufacturer's protocol (ab150678, Abcam). Image acquisition was performed on a Zeiss Axio Imager Z2 Upright Microscope (Carl Zeiss, Oslo, NO) and analyzed ZEN 2 pro software (Carl Zeiss, Oslo, NO).

2.3.7 *Mouse intracardiac electrophysiology*

Mice were anesthetized using a volatile anesthetic system with induction chamber (R5835, RWD Life Science, Dover, Delaware) with 2% isoflurane mixed with 2L/min 100% O₂. Subdermal leads were placed for surface electrocardiographic (ECG) analysis which includes two total leads: I and II. Baseline ECGs were recorded at 1000 samples/second and measured when mice reached internal temperature of 37 degrees Celsius. Jugular venous cutdown was performed using a dissection microscope (A60, Leica, Buffalo Grove, Illinois) and an 8-lead 1.1F, 8E, 1.0mm

octapolar catheter electrophysiology catheter (iWire-BIO8, ADInstruments, Colorado Springs, Colorado) was placed in the internal jugular vein and positioned in the right ventricle and right atrium (Au - Li and Au - Wehrens 2010). ECG parameters, including RR, PR, QRS, QT, and corrected QT (Bazett's QT correction) were measured as well as sinus node recovery time (SNRT) and AV node effective refractory period (AVERP) obtained. Electrical pacing was performed utilizing customized electrical stimulator to elicit ectopy and arrhythmia generation with progressive electrical challenge (Clasen, Eickholt et al. 2018). Specifically, for atrial pacing, 200-pulse pacing episodes with pacing interval stepping from 55ms to 15ms with 2ms decrement were applied with a 10-15 sec inter-episode break; for ventricular pacing, 30-pulse pacing episodes with pacing interval of 75ms were applied followed by 10 pulses with pacing interval stepping from 55ms to 15ms with 2ms decrement with a 10-15 sec inter-episode break. Induction of atrial and ventricular arrhythmias was tested using this electrical stimulation. Rhythm detection was captured by an iWorx-RA-834 Eight Channel 16bit Data Acquisition System (iWorx, Dover New Hampshire, United States). Data was viewed using a custom-built ECG Analysis Module software program for LabScribe v4. Adrenergic stimulation and ryanodine receptor sensitization was achieved with 200 μ g/g caffeine and 1 μ g/g isoproterenol IP and repeat ECG measurements made after two minutes. Atrial and ventricular pacing were then repeated. Sustained VT was defined as greater than 10. All studies were performed blinded to genotype.

2.3.8 *Mouse swimming*

Two independent mouse swimming experiments were performed. For each experiment, mice were placed at the same time in a large water bath kept between 35 and 37 degrees Celsius at a water depth that prevented them from being able to touch the bottom (approximately 6cm). The mice were continuously monitored for signs of struggle and were removed from swimming early

if they were unable to keep themselves above the water. Specifically, mice were removed if their head submerged under the water for longer than two seconds or submerged more than twice within a 10 second period. After removal, the mice were dried off and recovered in a cage on a heating pad before being returned to their cages.

2.4 Ca²⁺ imaging and analysis

To conduct live cell Ca²⁺ imaging, iPSC-CMs were washed once with 1X Ca²⁺-free Tyrode solution and then were stained with 10 μ M CAL-520 (ab171868, Abcam) for 1 hour. iPSC-CMs were then incubated with a 1:1 solution of RPMI/B27+ and 1X Tyrode with 1.8mM CaCl₂ for 30 minutes prior to imaging. Line scans of iPSC-CMs were acquired on a Zeiss Laser Scanning Confocal 510 Meta Microscope (Carl Zeiss AG) at 0.1 μ m per pixel. iPSC-CMs were paced at 0.5Hz with an IonOptix MyoPacer field stimulator (IonOptix) for ten seconds. Fiji ImageJ v.1.53c (National Institutes of Health) was used to analyze Ca²⁺ transients. Fiji was used in conjunction with the 2007 SparkMaster plug-in to quantify sparks (Picht, Zima et al. 2007). SparkMaster calculated and displayed a set threshold for quantifying sparks and their features at 3.8 times the standard deviation of surroundings. Features include spark duration, width, time to peak, amplitude and tau. Regions of interest were generated 0.22 seconds from the last paced beat. The average amplitude, width, and duration at half the maximum of all the sparks for a cell were multiplied with the spark frequency to generate a total leak value per cell. For the calcium TRPV4 inhibition experiments, DMSO or 1 μ M HC-067047 (4100, Tocris) was added in 1:1 solution of RPMI/B27+ and 1X Tyrode with 1.8mM CaCl₂. For caffeine analysis, cells were imaged with a Zeiss spinning disk Axio Observer.Z1 at 215ms intervals at 40X. 10mM caffeine was added to the iPSC-CMs after a 10 second pause following 10 seconds of 1Hz pacing. For Fura-2 imaging, iPSC-CMs were loaded with 10 μ M Fura-2;AM (AS-84017, Anaspec) in calcium-free 1X Tyrode containing 0.1%

Pluronic F-127 (P2443, Sigma-Aldrich) for 30 minutes and then incubated in 1:1 solution of RPMI/B27+ and 1X Tyrode with 1.8mM CaCl₂ for 30 minutes prior to imaging. Experiments were performed at room temperature. Cells were imaged with a Nikon TE2000-E with 340/380 dual excitation filter. The iPSC-CMs were paced for ten seconds at 0.5Hz first before data collection. The MetaFluor software (Molecular Devices) was used to generate 340/380 ratios. NCX activity was calculated as $1/\tau_{\text{caffeine}}$ and SERCA2A activity was calculated as $1/\tau_{\text{transient}} - 1/\tau_{\text{caffeine}}$ (Voigt, Heijman et al. 2014, Alsina, Hulsurkar et al. 2019).

2.5 Statistical analysis

To determine statistical significance among groups, a paired Student's t-test was performed for data with a normal distribution with two groups, and a one-way ANOVA with multiple comparisons was used for 3 groups. Normal distribution was tested with Shapiro-Wilk test. For non-parametric data, a Mann-Whitney test was used when comparing two groups and a Kruskal-Wallis test with Dunn post hoc tests were used when comparing 3 groups. Chi squared tests (or Fisher's exact tests where appropriate) were used for categorical data. For nested data, we performed the hierarchical analysis described in Sikkel et al. 2017 using the R code provided using R studio (Sikkel, Francis et al. 2017). With non-parametric data, the data was first Log10-transformed before running the R code. Data are presented as the mean \pm SEM. P<0.05 were considered statistically significant.

3. TAX1BP3 is associated with autosomal recessive pediatric-onset ACM

3.1 Clinical evaluation

To identify the cause of genetically elusive ACM in kindred presenting with pediatric ACM, the family was enrolled and clinically evaluated. The kindred pedigree and selected cardiac MRI (CMRI) images and the kindred pedigree are shown in **Figures 1 and 2**. The proband was a male (II.1) with no significant past medical history who died suddenly at 17 years of age while playing baseball. Autopsy revealed significant right ventricular dilation, multiple foci of myocardial fibrosis, and diffuse interstitial fibrosis with some asymmetric hypertrophy of the lateral left ventricular wall. The cause of death was declared as arrhythmia secondary to ACM. Based on the autopsy findings, additional family members including three siblings (ages 10-16 years at that time) were subsequently evaluated, with normal echocardiograms. Four years later, at age 14, the proband's youngest brother (II.4) presented after vigorous exercise with monomorphic ventricular tachycardia with left bundle branch block and an inferior axis. CMRI demonstrated a mildly dilated right ventricle (RV) with severe dysfunction (right ventricular ejection fraction 30%) and akinetic/dyskinetic segments, as well as fatty infiltration in the right ventricular myocardium. These findings were consistent with a diagnosis of ACM and an implantable cardioverter defibrillator (ICD) was placed. The older surviving brother (II.2), then age 19, demonstrated mild right ventricular dilation with reduced right ventricular ejection fraction of 40%, and dyskinetic areas and hyperenhancement of the right ventricular aspect of the inferior ventricular septum by delayed enhancement imaging via CMRI. A 24-hour Holter monitor demonstrated approximately 1500 premature ventricular complexes with left bundle branch block morphology and superior axis in 24 hours. Both surviving brothers had similar patterns of scarring/fat of the RV (II.2: 68.75% and II.4: 75%) and both had approximately 1% in the LV. This remodeling did not impact systolic function,

and both had normal RV and LV ejection fractions. Despite similar fibrosis patterns and amount of remodeling, II.4 demonstrated a higher arrhythmia burden than II.2. Additional CMRI images and diagnostic electrocardiograms (ECGs) are included in **Figures 3, 4, and 5**. The proband's sister (II.3) and biological parents (I.1 and I.2) were found to have no evidence of ACM after extensive testing including CMRI, ECG, and Holter monitoring.

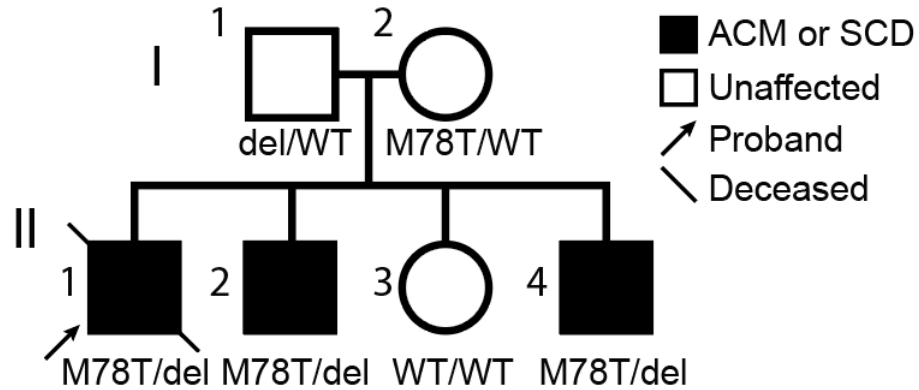


Figure 1: Pedigree of *TAX1BP3*-M78T/del kindred with arrhythmogenic cardiomyopathy

Pedigree of *TAX1BP3* variants co-segregating in kindred with ACM. Subjects are labeled by position on phylogenetic tree. Roman numerals indicate generation and numbers label kindred member. Black fill = sudden cardiac death (SCD) or diagnosis of ACM. Slash = deceased.

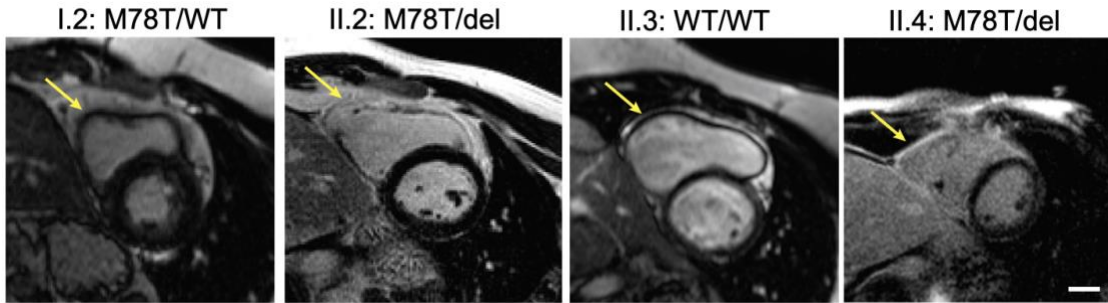


Figure 2: Clinical evaluation by cardiac MRI

Delayed enhancement cardiac magnetic resonance images (CMRI) of healthy mother (I.2, p.M78T/WT) and sister (II.3, WT/WT) demonstrating healthy myocardium (black signal) of the right ventricle (RV) free wall and youngest brother (II.2, p.M78T/del) and oldest brother (II.4, p.M78T/del) with fibrofatty hyperenhancement (bright signal) of the RV free wall. Yellow arrows show location RV free wall. Scale bar = 2cm.

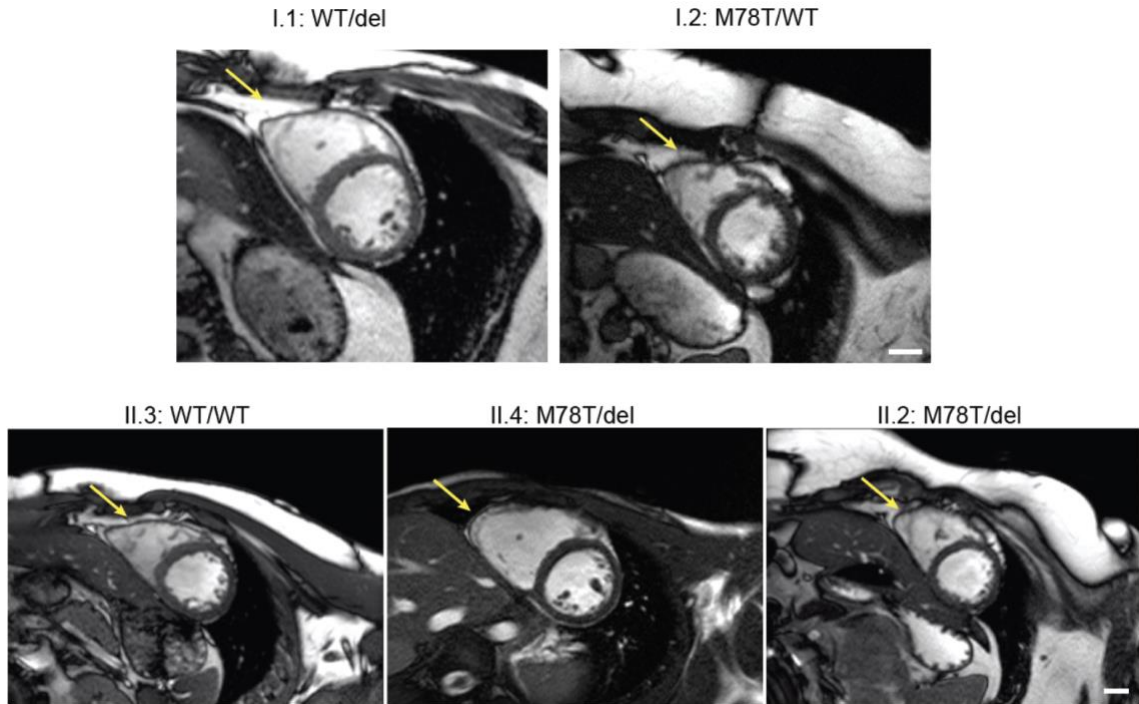


Figure 3: Additional Cardiac MRI imaging

CMRIs from the healthy father (I.1, del/WT) and mother (I.2, p.M78T/WT) and three surviving children: healthy sister (II.3, WT/WT), youngest brother (II.4, p.M78T/del) indicating a mildly dilated right ventricle, and oldest brother (II.2, p.M78T/del) showing mild right ventricular dilation and dyskinetic areas. RV free wall location indicated by yellow arrows. Scale bars = 2cm.

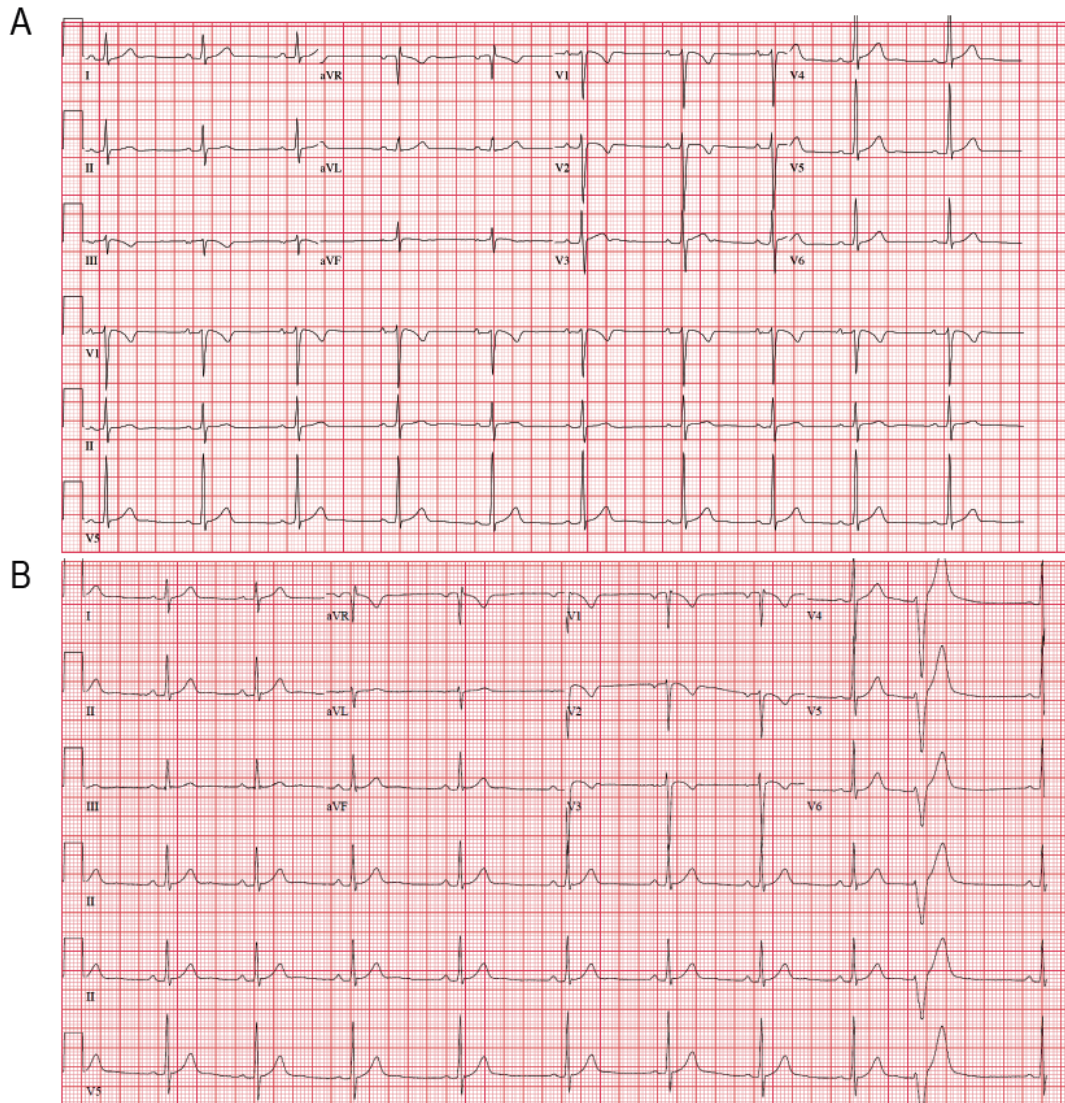


Figure 4: ECG Evaluation

A) Representative 12-lead ECG from individual II.4 showing normal sinus rhythm with T wave inversions in septal leads (V1 and V2) B) 12-lead ECG from individual II.2 showing normal sinus rhythm with premature ventricular contractions (PVCs).

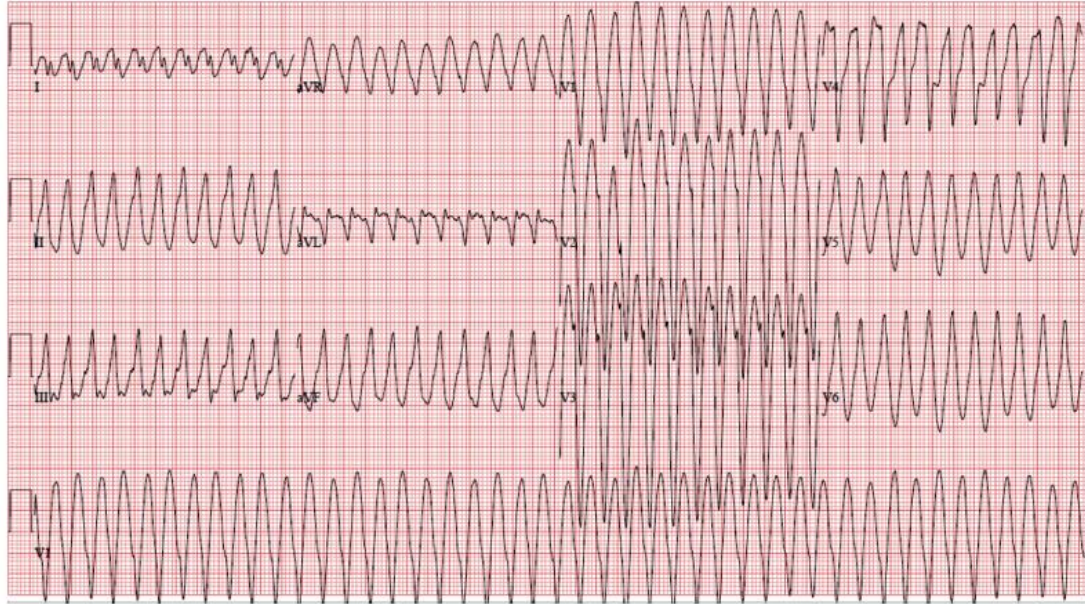


Figure 5: ECG from individual II.4 with ventricular tachycardia
 12-lead ECG from individual II.4 showing wide complex tachycardia consistent with ventricular tachycardia.

3.2 Genetic evaluation

All immediate family members underwent genetic testing, and a next generation sequencing panel for variants in 13 known ACM-associated genes did not identify a diagnostic genetic variant (Musunuru, Hershberger et al. 2020, Landstrom, Kim et al. 2021). The two surviving brothers were subsequently evaluated through the Undiagnosed Diseases Network (UDN). Exome sequencing (ES) through the UDN identified a paternally inherited deletion of approximately 238 kb encompassing the entire *TAX1BP3* (MIM# 616484) gene locus and a maternally inherited hemizygous missense variant in *TAX1BP3* (NM_014604.4:c.233T>C, p.M78T) in both brothers (II.2 and II.4) (**Figure 6 A-C**). The 17p13.2 deletion was confirmed by chromosomal microarray analysis (CMA) and reported as 242 kb (chr17:3,392,348-3,634,096, **Figure 7**). In addition to the 242 kb deletion, the youngest brother (II.4) was found to have two additional deletions on CMA: a 592 kb deletion of unknown significance at 3p26.3 (chr3:858,547-

1,450,741) and a likely pathogenic deletion at 14q23.3 (chr14:67,198,080-67,285-061), which could be related to his non-cardiac findings. Due to the previous report of *TAX1BP3* biallelic variants in a sibling pair with dilated cardiomyopathy and septo-optic dysplasia (Reinstein, Orvin et al. 2015), ophthalmologic exams were obtained in both affected brothers and were normal. Neuropsychological evaluations confirmed ADHD in both brothers (II.2 and II.4) and cognitive functioning below age-based expectations for the youngest brother (II.4). The youngest brother also has had diabetes mellitus type I since the first decade of life.

The deceased proband (II.1) was confirmed to have both the 242 kb deletion and the p.M78T missense variant through chromosomal microarray analysis (CMA) and Sanger sequencing on blood that had been stored by the state laboratory following the autopsy. The unaffected sister (II.3) was found to not have either of the two variants. Therefore, the two *TAX1BP3* variants co-segregated with disease in an autosomal recessive manner. Clinical and genetic findings are summarized in **Table 1**.

The p.M78T missense variant was confirmed by Sanger sequencing (**Figure 8A**). We next performed RT-qPCR on whole blood from each family member for *TAX1BP3* (**Figure 8B**). The unaffected parents with the deletion and p.M78T demonstrated a ~50% and ~75% reduction in *TAX1BP3* expression. *TAX1BP3* mRNA expression was reduced by about 90% in affected individuals (p.M78T/del).

TAX1BP3 is ubiquitously expressed, including in cardiac myocytes (v.19.3.proteinatlas.org) (Uhlén, Fagerberg et al. 2015). It is a small protein of 124 amino acids (13.74 kDa) and consists of a single PDZ domain (Cui, Hayashi et al. 2007). These domains are common protein interaction sites, and *TAX1BP3* has been shown to physically interact with other proteins such as β -catenin and rhotekin (Reynaud, Fabre and Jalinot 2000, Kanamori, Sandy et al. 2003, Lee and Zheng 2010). The p.M78T variant localizes within this PDZ domain in an area with

high sequencing conservation across species (86.7%), and a GERP++RS score of 5.31 (**Figure 6C**) (Cooper, Stone et al. 2005). *TAX1BP3* is a tolerant gene with an RVIS score of 45 and pLI of 0.005. The p.M78T variant was not identified in ~13,000 internal controls, gnomAD, or ClinVar databases (Landrum, Lee et al. 2018, Karczewski, Francioli et al. 2020). *In silico* modeling also suggests that the p.M78T variant would be deleterious to protein function (**Table 2**). Taken together, these results suggest that biallelic variants in *TAX1BP3* are associated with autosomal recessive ACM.

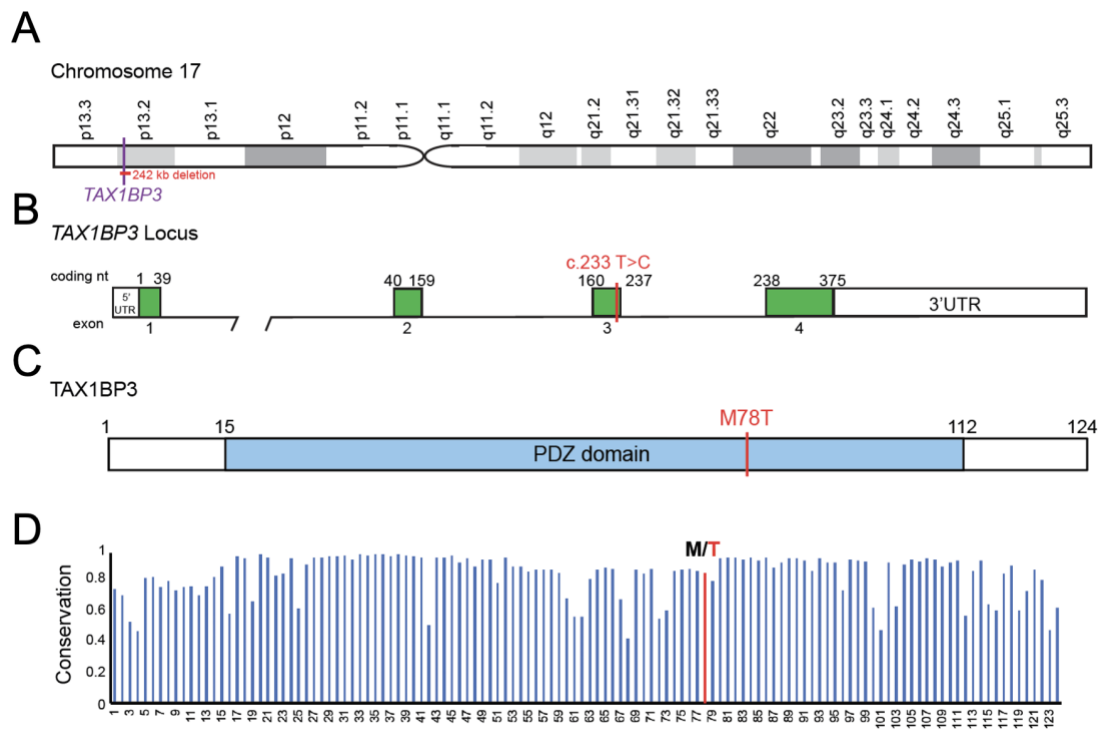


Figure 6: TAX1BP3 variant locations

A) Genomic location of the *TAX1BP3* locus on chromosome 17 in purple, with location of deletion in red. B) *TAX1BP3* locus with location of variant on exon 3. C) Linear topology of *TAX1BP3* with PDZ domain and p.M78T variant location noted. D) Amino acid conservation analysis demonstrating the percent conservation across 195 species at each *TAX1BP3* position relative to the human sequence. Conservation analysis performed by Qixin Yang.

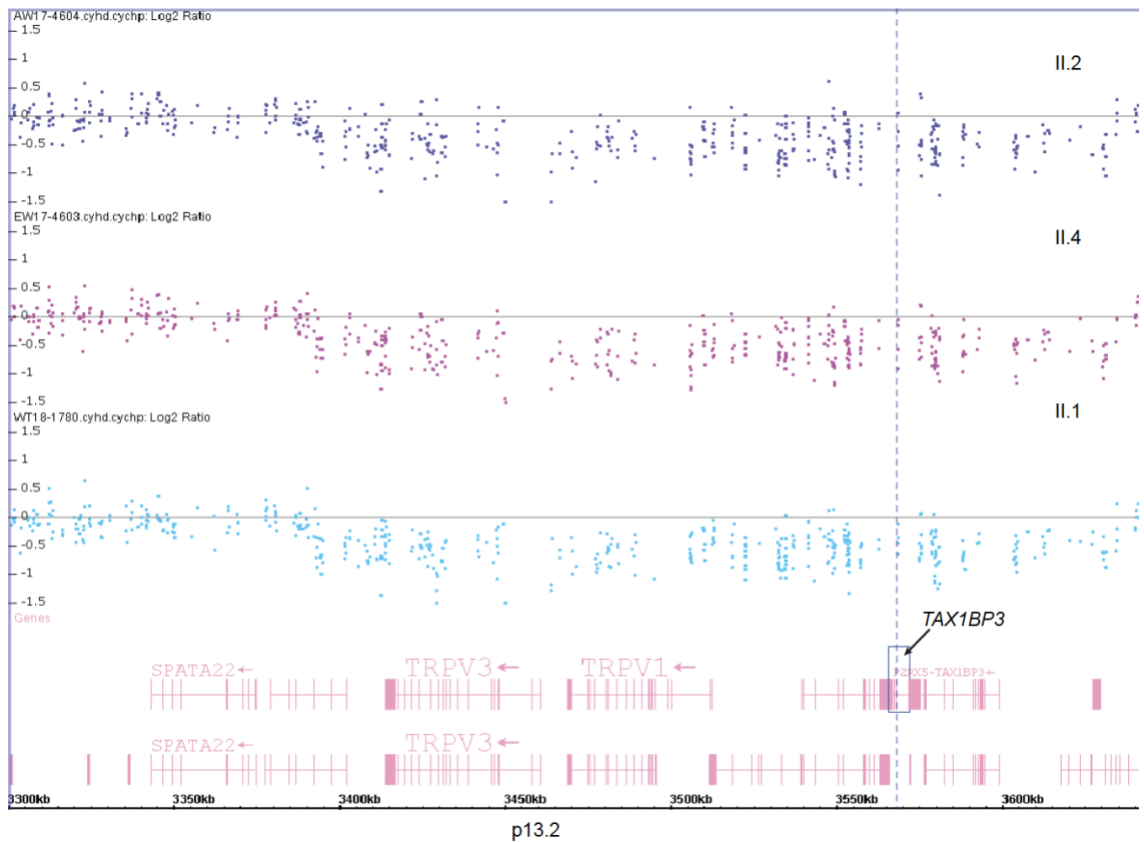


Figure 7: Chromosomal microarray analysis findings demonstrating loss of *TAX1BP3* heterozygosity

Chromosomal microarray analysis (CMA) results for individuals II.1, II.2, and II.4 showing *TAX1BP3* deletion (17p13.2). The deletion is paternally inherited and encompasses the entire *TAX1BP3* gene and is a total of 242 kb (chr17:3,392,348-3,634,096). CMA performed by the Undiagnosed Diseases Network.

Table 1: Kindred clinical and genetic information

CMA, chromosomal microarray; ACM, arrhythmogenic cardiomyopathy; Arrhy, history of arrhythmia; ADHD, attention deficit and hyperactivity disorder; DMI, diabetes mellitus type 1.

Individual	Age at diagnosis/death (years)	Age at UDN evaluation	Sex	Status	<i>TAX1BP3</i> status	CMA findings	ACM	Arrhy	ADHD	DMI
I.1	n/a	39	M	Alive	Del/WT	17p13.2(3,393,085-3,631,198)x1 <i>TAX1BP3</i> , <i>ASPA</i> , <i>TRPV3</i> , <i>TRPV1</i> , <i>SHPK</i> ,	-	-		

						<i>CTNS, P2RX5-TAX1BP3, EMC6, P2RX5, ITGAE, GSG2</i>				
I.2	n/a	41	F	Alive	M78T/ WT	n/a	-	-		
II.1	17	n/a	M	Deceased	M78T/d el	6p21.1(45,290,633-45,316,649)x1 <i>SUPT3H, RUNX2</i> 14q23.3(67,198,080-67,285,061)x1, <i>TAX1BP3, ASPA, TRPV3, TRPV1, SHPK, CTNS, P2RX5-TAX1BP3, EMC6, P2RX5, ITGAE, GSG2</i>	+	+	?	
II.2	19	20	M	Alive	M78T/d el	17p13.2(3,393,085-3,631,198)x1 <i>TAX1BP3, ASPA, TRPV3, TRPV1, SHPK, CTNS, P2RX5-TAX1BP3, EMC6, P2RX5, ITGAE, GSG2</i>	+	+	+	-
II.3	n/a	17	F	Alive	WT/WT	Normal female	-	-	-	-
II.4	14	14	M	Alive	M78T/d el	3p26.3(858,547-1,450,741)x1 <i>CNTN6</i> 14q23.3(67,198,080-67,285,061)x1 <i>GPHN</i> 17p13.2(3,392,348-3,634,096)x1 <i>TAX1BP3, ASPA, TRPV3, TRPV1, SHPK, CTNS, P2RX5-TAX1BP3, EMC6, P2RX5, ITGAE, GSG2</i>	+	+	+	+

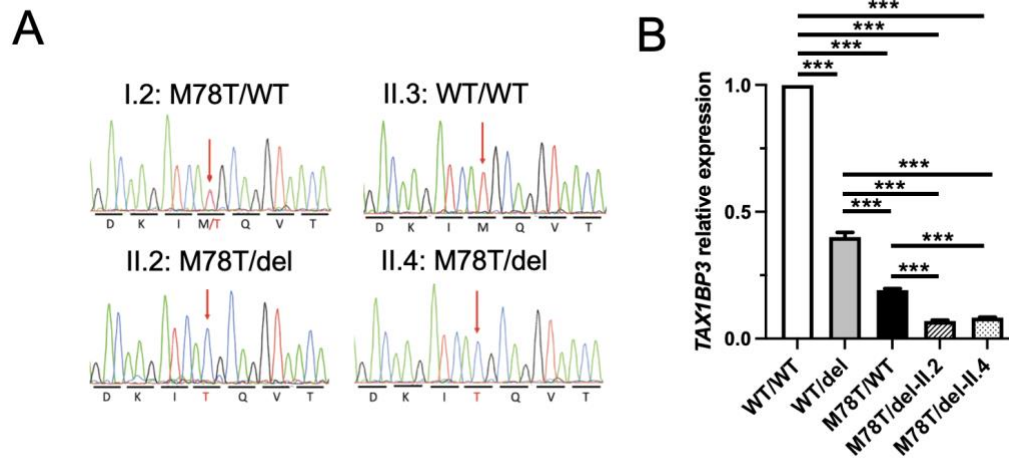


Figure 8: Sanger sequencing validation and *TAX1BP3* expression

A) Sanger sequencing chromatograms of wild type, heterozygous variant p.M78T, and compound heterozygous p.M78T/del. B) qPCR from whole blood of *TAX1BP3* mRNA (Mean \pm s.e.m. n = 3; 3; 3; 3; 3, all comparisons: p < 0.0001 except M78T/del-II.1 vs M78T/del II.4: not significant. * p < 0.05, ** p < 0.01, *** p < 0.001. Sanger sequencing performed by Bo Sun and qPCR performed by Qixin Yang.

Table 2: In silico variant prediction aggregate analysis of the TAX1BP3-M78T variant

Tool	Algorithm	Clinical Significance	Result	Results Range
PolyPhen-2	Naïve Bayes classification	Possibly Damaging	0.919	0-1, 1 = Deleterious
SIFT	Sequence conservation	Deleterious	0.02	<0.05 = Deleterious
Panther	Position-specific evolutionary preservation	Probably Damaging	750	Probably damaging: >450my Possibly damaging: 200-250my Probably benign: 0-200my
Provean	Protein variation effect analyzer	Deleterious	-3.625	Deleterious < -2.5 < neutral
MUpro	Protein stability prediction	Decrease Stability	-1.597	Decreases stability < 0 < increases stability
Revel	An ensemble method for predicting the pathogenicity of missense variants based on a combination of scores from 13 individual tools	Deleterious (low)	0.62	0 to 1, with higher scores reflecting greater likelihood that the variant is disease-causing

4. Novel iPSC-CM model of arrhythmogenic cardiomyopathy

4.1 Generation of iPSC-CM^{M78T/del}

To study the role TAX1BP3 in the heart, we generated induced pluripotent stem cells (iPSCs) from the patient peripheral blood mononuclear cell (PBMC) lines from the two surviving affected brothers (II.2 and II.4, p.M78T/del) and the sister to use as the control (II.3, WT/WT). We validated that the iPSC lines expressed iPSC markers OCT4 and NANOG with immunofluorescence (**Figure 9**). We then differentiated the iPSCs into cardiomyocytes (iPSC-CMs) and confirmed the TAX1BP3-M78T variant status in the iPSC-CMs by Sanger sequencing (**Figure 10A**). Differentiation to cardiomyocytes was validated by immunofluorescence of cardiomyocyte marker TNNT2 and robust beating of cells in the dish (**Figure 10B**). Reduction of TAX1BP3 protein was confirmed in the iPSC-CMs with Western blot (**Figure 11A,B**).

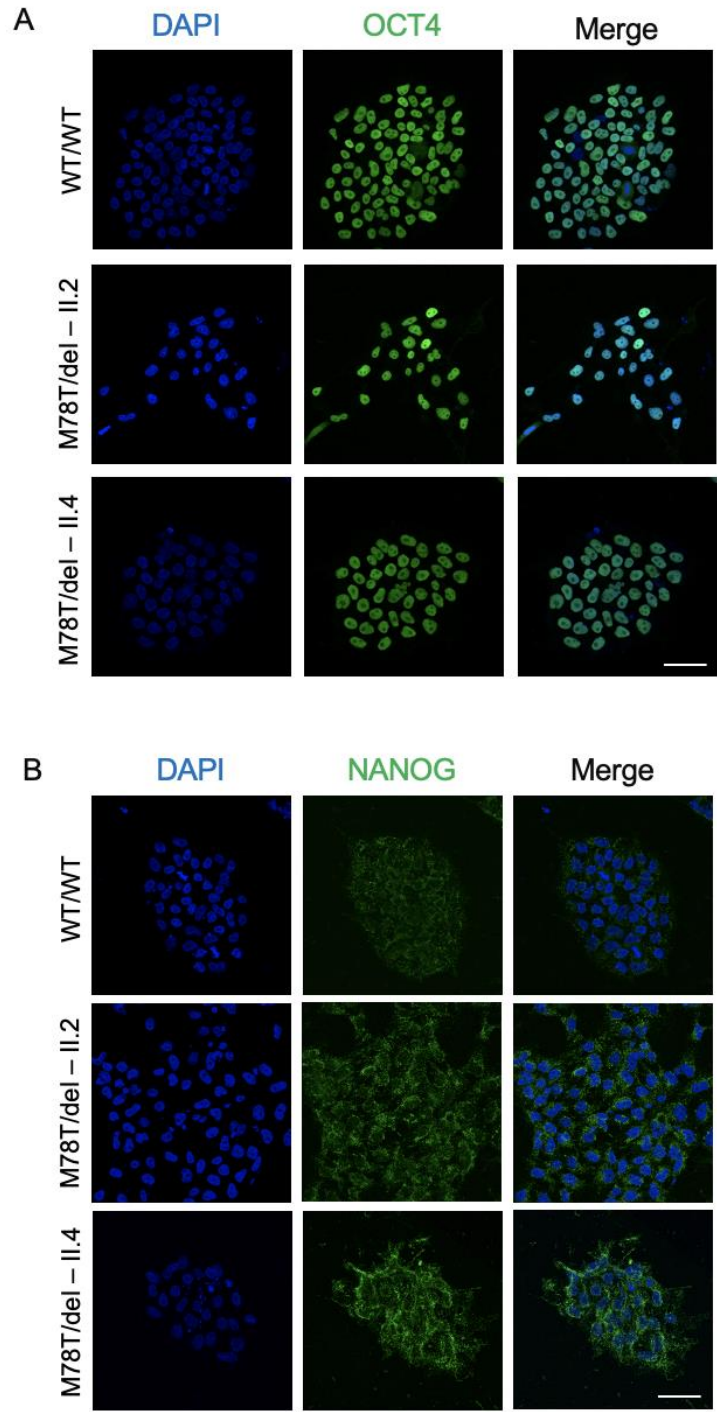


Figure 9: Validation of TAX1BP3 induced pluripotent stem cells (iSPCs)

A,B) Immunofluorescence for iPSC markers OCT4 (green) or NANOG (green) and DAPI (blue) on the three iPSC lines: II.2 (M78T/del), II.3 (WT/WT), and II.4 (M78T/del). Scale bar = 50 μ m. Imaging done by Leonie Kurzlechner.

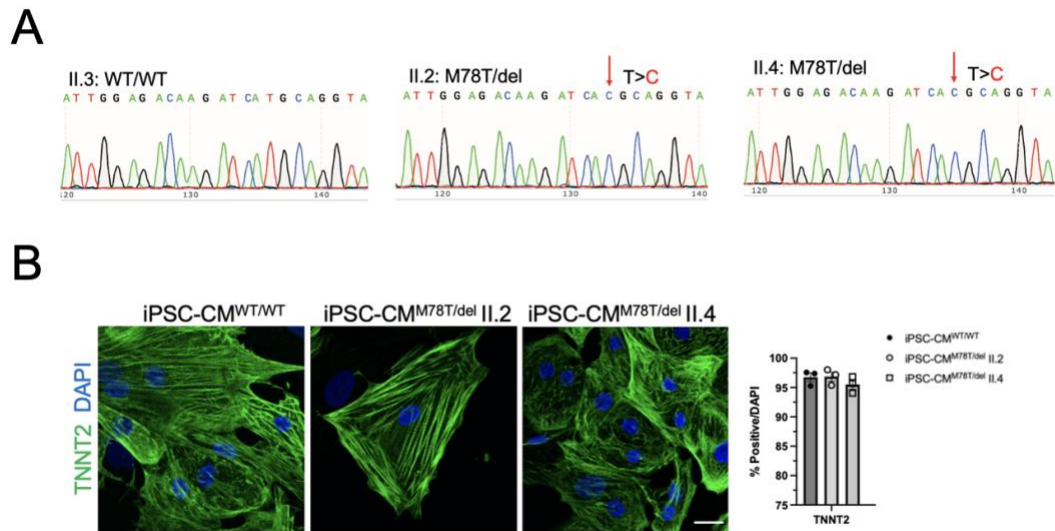


Figure 10: Validation of induced pluripotent stem cell-derived cardiomyocytes (iPSC-CMs)

A) Sanger sequencing of induced pluripotent stem cell-derived cardiomyocytes (iPSC-CMs) to confirm T>C missense variant in II.2 and II.4. B) Immunofluorescence examples of DAPI (blue) and TNNT2 (green) positive iPSC-CMs. Scale bar = 20 μ m. Quantification of TNNT2 cells per DAPI positive cell (Mean \pm s.e.m. n = 3; 3; 3). Quantification in B done by Anna Poněk.

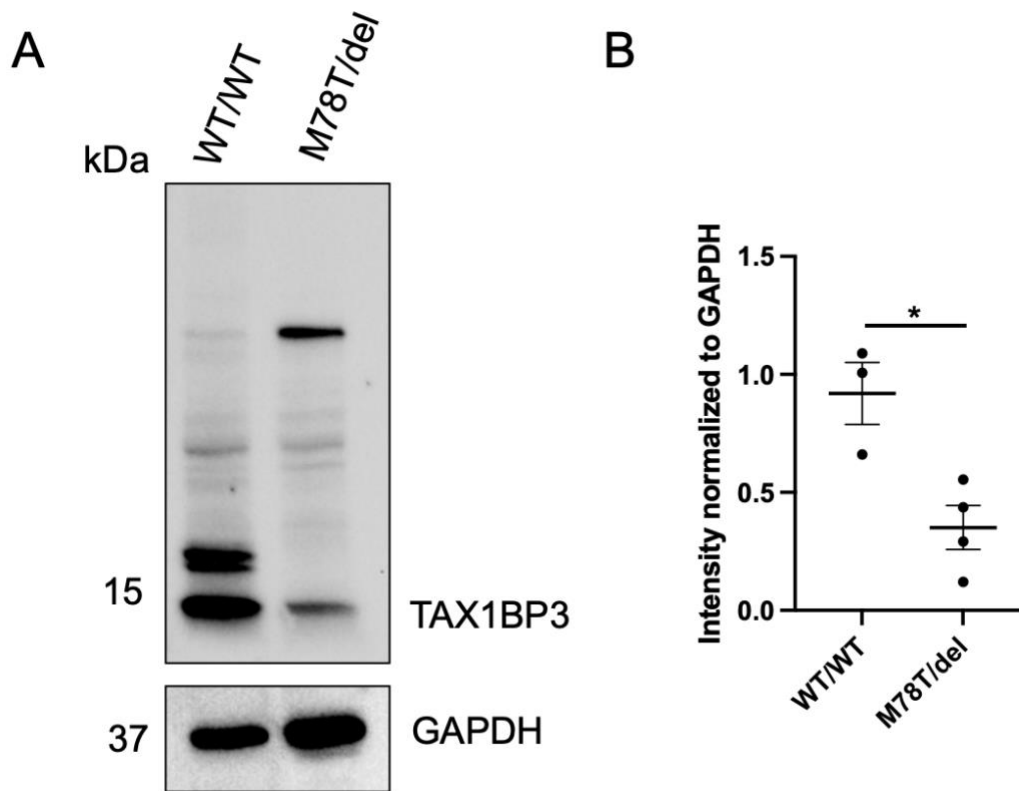


Figure 11: Reduced TAX1BP3 protein expression in iPSC-CM^{M78T/del}

A) Example Western blot of iPSC-CMs showing decrease of TAX1BP3 protein in iPSC-CM^{M78T/del}. B) Quantification of A and additional Western blots. Each data point is from a different differentiation of iPSC-CMs (Mean \pm s.e.m. n = 3;4, p = 0.0149). * p < 0.05, ** p < 0.01, *** p < 0.001.

4.2 iPSC-CM^{M78T/del} have increased intracellular lipid droplet accumulation

Because ACM is associated with fibro-fatty infiltration, we hypothesized that the affected iPSC-CMs would be susceptible to fat accumulation. We applied the 3 factor (3F) reagent protocol to stimulate lipogenesis (Kim, Wong et al. 2013) and found that this media resulted in lipid droplets in both the iPSC-CM^{WT/WT} and iPSC-CM^{M78T/del} lines, but the iPSC-CM^{M78T/del} lines had more than double the quantity of fat accumulation (**Figure 12 A-C**). To validate that the protocol was indeed inducing a lipogenesis-state, we performed RT-qPCR for lipogenesis genes *PPARG* and *CEBPA*

and found that both were upregulated following treatment with the 3F media (**Figure 13**). The increase in lipid droplets in the iPSC-CM^{M78T/del} lines suggests that genetic loss of *TAX1BP3* predisposes iPSC-CMs to undergo lipogenic remodeling of the cardiac myocytes, reflective of a distinguishing property of ACM (Austin, Trembley et al. 2019).

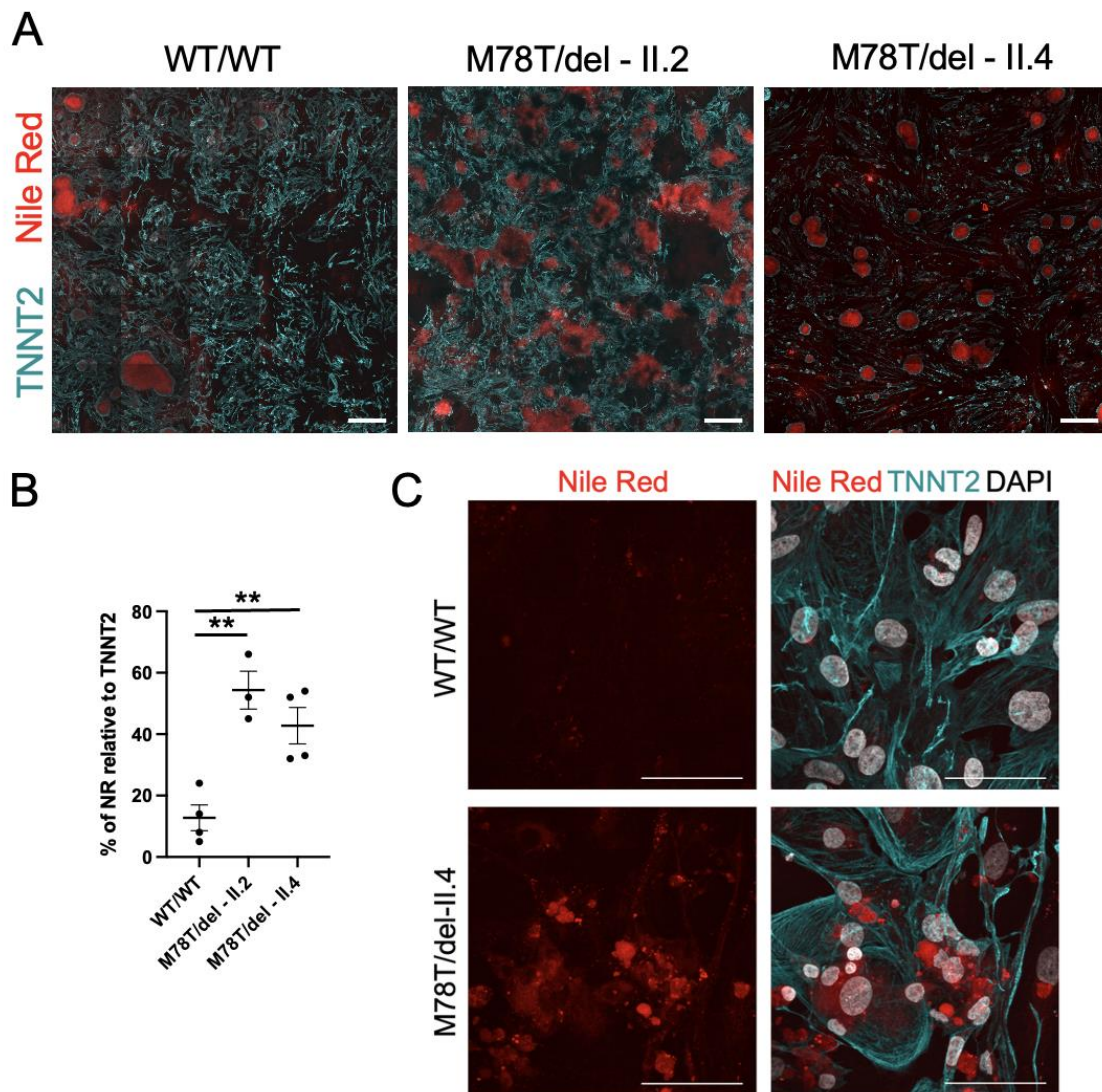


Figure 12: Lipid accumulations in fat-stressed iPSC-CMs

A) Confocal images of iPSC-CM^{WT/WT} and iPSC-CM^{M78T/del} lines showing immunofluorescence TNNT2 (cyan) and Nile Red (red, lipids). Scale bar = 500 μ m. Quantification of the percentage of Nile Red fluorescence relative to TNNT2 fluorescence (Mean \pm s.e.m. n = 4; 3; 4, p = 0.0018, WT/WT vs. M78T/del - II.2: p = 0.0014, WT/WT vs. M78T/del - II.4: p = 0.0065). C) 63X

Confocal z-stack images of Nile Red (red), TNNT2 (cyan), and DAPI (white) in iPSC-CM^{WT/WT} and iPSC-CM^{M78T/del} lines. Scale bars = 50 μ m. * p < 0.05, ** p < 0.01, *** p < 0.001.

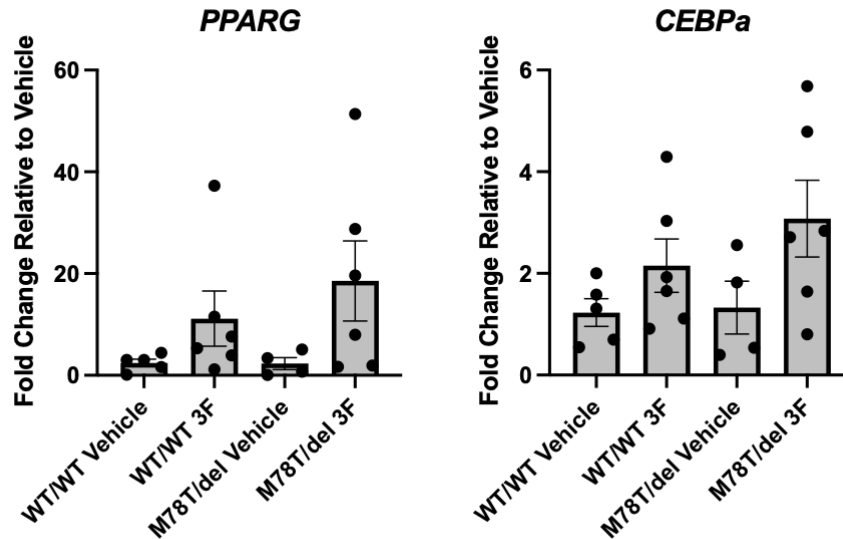


Figure 13: RNA expression in fat-stressed iPSC-CMs

RT-qPCR for *PPARG* and *CEBPa* of iPSC-CMs following vehicle or 3F treatment. 3F treatments for both iPSC-CM^{WT/WT} and iPSC-CM^{M78T/del} lines were normalized to the vehicle treatment of each line (Mean \pm s.e.m. n differentiations= 5; 6; 4; 6, not significant).

4.3 iPSC-CM^{M78T/del} demonstrates pro-arrhythmogenic Ca²⁺ leak from the sarcoplasmic reticulum

Given the marked arrhythmogenic phenotype of the genotype-positive kindred, we hypothesized that the iPSC-CMs^{M78T/del} lines would have a Ca²⁺-overload state marked by pathologic Ca²⁺ leak from the SR store – a known mechanism of arrhythmogenesis (Voigt, Li et al. 2012, Hoang-Trong, Ullah and Jafri 2015, Cerrone, Montnach et al. 2017, Mohamed, Hartmann et al. 2018). To assess Ca²⁺ dynamics, we examined calcium transients using live cell calcium imaging finding that iPSC-CM^{M78T/del} paced at 0.5Hz demonstrated increased Ca²⁺ transient amplitude compared to iPSC-

CM^{WT/WT} (**Figure 14A and B**). In addition, SR store Ca²⁺ was lower in iPSC-CM^{M78T/del} compared to iPSC-CM^{WT/WT} (**Figure 14C and D**). There was no significant difference in diastolic Ca²⁺ as measured by Fura-2 AM 340/380 ratios (**Figure 14E**). Together, these results suggest that the variants in *TAX1BP3* result in shifting of the intracellular Ca²⁺ out of the SR store.

Due to the decrease in SR store in the iPSC-CM^{M78T/del} lines, we wanted to explore if there was a change in SERCA2, the pump that returns Ca²⁺ back into the SR, in the iPSC-CM^{M78T/del} compared with iPSC-CM^{WT/WT}. There were no clear changes in NCX or SERCA2 protein expression (**Figure 15A and B**). Phospholamban (PLN), a negative regulator of SERCA2, also did not have any differences in protein expression, nor were there differences in the protein kinase A phosphorylation site at serine 16 on PLN (**Figure 15C and D**). We then utilized the live Ca²⁺ imaging to calculate NCX and SERCA2 activity by measuring the tau of decay for calcium transients and the tau after 10mM caffeine. With high dose of caffeine, the removal of Ca²⁺ is predominately dictated by NCX, whereas during regular calcium transients the largest contributions of Ca²⁺ removal from the cytoplasm is by reuptake of Ca²⁺ into the SR by SERCA and by extrusion from the cell by NCX. Thus, one can estimate NCX and SERCA activity from the following equations: SERCA activity = $1/\tau_{\text{transient}} - 1/\tau_{\text{caffeine}}$ and NCX activity = $1/\tau_{\text{caffeine}}$. The iPSC-CM^{M78T/del} showed significant differences in SERCA or NCX activity compared with iPSC-CM^{WT/WT} (**Figure 15E**).

We next hypothesized that SR store Ca²⁺-leak would be increased in the mutant cells, contributing to the reduced SR store. Indeed, we found that the iPSC-CM^{M78T/del} lines have greater spark frequency and Ca²⁺ leak from the SR via RyR2, especially in cells from II.4, the donor who is more arrhythmic in the kindred (**Figure 16A and B**). This difference was more pronounced when this leak was normalized to the relatively low SR store to account for the total amount of Ca²⁺ available (**Figure 16C**). The iPSC-CM^{M78T/del} lines also trended towards a greater percentage of

cells with spontaneous Ca^{2+} release during pacing. Specifically, iPSC-CM^{M78T/del} cells exhibited an increased propensity for delayed-after depolarization-like spontaneous Ca^{2+} release events (**Figure 17A and B**), a known cellular etiology for triggered arrhythmogenesis of the myocardium. Moreover, some iPSC-CM^{M78T/del} cells also demonstrated significant runs of spontaneous Ca^{2+} release events (**Figure 17C**). These findings suggest that the mechanism of reduced SR store and the arrhythmogenesis in the affected kindred from *TAX1BP3* loss is due to Ca^{2+} leak from RyR2.

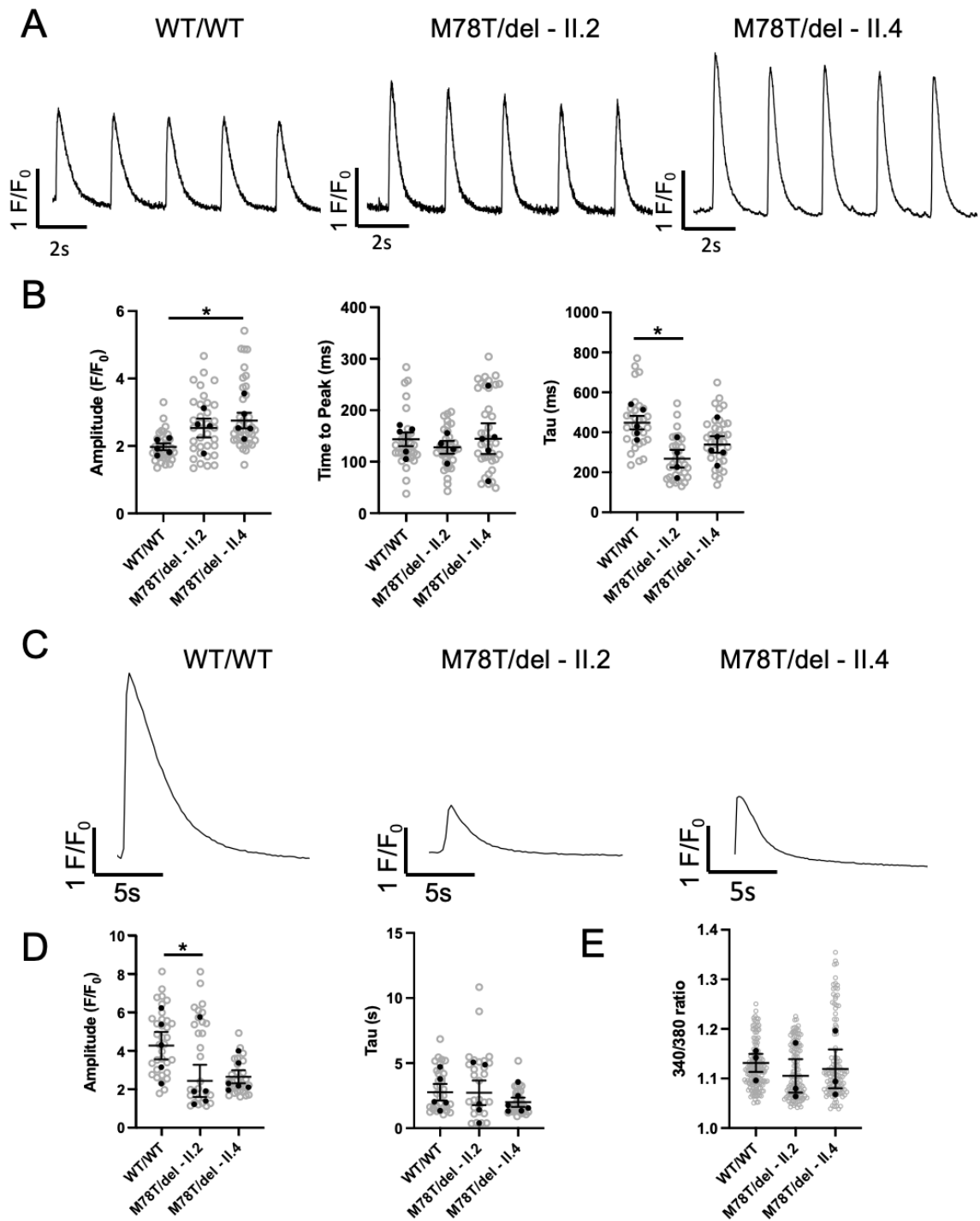


Figure 14: iPSC-CM^{M78T/del} have differences in Ca²⁺ handling

A) Example Ca²⁺ transient traces of iPSC-CMs taken from line scans while cells were paced at 0.5Hz. B) Quantifications of Ca²⁺ transient amplitude (Mean ± s.e.m, n differentiations = 5; 4; 5, n

cells = 31; 34; 37, WT/WT vs. M78T/del – II.2: $p = 0.057$, WT/WT vs. M78T/del – II.4: $p = 0.006$), time to peak (Mean \pm s.e.m, n differentiations = 5; 4; 5, n cells = 31; 34; 37, not significant), tau (Mean \pm s.e.m, n differentiations = 5; 4; 5, n cells = 31; 34; 37, WT/WT vs. M78T/del – II.2: $p = 0.005$, WT/WT vs. M78T/del – II.4: not significant). C) Example Ca^{2+} traces of iPSC-CMs following treatment with 10mM caffeine to trigger SR store Ca^{2+} release. D) Quantifications of SR store Ca^{2+} release amplitude (Mean \pm s.e.m, n differentiations = 5; 5; 6, n cells = 34; 28; 31, WT/WT vs. M78T/del – II.2: 0.0186, WT/WT vs. M78T/del – II.4: not significant) and tau (Mean \pm s.e.m, n differentiations = 5; 5; 6, n cells = 34; 28; 31, not significant). E) Quantification of 340/380 ratio of Fura-2 fluorescence measuring intracellular Ca^{2+} levels (Mean \pm s.e.m, n = 158; 132; 98, not significant. $p < 0.01$. * $p < 0.05$, ** $p < 0.01$, *** $p < 0.001$)

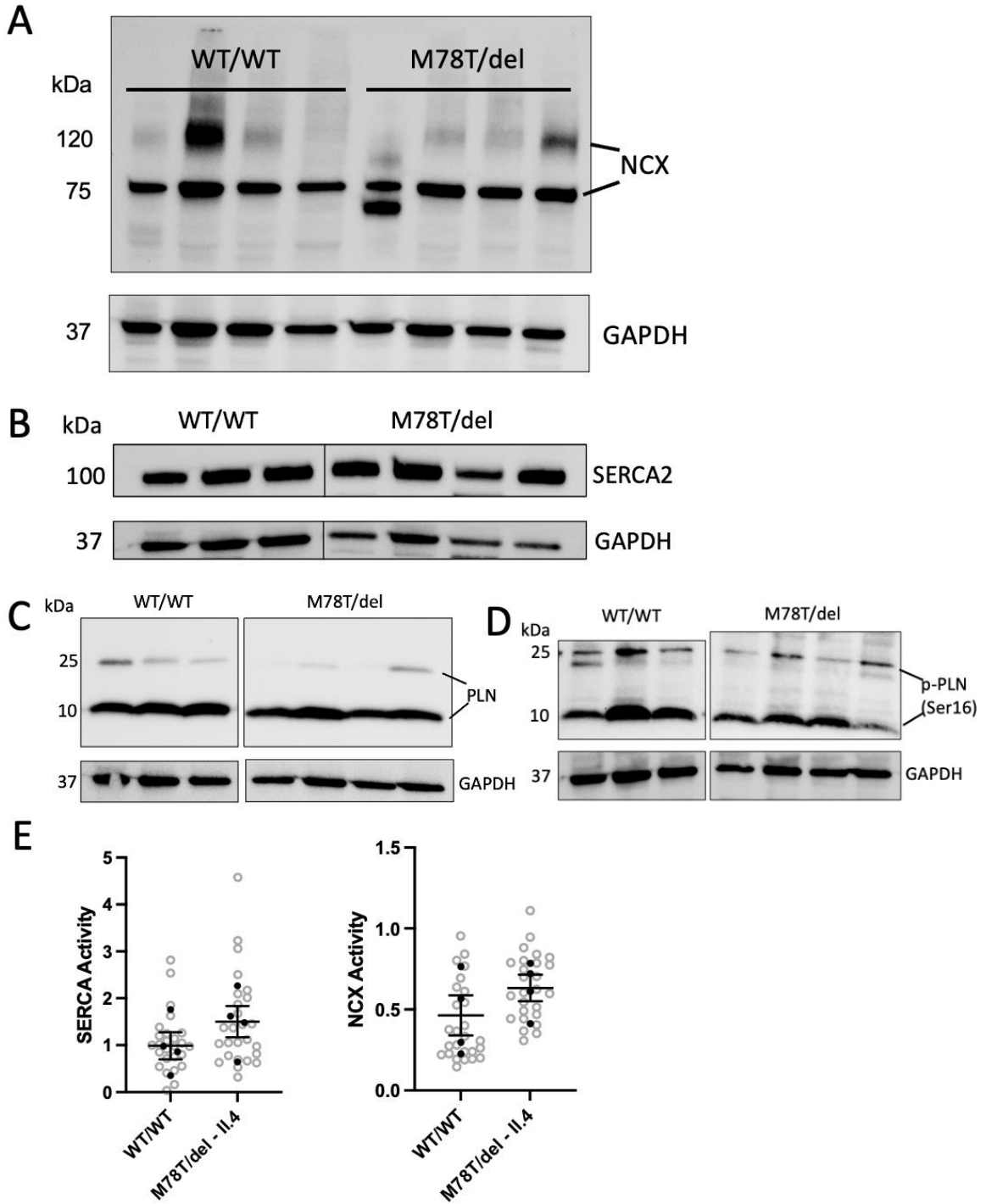


Figure 15: No change in NCX, SERCA2, or PLN protein expression or SERCA and NCX activity
 A-D) Western blots on iPSC-CM^{WT/WT} and iPSC-CM^{M78T/del} cells for NCX, SERCA2, PLN, and phospho-PLN (Ser16), respectively. Each lane is a separate differentiation. E) Quantification of

SERCA2 and NCX activity calculated from live calcium imaging. SERCA2 activity was calculated as $1/\tau_{\text{transient}} - 1/\tau_{\text{caffeine}}$ and NCX activity was calculated as $1/\tau_{\text{caffeine}}$.

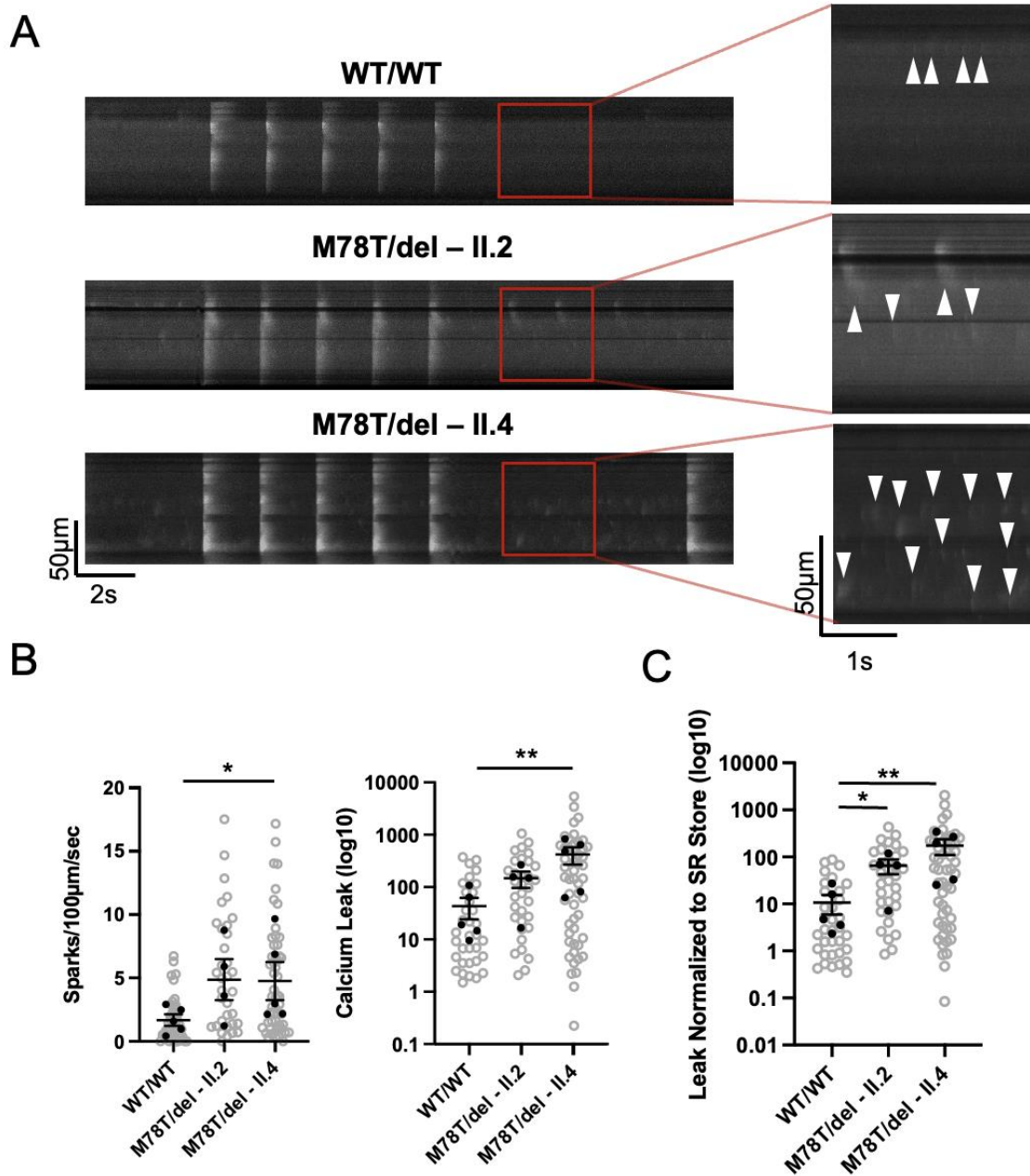


Figure 16: iPSC-CM^{M78T/del} have greater spark frequency and Ca²⁺ leak

A) Representative examples of confocal line scans with insets showing example regions of interest showing Ca^{2+} sparks (white arrows) B) Quantifications of spark frequency (Mean \pm s.e.m, n differentiations = 5; 4; 5, n cells = 41; 34; 53, WT/WT vs. M78T/del – II.2: not significant, WT/WT vs. M78T/del – II.4: $p = 0.0459$) and leak (Mean \pm s.e.m, n differentiations = 5; 4; 5, n cells = 41; 34; 53, $p < 0.001$, WT/WT vs. M78T/del – II.2: not significant, WT/WT vs. M78T/del – II.4: $p = 0.022$). C) Quantification of Ca^{2+} leak normalized to SR store (average amplitude per cell line of caffeine induced Ca^{2+} release) (Mean \pm s.e.m, n differentiations = 5; 4; 5, n cells = 41; 34; 53, WT/WT vs. M78T/del – II.2: $p = 0.0164$, WT/WT vs. M78T/del – II.4: $p = 0.0032$). * $p < 0.05$, ** $p < 0.01$, *** $p < 0.001$

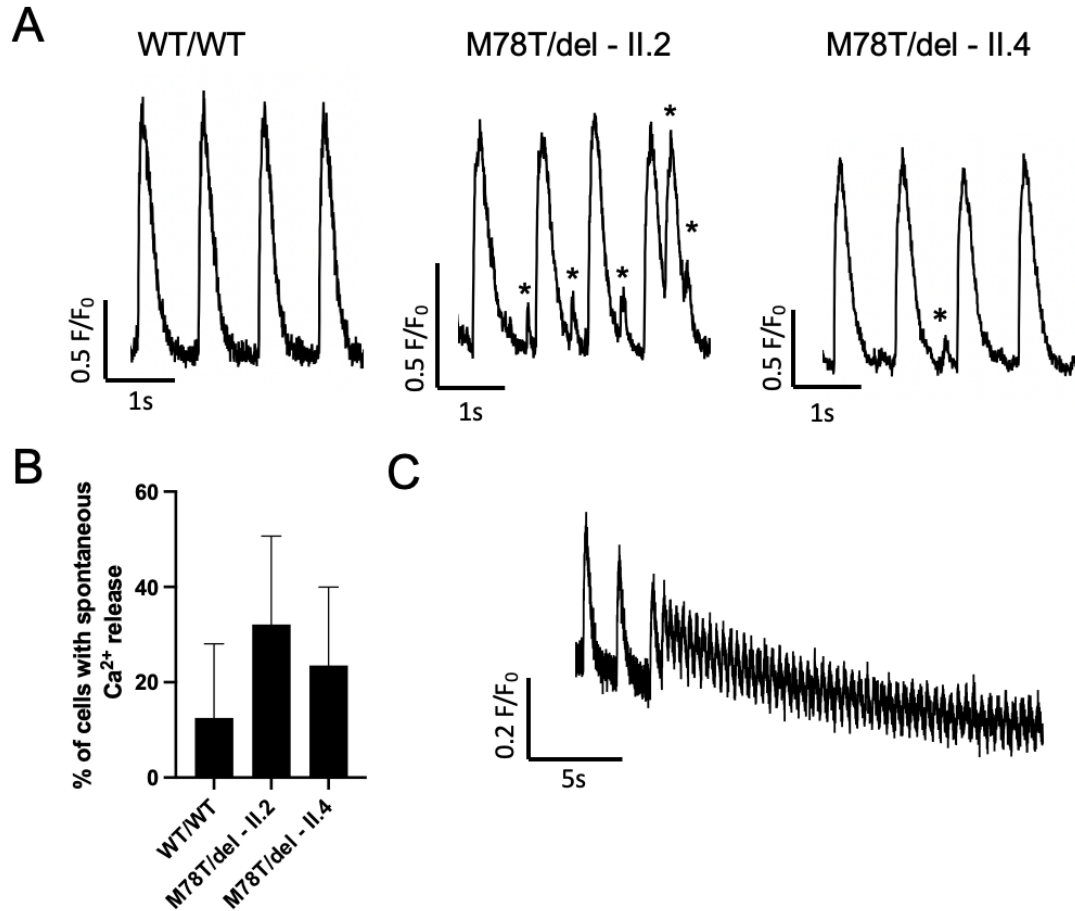


Figure 17: iPSC-CMM78T/del have spontaneous Ca^{2+} release and inducible sustained cellular arrhythmias

A) Example Ca^{2+} fluorescent traces of iPSC-CMs during pacing. Asterisks denote spontaneous Ca^{2+} release. B) Quantification of the percentage of cells with spontaneous Ca^{2+} release with 95% confidence interval, n = 32; 28; 34, not significant. C) An example trace from iPSC-CM^{M78T/del} II.4 iPSC-CMs with a triggered sustained arrhythmia.

TAX1BP3 overexpression rescues Ca²⁺ leak

To confirm that the Ca²⁺ leak phenotype is specifically due to loss of *TAX1BP3*, we overexpressed wildtype *TAX1BP3* in the iPSC-CM^{M78T/del} cells and hypothesized that *TAX1BP3* would be sufficient to suppress calcium leak. To do this, we used *EF1A-TAX1BP3-T2A-mCherry* packaged into a lentivirus to deliver *TAX1BP3* or *TAX1BP3-M78T* (**Figure 18A**). As a control, we delivered the same construct with mCherry alone. We validated the transduction was successful by imaging red fluorescence produced by mCherry and by performing a Western blot to validate greater *TAX1BP3* protein expression (**Figure 18 B and C**). We then repeated the same Ca²⁺ imaging studies with the transduced cells and found that *TAX1BP3* overexpression decreased Ca²⁺ leak (**Figure 19A and B**). This suggests that *TAX1BP3* loss is the cause of the increased Ca²⁺ leak in this model. Interestingly, the cells transduced with *TAX1BP3-M78T* version also had reduced Ca²⁺ leak compared with control (**Figure 19A and B**). However, based on the Western blot, about the same quantity of overexpressed *TAX1BP3* protein was produced in both cases, whereas the qPCR of the mother's whole blood (I.2, genotype WT/M78T, Figure 8B) showed a drastic reduction in *TAX1BP3* mRNA. Thus, it is possible that the p.M78T variant affects the production of *TAX1BP3* by affecting splicing, but more work is needed to determine the exact effects of p.M78T.

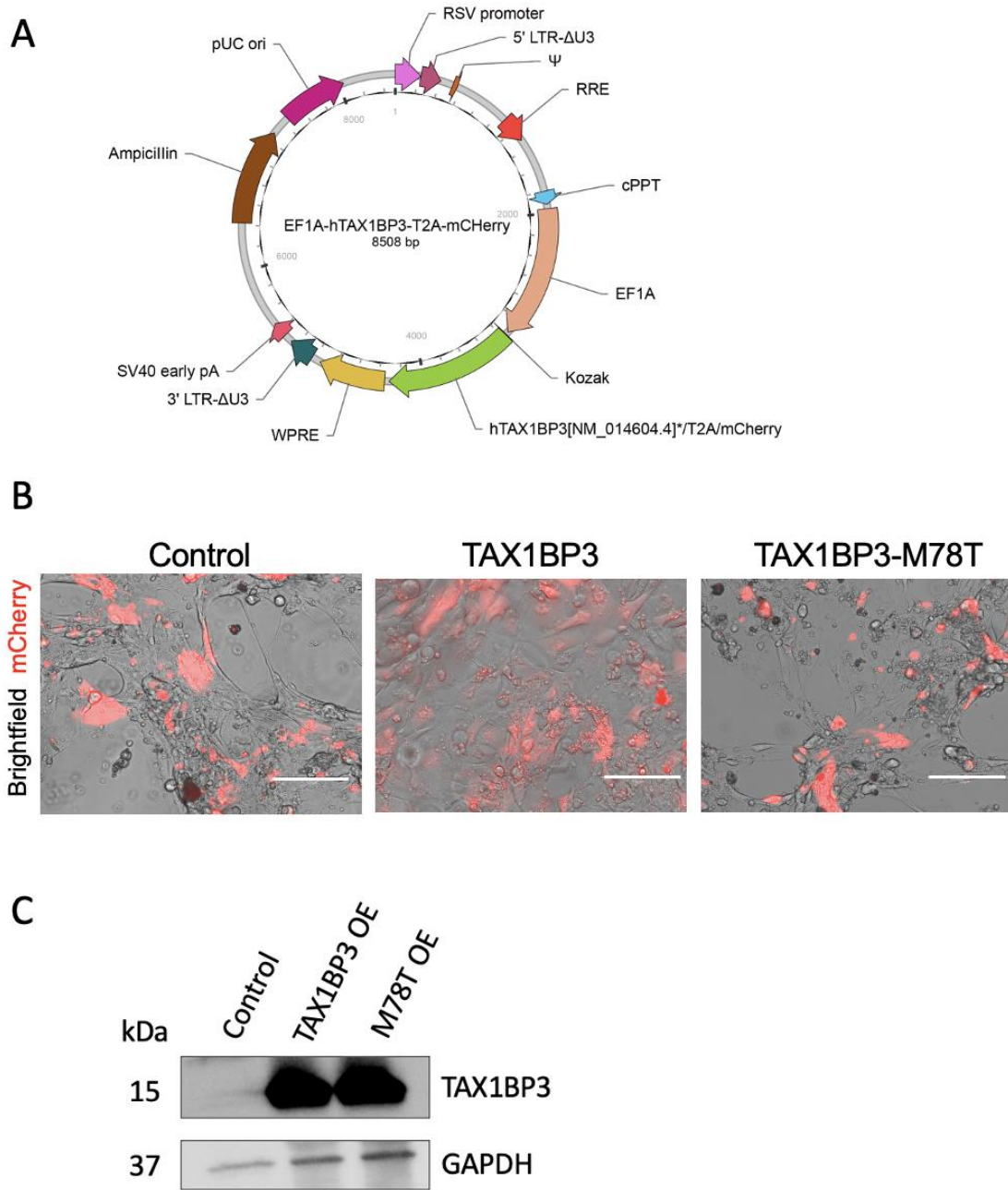


Figure 18: TAX1BP3 lentivirus overexpression in iPSC-CM^{M78T/del}

A) Lentivirus vector map for TAX1BP3 overexpression. B) Representative images showing lentivirus transduced iPSC^{M78T/del} cells in red (mCherry) overlaid with brightfield. Scale bar = 125 μ m. C) Western blot of iPSC-CM^{M78T/del} cells transduced with control, TAX1BP3, or TAX1BP3-M78T lentivirus.

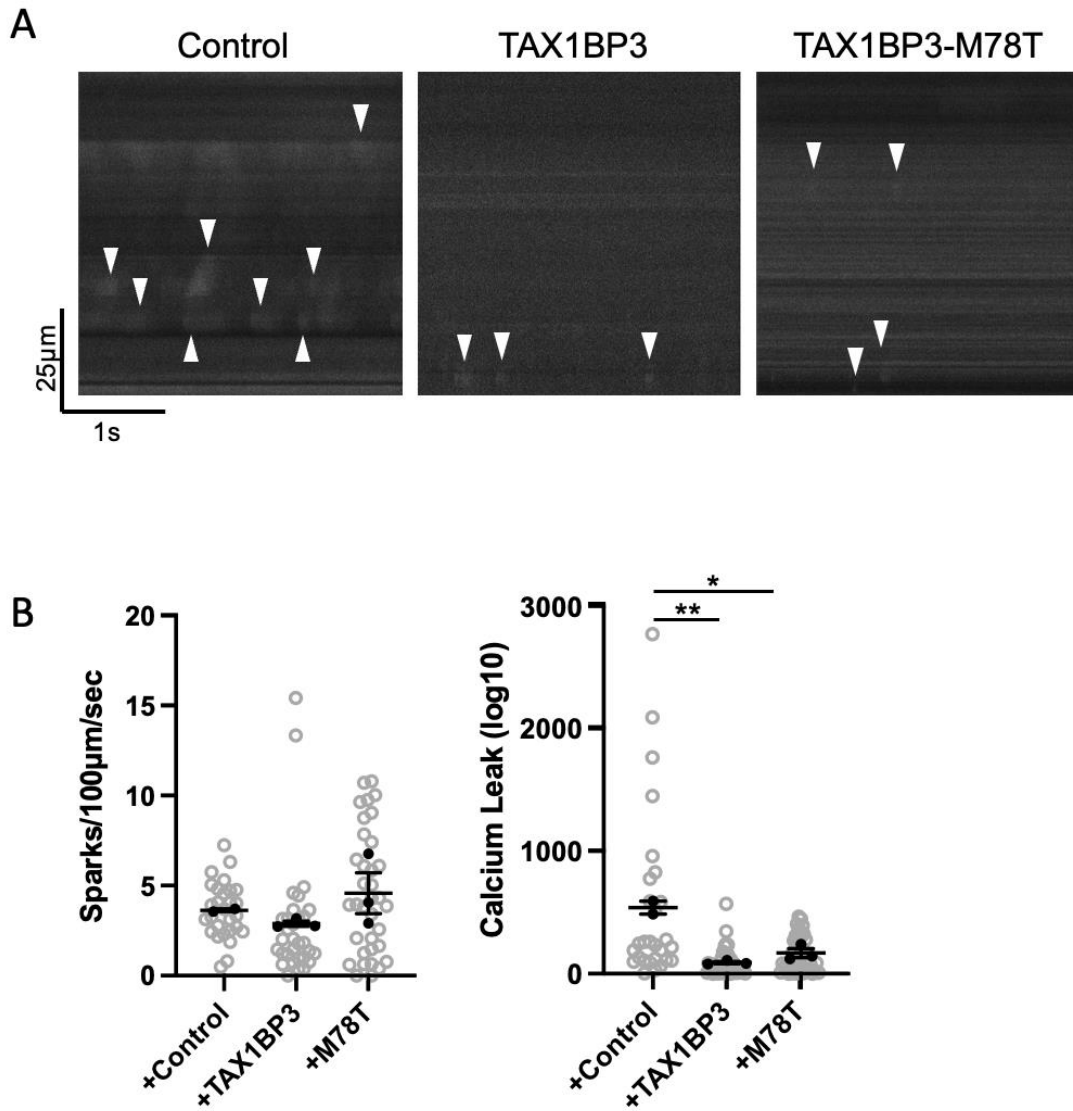


Figure 19: TAX1BP3 overexpression rescues Ca²⁺ leak

A) Representative confocal line scan images of Ca²⁺ sparks (examples denoted by white arrows).
 B) Quantification of spark frequency (Mean ± s.e.m, n differentiations = 2; 3; 3, n cells = 28; 40; 47) and Ca²⁺ leak (Mean ± s.e.m, n differentiations = 2; 3; 3, n cells = 28; 40; 47, control vs. TAX1BP3: p = 0.0015, control vs. M78T: p = 0.0239, TAX1BP3 vs. M78T: p = 0.065). * p < 0.05, ** p < 0.01, *** p < 0.001

5. Inducible, cardiac-specific *Tax1bp3* knockout mouse model

5.1 Inducible, cardiac-specific *Tax1bp3* knockout mice have increased Ca^{2+} leak and ventricular arrhythmias

To determine the effect of *TAX1BP3* loss in an *in vivo* model, we generated an inducible, cardiomyocyte-specific *Tax1bp3* knockout mouse (*Tax1bp3*^{-/-}) by crossing mice harboring *Tax1bp3* alleles with loxP sites flanking exons 2-4 with the alpha-MHC MerCreMer (MCM) mouse (**Figure 20**). Cre induction resulted in a reduction of *Tax1bp3* protein from ventricle myocardium while not altering *Tax1bp3* expression levels in non-cardiac organs (**Figure 21**). To test for evidence of cardiomyopathic remodeling, we performed transthoracic echocardiograms of conscious mice and processed *Tax1bp3*^{-/-} hearts for myocardial histology analysis to look for evidence of cardiac remodeling. There were no differences in the LV dimensions or systolic function by echocardiogram (**Figure 22**). We found no significant changes in the LV dimensions, ventricular wall thickness, or other structural abnormalities by H&E staining of the whole hearts. Further, we found no evidence of myocardial fibrosis, and no evidence of adipose deposition/remodeling, as assessed by Masson's Trichrome and Oil Red-O staining, respectively (**Figure 23**). Given the evidence of Ca^{2+} -mediated arrhythmogenesis in the iPSC-CM models, we next assessed whether reduced *Tax1bp3* expression causes increased Ca^{2+} leak from the SR. To do this, we Langendorff-perfused hearts from *Tax1bp3*^{-/-} and *Tax1bp3*^{+/+} mice to isolate ventricular myocytes and then performed live-cell Ca^{2+} imaging following Cal520 dye loading. We found that primary ventricular myocytes from *Tax1bp3*^{-/-} mice had greater Ca^{2+} spark frequency and Ca^{2+} leak compared with *Tax1bp3*^{+/+} mice (**Figure 24**). Interestingly, there was no difference in the Ca^{2+} transient amplitude as there was with the iPSC-CMs, but there was an increase in time to peak (**Figure 25**).

To evaluate arrhythmia inducibility *in vivo*, we next performed both ECG and intracardiac electrophysiology studies with programmed electrical stimulation. While there were no differences in surface ECG measurements (**Figure 26**), 30% of *Tax1bp3*^{-/-} mice had sustained ventricular tachycardia immediately following programmed electrical stimulation of the ventricular myocardium, while *Tax1bp3*^{+/+} mice demonstrated no sustained ventricular arrhythmias (**Figure 27**). One *Tax1bp3*^{-/-} mouse had sustained VT for over 20 minutes that never resolved. All but one mouse with VT had the VT occur after caffeine and isoproterenol were given. Taken together, these data indicate that loss of *Tax1bp3* does not result in heart failure or cardiomyopathic remodeling yet increases ventricular arrhythmia predisposition and intracellular Ca²⁺ leak, *in vivo* at 6 months.

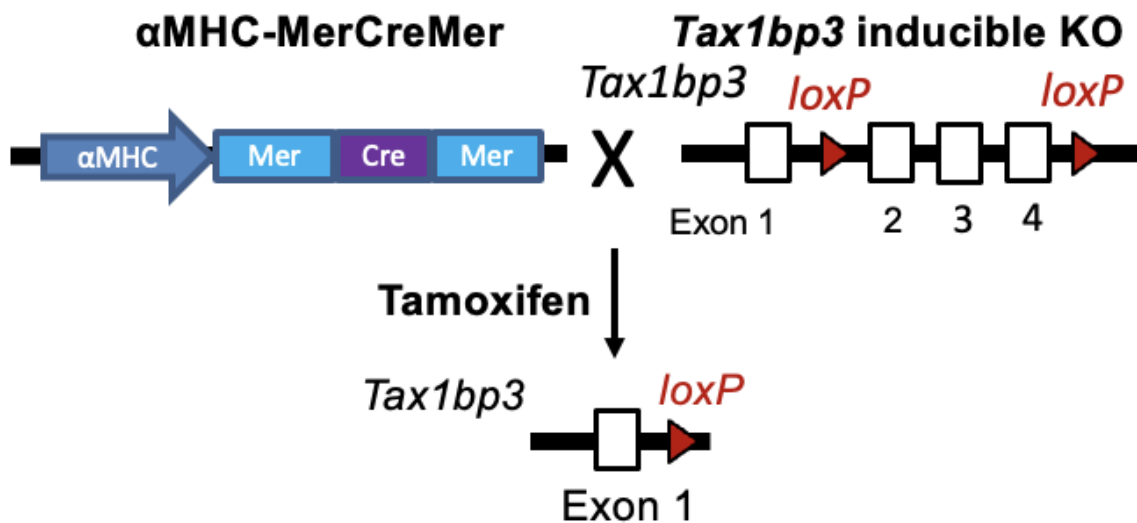


Figure 20: Generation of inducible, cardiac-specific *Tax1bp3*^{-/-} mice

Schematic showing inducible, cardiac specific *Tax1bp3*^{-/-} mouse breeding strategy. LoxP sites flank *Tax1bp3* exons 2-4, such that when Cre is expressed, only Exon 1 remains. MerCreMer is under the alpha Myosin Heavy Chain (alphaMHC) promoter so that Cre is only expressed in cardiomyocytes. Tamoxifen is injected when mice are 1.5 months old to induce Cre expression.

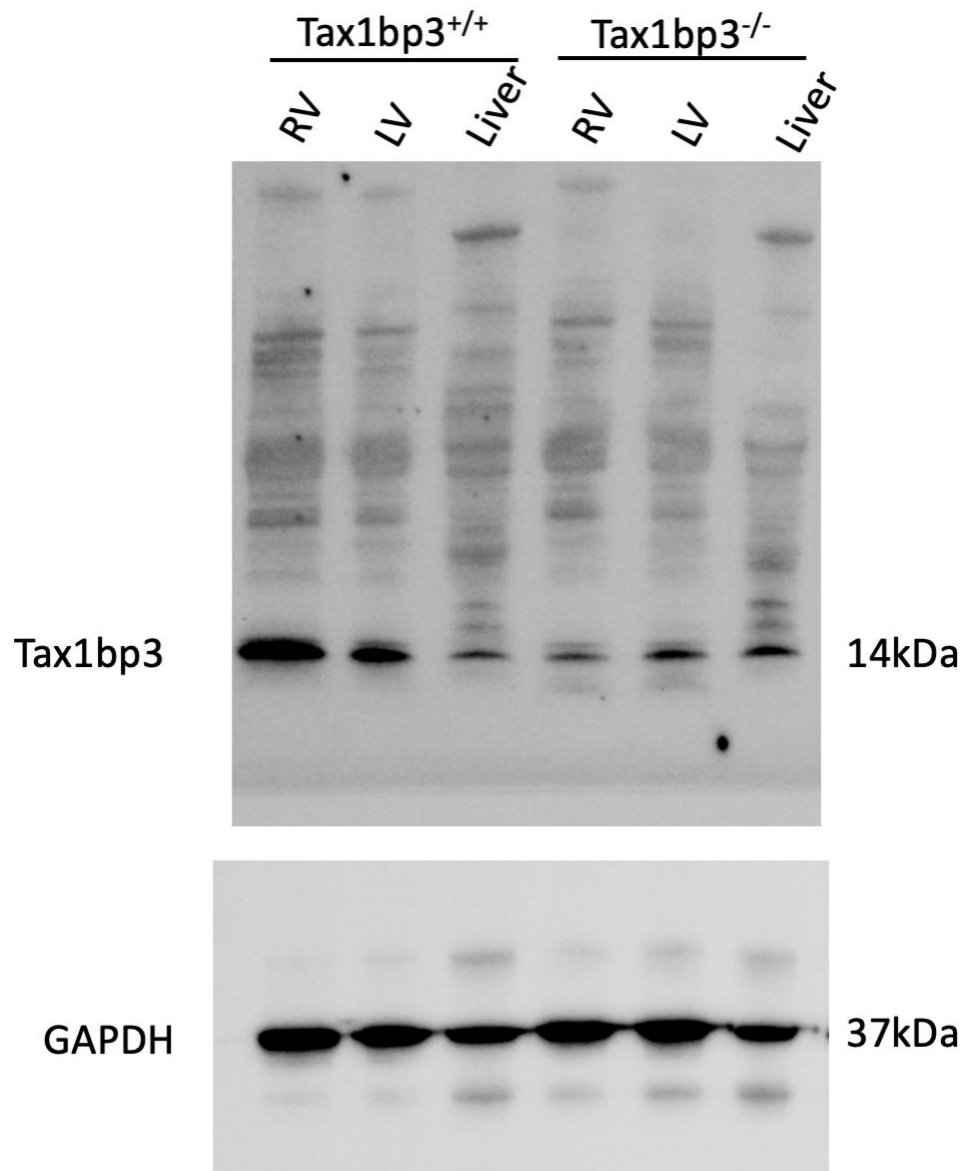


Figure 21: Full Western blot of Tax1bp3 reduced ventricular protein expression in *Tax1bp3*^{-/-} mice

Western blot on lysate from the right ventricle (RV), left ventricle (LV), and liver from *Tax1bp3*^{+/+} and *Tax1bp3*^{-/-} mice of Tax1bp3 protein expression at 13.5kDa and reblotted Gapdh at 37kDA as the loading control.

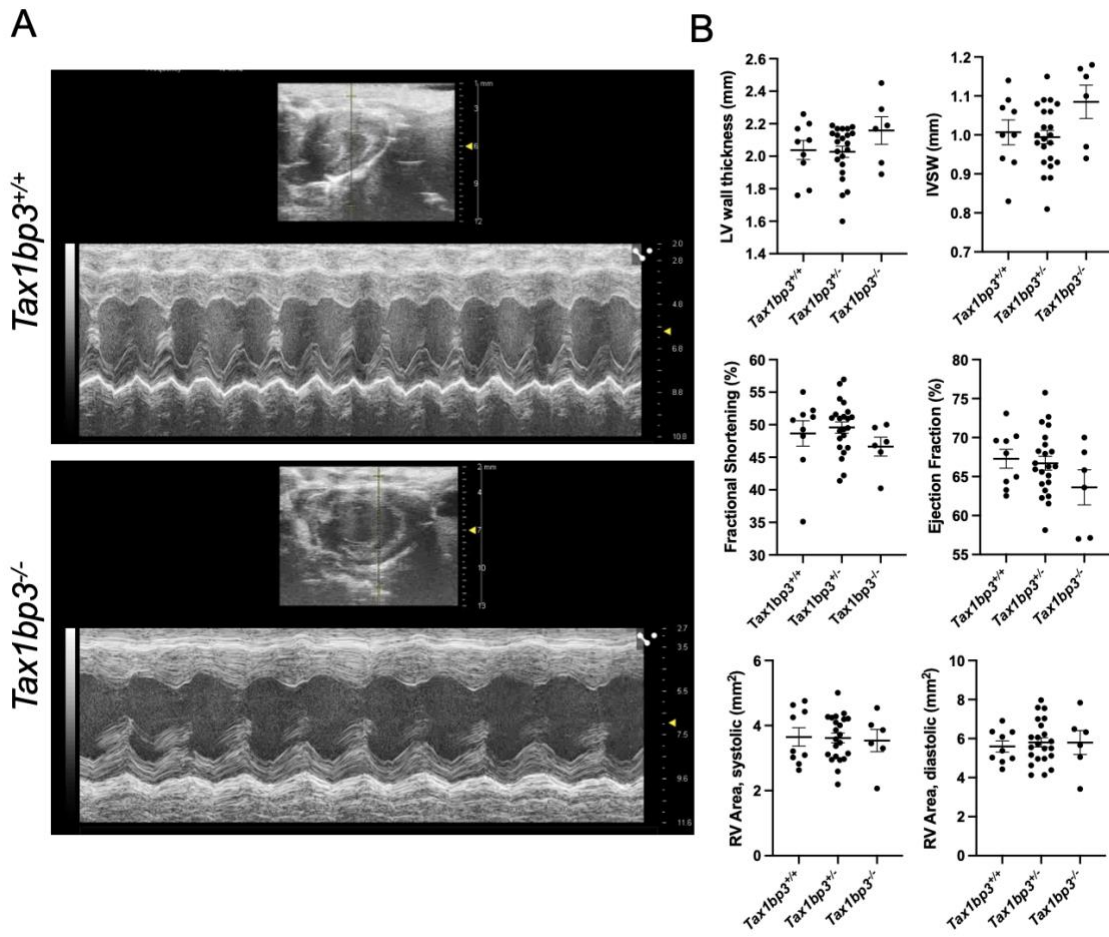


Figure 22: *Tax1bp3*^{-/-} mouse transthoracic echocardiograms demonstrate no differences compared to controls

A) Example long axis M-mode echocardiograms from *Tax1bp3*^{+/+} and *Tax1bp3*^{-/-} mice, respectively. B) Graphs with quantification of echocardiogram measurements of the left ventricular (LV) wall thickness, interventricular septum width (IVSW), fractional shortening, ejection fraction, systolic right ventricle (RV) area, and diastolic RV area (mean ± s.e.m., n= 9; 22; 6, not significant).

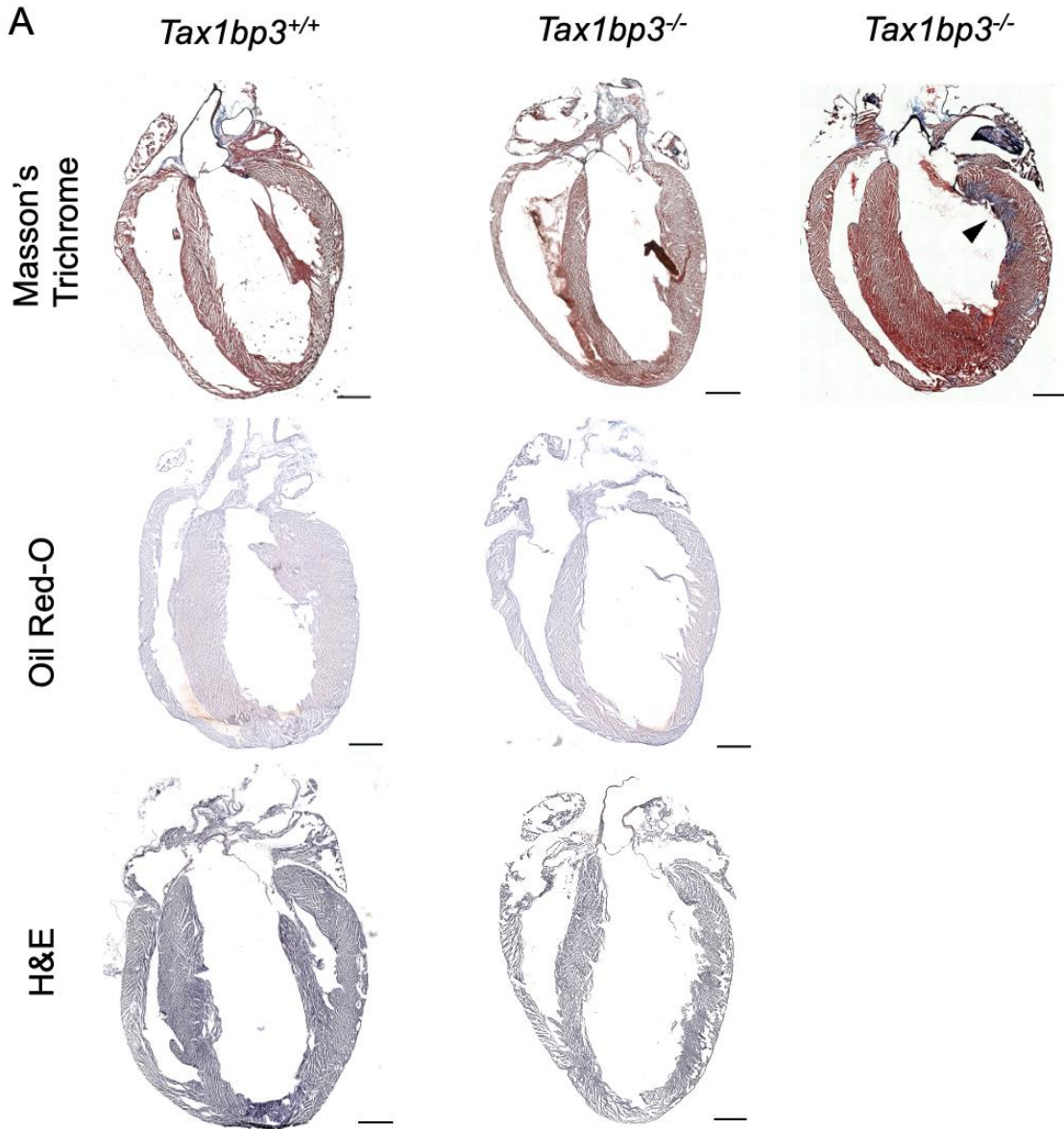


Figure 23: *Tax1bp3*^{-/-} mouse histology demonstrates no significant differences compared to controls.

A) Example tile scan images of histological sections from *Tax1bp3*^{+/+} and *Tax1bp3*^{-/-} mice, respectively, with Masson's Trichrome, Oil-red O, and H&E staining. Top right: While otherwise normal, 1 of the 6 *Tax1bp3*^{-/-} mice demonstrated large areas of fibrosis in the LV free wall (black arrow). Scale bars = 1000 μ m.

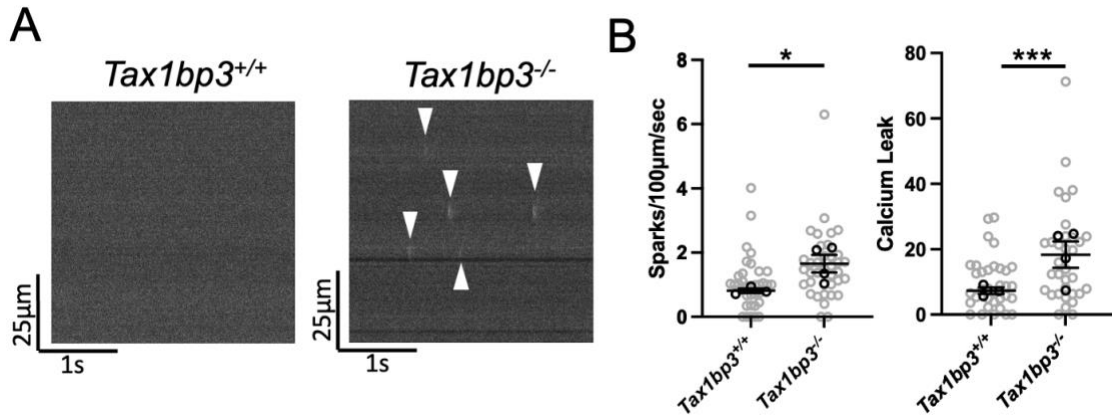


Figure 24: *Tax1bp3^{-/-}* have increased Ca^{2+} leak

A) Representative ROI images showing Ca^{2+} sparks from confocal line scans in *Tax1bp3^{+/+}* and *Tax1bp3^{-/-}* mice. White arrows denote examples of sparks. **B**) Quantification of spark frequency after 0.5Hz pacing (mean \pm s.e.m, n mice = 3; 4, n cells = 35; 37, $p = 0.00114$) and Ca^{2+} leak (mean \pm s.e.m, n mice = 3; 4, n cells = 34; 34, $p = 0.0006$). * $p < 0.05$, ** $p < 0.01$, *** $p < 0.001$.

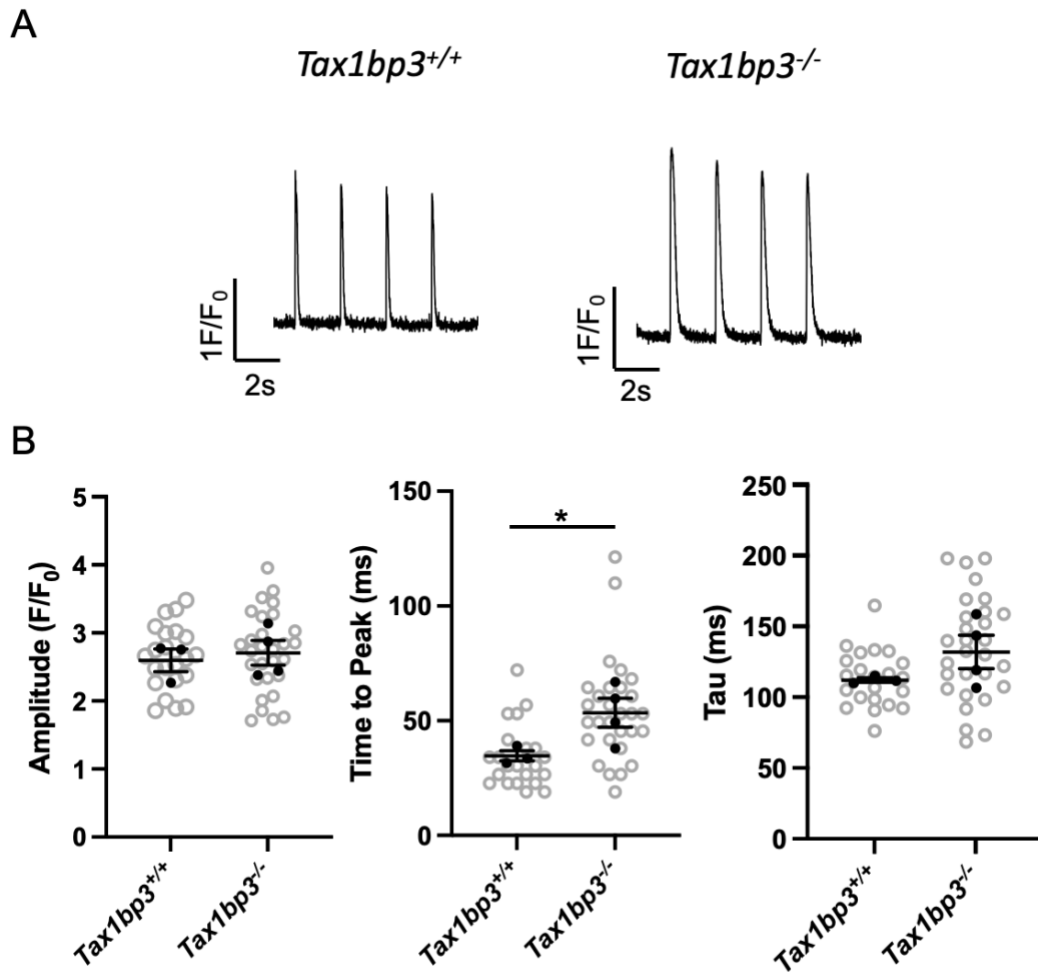


Figure 25: Ca²⁺ transient analysis in *Tax1bp3^{-/-}* mice shows increased time to peak

A). Representative example calcium transient traces during 0.5Hz pacing in *Tax1bp3^{+/+}* and *Tax1bp3^{-/-}* mice. B) Calcium transient quantifications for amplitude (mean \pm s.e.m, n mice = 3; 4, n cells = 22; 29, not significant), time to peak (mean \pm s.e.m, n mice = 3; 4, n cells = 22; 29, p = 0.0258, and Tau (mean \pm s.e.m, n mice = 3; 4, n cells = 22; 29, not significant). * p < 0.05, ** p < 0.01, *** p < 0.001.

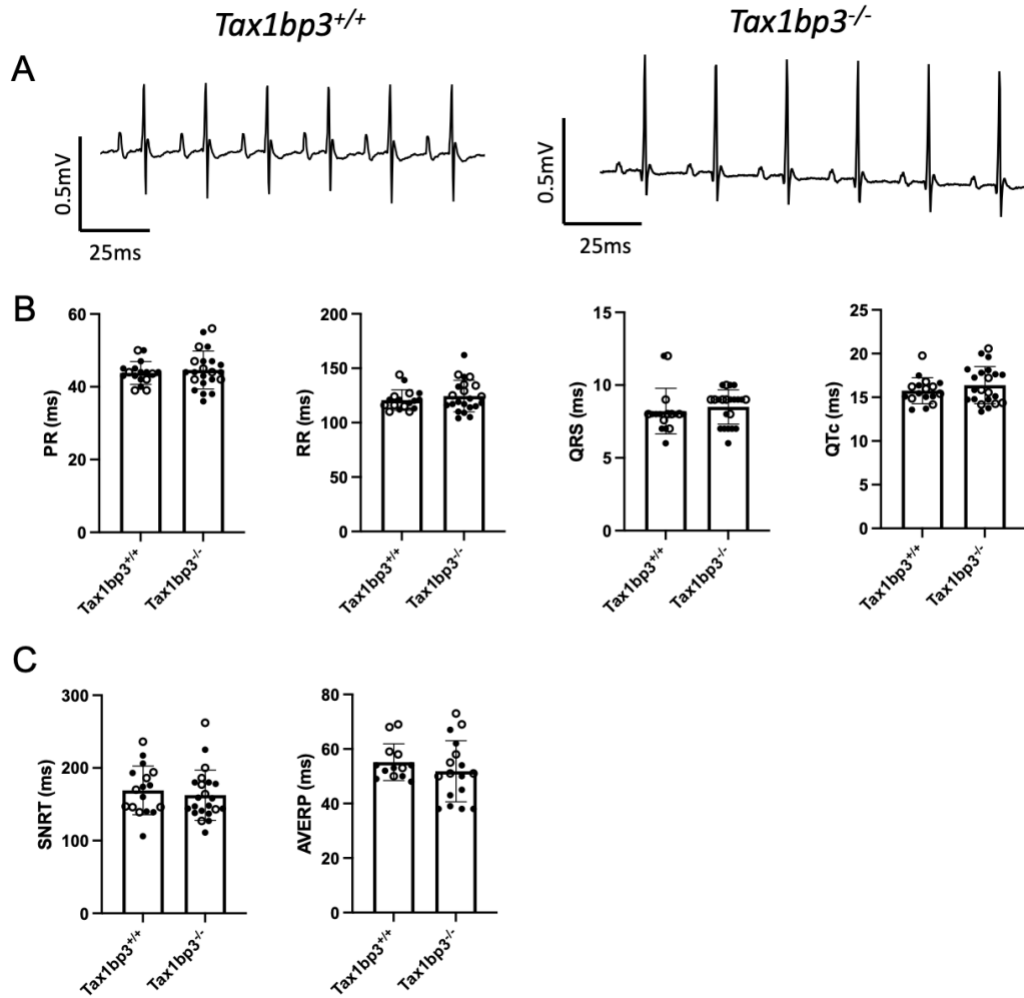


Figure 26: Electrocardiograms in *Tax1bp3^{-/-}* mice demonstrate no differences compared to controls

A) Example surface ECG traces in *Tax1bp3^{+/+}* and *Tax1bp3^{-/-}* mice, respectively. B) Graphs demonstrating the quantification of PR, RR, QRS and QTc intervals. Open circles are female mice and closed circles are male mice (mean \pm s.e.m., n = 17; 22, not significant). C) Quantification of sinus node recovery time (SNRT) (mean \pm s.e.m., n = 17; 22, not significant) and AV node effective refractory period (AVERP) (Mean \pm s.e.m., n = 11; 17, not significant). Open circles are female mice and closed circles are male mice.

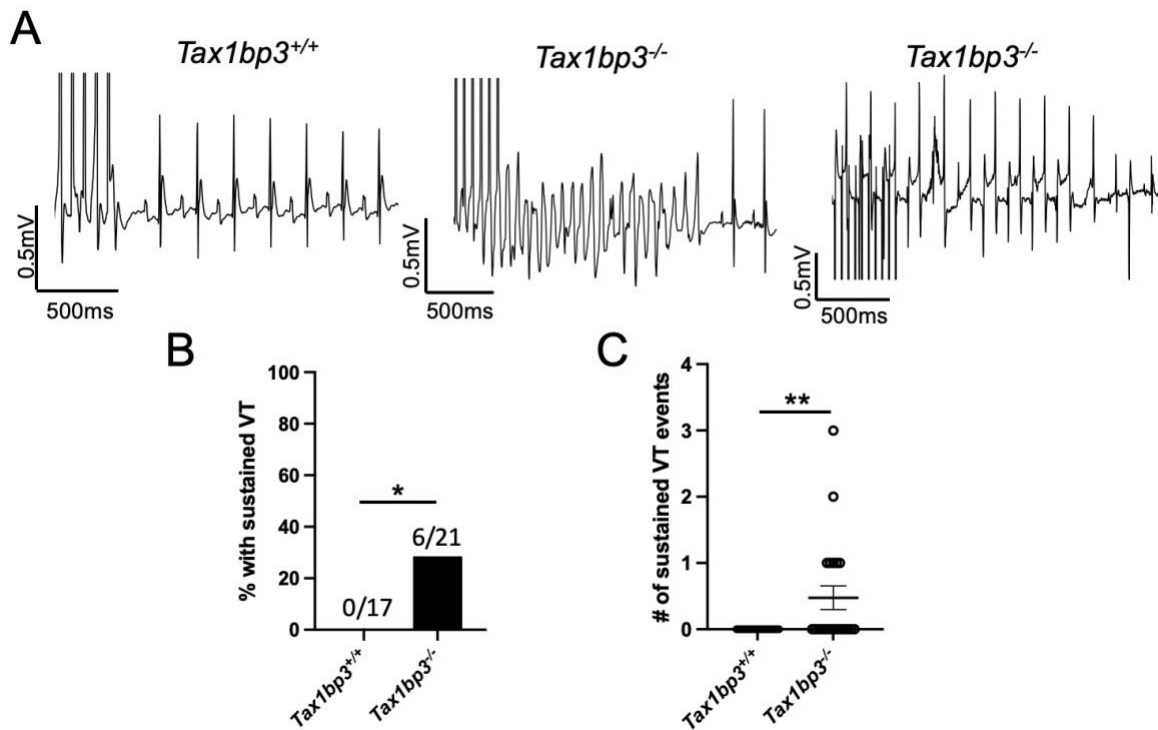


Figure 27: *Tax1bp3^{-/-}* mice have increased inducible ventricular tachycardia

A) Representative surface electrocardiogram (ECG) trace of sinus rhythm follow ventricular pacing in *Tax1bp3^{+/+}* mice and polymorphic and bidirectional ventricular tachycardia (VT) surface ECG traces in *Tax1bp3^{-/-}* mice. B) Quantification of percentage of mice with sustained VT (Mean \pm 95% confidence interval, n = 17; 21, p = 0.0148) C) Quantification of the number of sustained VT events per mouse (mean \pm s.e.m, n = 17; 21, p = 0.0096). * p < 0.05, ** p < 0.01, *** p < 0.001

6. TRPV4 current is activated in iPSC-CM^{M78T/del} and changes localization

6.1 TRPV4 current is activated in iPSC-CM^{M78T/del}

Given that the function of TAX1BP3 in the heart is unknown, we took a nonbiased approach to investigate the mechanism by which TAX1BP3 may be modulating intracellular Ca²⁺ leak. We performed bulk differential expression RNA-sequencing on iPSC-CMs from the two iPSC-CM^{M78T/del} lines and the iPSC-CM^{WT/WT} line. Due to the known role of Wnt signaling in ACM and that TAX1BP3 has been shown to bind to β -catenin in other tissues, we first looked at canonical Wnt signaling transcripts (Kanamori, Sandy et al. 2003, Garcia-Gras, Lombardi et al. 2006, Basso, Bauce et al. 2012). There were no significant differences in canonical Wnt signaling mRNA expression between the iPSC-CM^{M78T/del} lines and the iPSC-CM^{WT/WT} line (**Table 3**). Following subsequent manual curation of the differentially expressed genes that were consistent between both affected lines, we identified *TRPV4* as being increased in iPSC-CM^{M78T/del} lines compared to iPSC-CM^{WT/WT} (**Figure 28A**). TRPV4 is a nonselective cation channel permeable to Ca²⁺. This finding was of particular interest as increased TRPV4 current activity has been linked with increased Ca²⁺ spark frequency in cerebral arteries (Earley, Heppner et al. 2005) and aged mouse ventricular myocytes (Jones, Peana et al. 2019), and antagonism of TRPV4 suppressed atrial fibrillation in rats (Liao, Wu et al. 2020) which has been linked with SR Ca²⁺ leak (Voigt, Li et al. 2012). To test for TRPV4 functionally, we performed whole cell patch clamp. We found that iPSC-CM^{WT/WT} had minimal TRPV4 current (I_{TRPV4}) at basal conditions as well as following application of GSK1016790A, a potent and specific TRPV4 agonist. Conversely, iPSC-CM^{M78T/del} demonstrated a large increase in I_{TRPV4} following application of GSK1016790A (**Figure 26B-E**). Taken together with our previous findings, this suggests that *TAX1BP3* loss results in induction of functionally active TRPV4 expression.

Table 3: Canonical Wnt signaling mRNA expression in iPSC-CM RNA-sequencing

II.2 vs WT/WT			II.4 vs WT/WT		
Gene	Log Fold Change	Adjusted P-value	Gene	Log Fold Change	Adjusted P-value
<i>WNT5A</i>	0.055110207	0.62135769	<i>WNT5A</i>	0.024683721	0.73681491
<i>WNT7A</i>	0.098164605	0.53992445	<i>WNT7A</i>	-0.123046652	0.45545721
<i>DVL2</i>	0.061085266	0.56248546	<i>DVL2</i>	0.02081937	0.78801324
<i>DACT1</i>	-0.008758617	0.94803289	<i>DACT1</i>	-0.006520328	0.94268702
<i>AXIN2</i>	0.002656342	0.9876961	<i>AXIN2</i>	0.033628972	0.66552921
<i>TNKS2</i>	0.0079949	0.95514269	<i>TNKS2</i>	-0.007754221	0.93114924
<i>SFRP1</i>	0.028024086	0.83292975	<i>SFRP1</i>	-0.00312577	0.97705834
<i>LRP6</i>	0.001569847	0.99224179	<i>LRP6</i>	-0.006250623	0.94800766
<i>CSNK1G2</i>	0.057381146	0.60460501	<i>CSNK1G2</i>	0.008213574	0.92613427
<i>CBY1</i>	-0.011250722	0.93357418	<i>CBY1</i>	-0.005427813	0.95491416
<i>CTNNB1</i>	0.045937371	0.6865371	<i>CTNNB1</i>	0.005186453	0.95892185

6.2 TRPV4 localizes to the dyad in *Tax1bp3*^{-/-} mice

Given our findings in iPSC-CMs that I_{TRPV4} is induced with loss of TAX1BP3 expression, we hypothesized that this is due to re-localization of TRPV4 to the sarcolemma where I_{TRPV4} was detected. To test this, we performed immunofluorescence staining for TRPV4 which showed that the TRPV4 expression localization is primarily perinuclear and nuclear in control iPSC-CM^{WT/WT} (**Figure 29**). Conversely, in iPSC-CM^{M78T/del}, TRPV4 localized to the sarcolemma and co-localizes with desmoplakin (DSP), a cardiac desmosomal protein (**Figure 29**). Similar IF staining for Trpv4 in *Tax1bp3*^{-/-} ventricular myocytes revealed that Trpv4 was localized to the t-tubular sarcolemma in close proximity with RyR2. This was in stark contrast to Trpv4 staining in *Tax1bp3*^{+/+} mice,

which showed Trpv4-positive fluorescence in the nucleus and perinuclear area without clear colocalization with RyR2 (**Figure 30**). Overall, these findings suggest that TRPV4 changes subcellular localization from predominantly nuclear/perinuclear to the T-tubular sarcolemma in iPSC-CM^{M78T/del} and *Tax1bp3*^{-/-}, compared to respective controls.

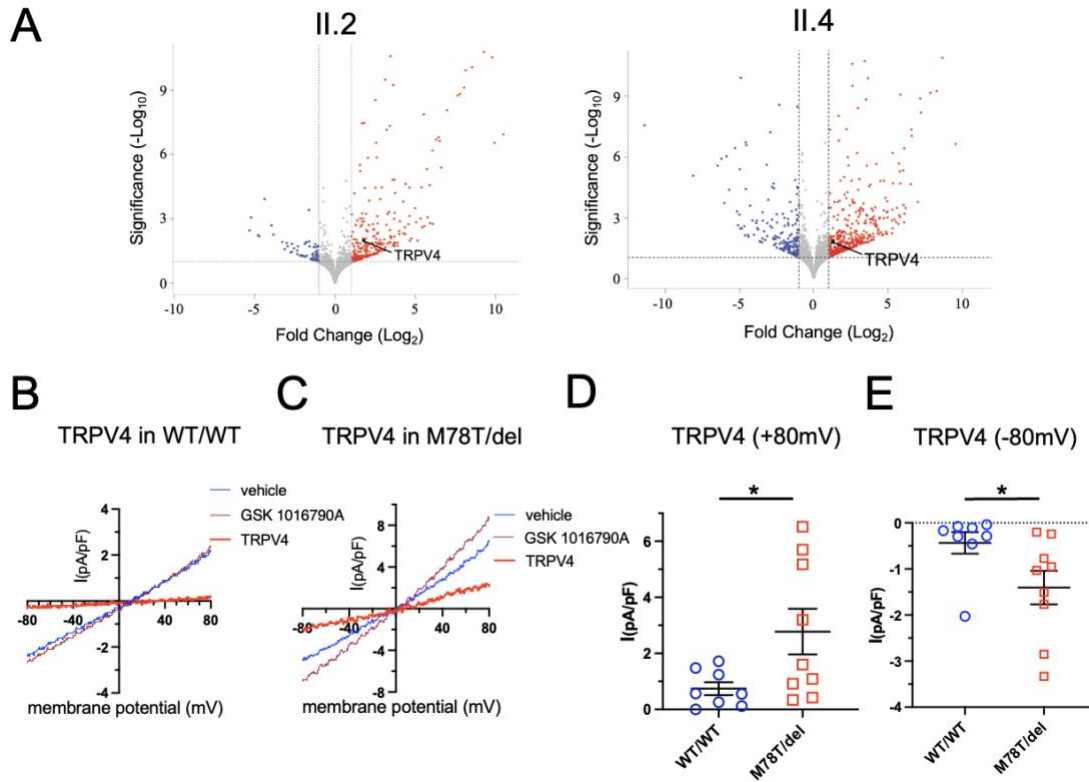


Figure 28: Increased TRPV4 activity in iPSC-CM^{M78T/del}

A) Volcano plots of RNA-sequencing of iPSC-CMs showing genes with an adjusted p value < 0.05 in II.2 vs WT (II.3, left) and II.4 vs. WT (right). B,C) Representative traces of I_{TRPV4} in iPSC-CM^{WT/WT} vs. iPSC-CM^{M78T/del} cells. I_{TRPV4} was calculated by subtracting the current after adding TRPV4 small molecule activator GSK1016790A from current with vehicle. D,E) Group mean values of I_{TRPV4} currents of iPSC-CM^{WT} vs. iPSC-CM^{M78T/del} cells measured at -80mV (mean ± s.e.m, n = 8; 9, p = 0.038) and +80mV (mean ± s.e.m, n = 8; 9, Unpaired T-test, p = 0.045). * p < 0.05, ** p < 0.01, *** p < 0.001. Volcano plot by Gabrielle Monaco and patch clamp by Zhushan Zhang.

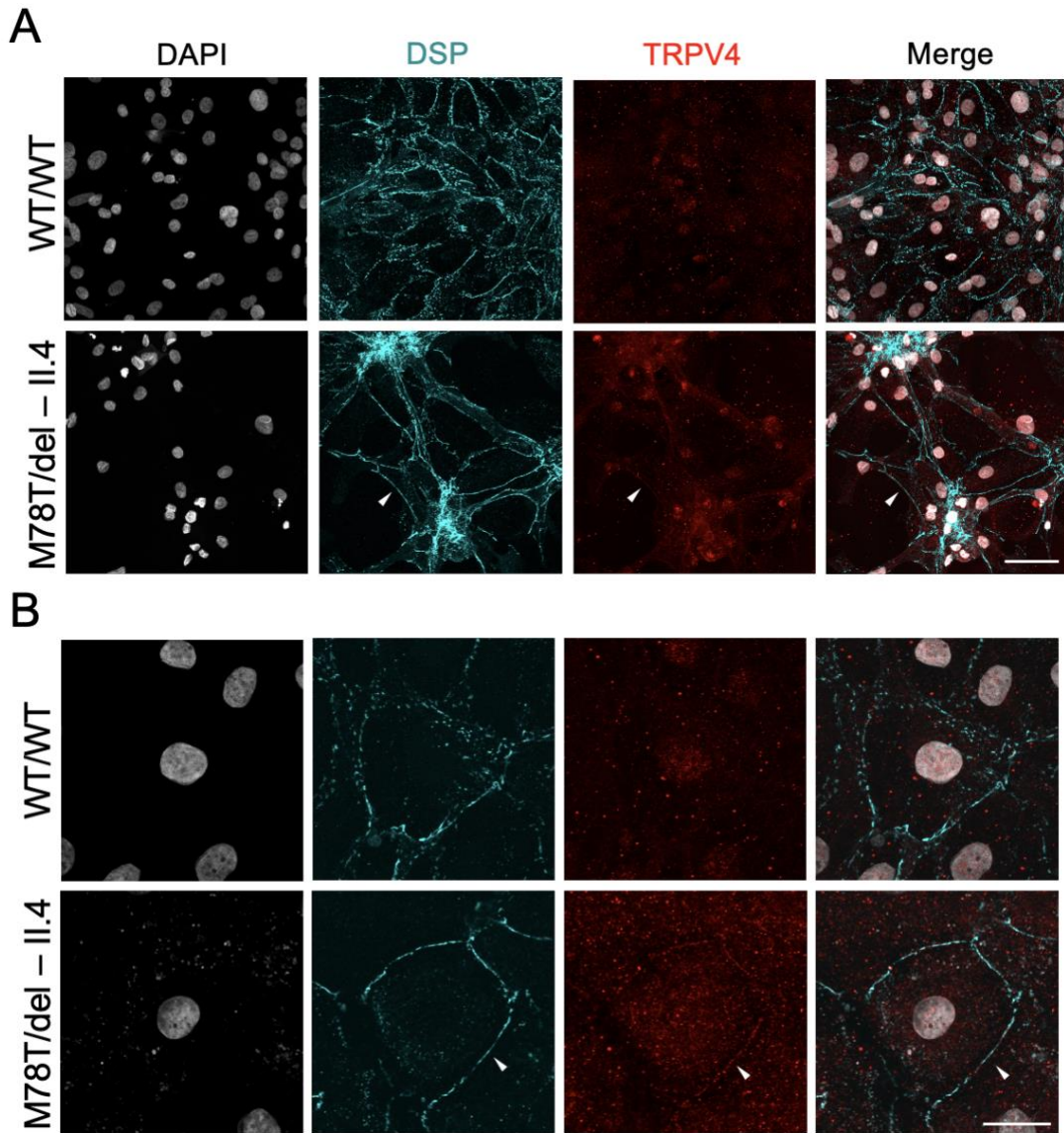


Figure 29: TRPV4 localization changes in iPSC-CM^{M78T/del}

A) Immunofluorescence of DAPI (white), DSP (cyan), and TRPV4 (red). White arrow denotes an example of overlap between DSP and TRPV4 signal in the iPSC-CM^{M78T/del} cells. Scale bar = 50 μ m.
 B) Higher magnification of staining in A with white arrows denoting TRPV4 and nucleus colocalization in iPSC-CM^{WT/WT} and DSP and TRPV4 signal overlap at the cell membrane in iPSC-CM^{M78T/del}. Scale bar = 20 μ m.

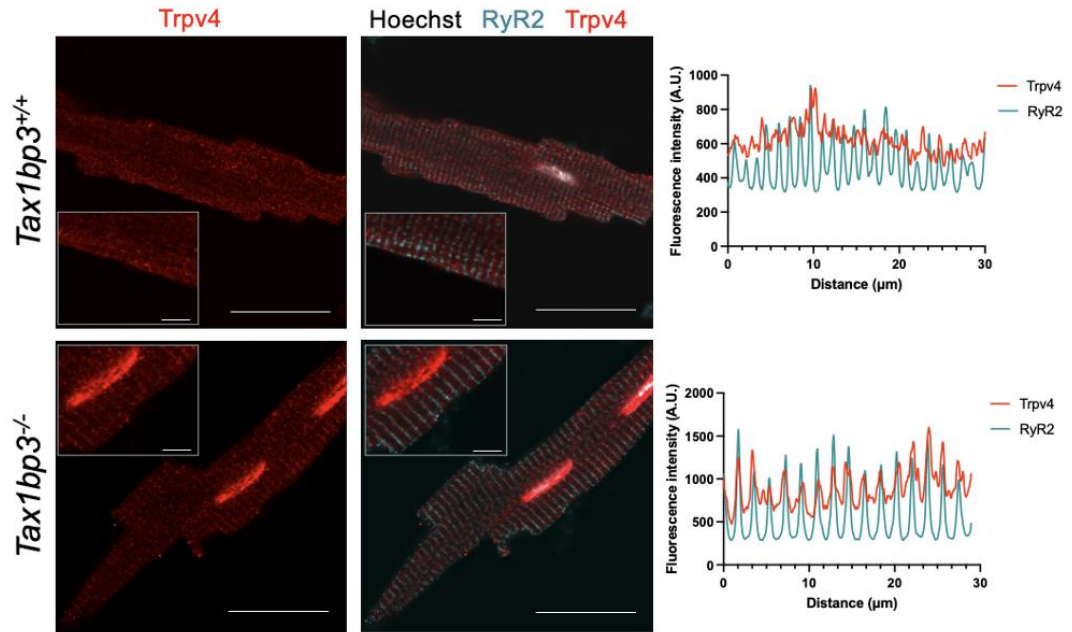


Figure 30: Trpv4 localization changes in *Tax1bp3*^{-/-} mice

Representative confocal images of immunofluorescence of Hoechst (white), RyR2 (cyan), and TRPV4 (red) on isolated mouse ventricular myocytes with corresponding fluorescence plot profiles (n mice = 4 *Tax1bp3*^{+/+}, n mice = 3 *Tax1bp3*^{-/-}). Scale bars = 25µm, inset scale bars = 5µm.

7. Small molecule TRPV4 inhibition rescues Ca²⁺ leak in vitro and in vivo

7.2 Ca²⁺ leak and delayed afterdepolarizations can be suppressed by TRPV4 inhibition

We next hypothesized that TRPV4 inhibition would rescue the increased Ca²⁺ leak in iPSC-CM^{M78T/del} lines. To test this, we added a TRPV4-specific inhibitor small molecule HC-067047 to the iPSC-CMs and found a reduction of Ca²⁺ spark frequency and leak in the iPSC-CM^{M78T/del} cells. We used the iPSC-CM^{M78T/del-II.4} line because of the stronger Ca²⁺ leak phenotype. This reduction was equivalent to untreated iPSC-CM^{WT/WT} Ca²⁺ leak levels (**Figure 31A and B**). HC-067047 also reduced the spontaneous Ca²⁺ release events (**Figure 31C and D**). Furthermore, iPSC-CM^{M78T/del} cells exhibited an increased propensity for delayed-afterdepolarizations, a known cellular etiology for triggered arrhythmogenesis of the myocardium, which was also ameliorated by TRPV4 inhibition (**Figure 31 E-H**). These findings suggest that loss of *TAX1BP3* leads to increased Ca²⁺ leak, and this can be suppressed by TRPV4 antagonism.

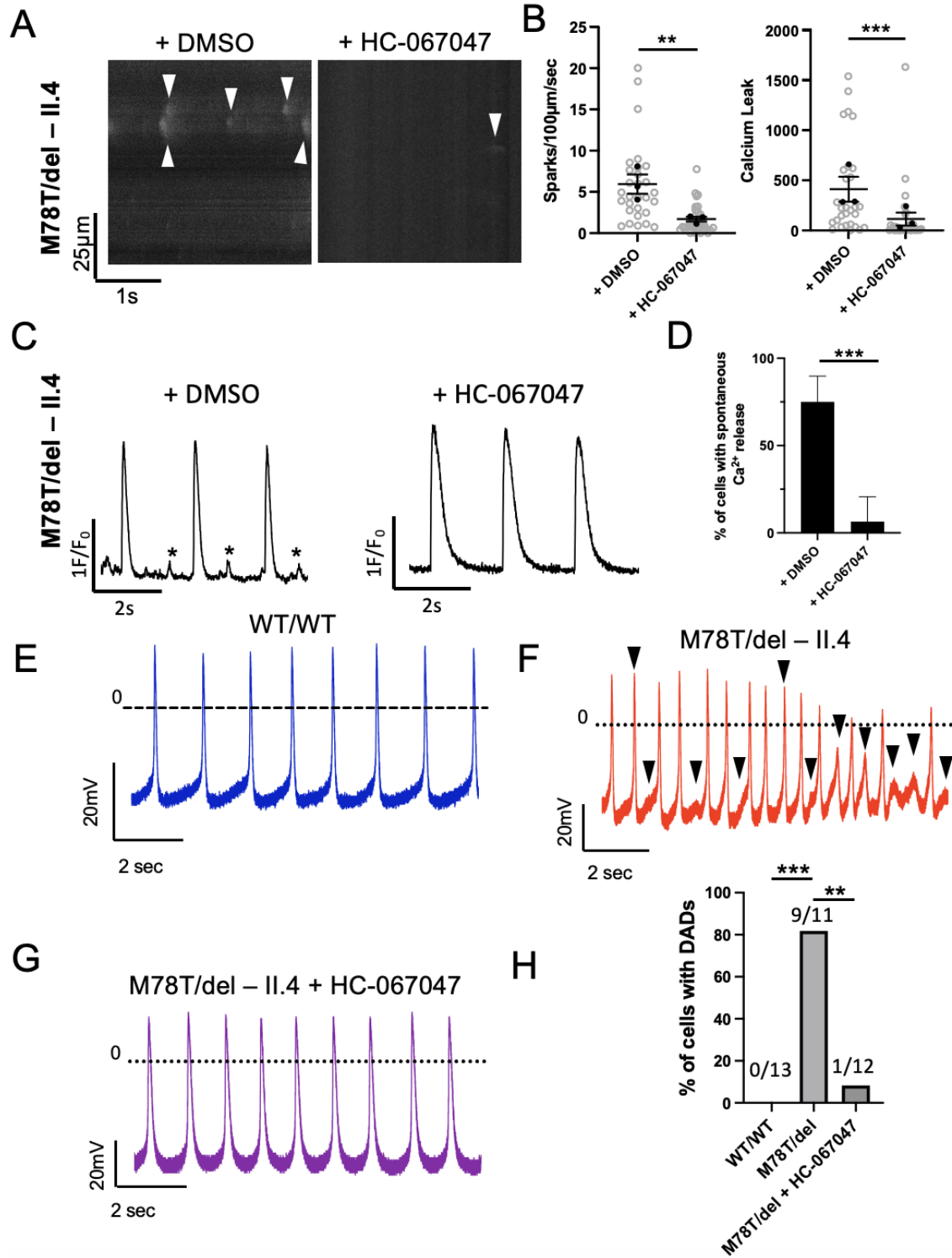


Figure 31: TRPV4 inhibition with HC-067047 rescues Ca²⁺ leak and DADs

A) Example confocal images of regions of interest for Ca²⁺ sparks in II.4 iPSC-CMs treated with DMSO or 1µM HC-067047. White arrows denote examples of sparks. B) Quantification of spark

frequency (mean \pm s.e.m, hierarchical test, M78T/del II.4: n differentiations = 3;3, n cells = 29; 31, $p = 0.0034$) and Ca^{2+} leak (mean \pm s.e.m, hierarchical test, M78T/del II.4: n differentiations = 3;3, n cells = 29; 31, $p < 0.0001$). C, D) Example traces of Ca^{2+} fluorescence in II.2 and II.4 iPSC-CMs following DMSO or $1\mu\text{M}$ HC-067047. Asterisks indicate spontaneous Ca^{2+} release. F,H) Quantification of the percentage of cells with spontaneous Ca^{2+} release. Error bars indicate 95% confidence interval, $p < 0.001$ E, F) Examples tracings of action potentials recordings from iPSC-CM^{WT/WT} and iPSC-CM^{M78T/del}, respectively. Black arrows denote delayed afterdepolarizations (DADs) G) iPSC-CM^{M78T/del-II.4} action potential example trace with $10\mu\text{M}$ HC-067047 pre-treatment. H) Bar graph demonstrating the quantification of the percentage of cells which demonstrated DADs (mean, n = 13; 11; 12, WT/WT vs. M78T/del, $P < 0.0001$; M78T/del vs. M78T/del + HC-067047, $P < 0.01$). * $p < 0.05$, ** $p < 0.01$, *** $p < 0.001$. Patch clamp by Zhushan Zhang.

7.3 TRPV4 inhibition rescues Ca^{2+} leak in $\text{Tax1bp3}^{-/-}$ mice

Given our observation that TRPV4 inhibition normalized Ca^{2+} -mediated DADs and SR store leak, we hypothesized that it would also reduce aberrant Ca^{2+} leak and spontaneous Ca^{2+} release events (SREs) in $\text{Tax1bp3}^{-/-}$ myocytes. To test this, we applied HC-067047 to isolated primary ventricular myocytes derived from $\text{Tax1bp3}^{-/-}$ mice. We found that application of HC-067047 normalized the elevated Ca^{2+} leak in the isolated ventricular myocytes from $\text{Tax1bp3}^{-/-}$ mice to approximately WT levels (**Figure 32A and B**). Furthermore, we observed a marked reduction in SREs from $\text{Tax1bp3}^{-/-}$ ventricular myocytes, again to WT levels (**Figure 32C and D**). Overall, these findings suggesting that TRPV4 inhibition decreases the aberrant Ca^{2+} leak and SREs which is the cellular substrate for triggered ventricular arrhythmias in these mice.

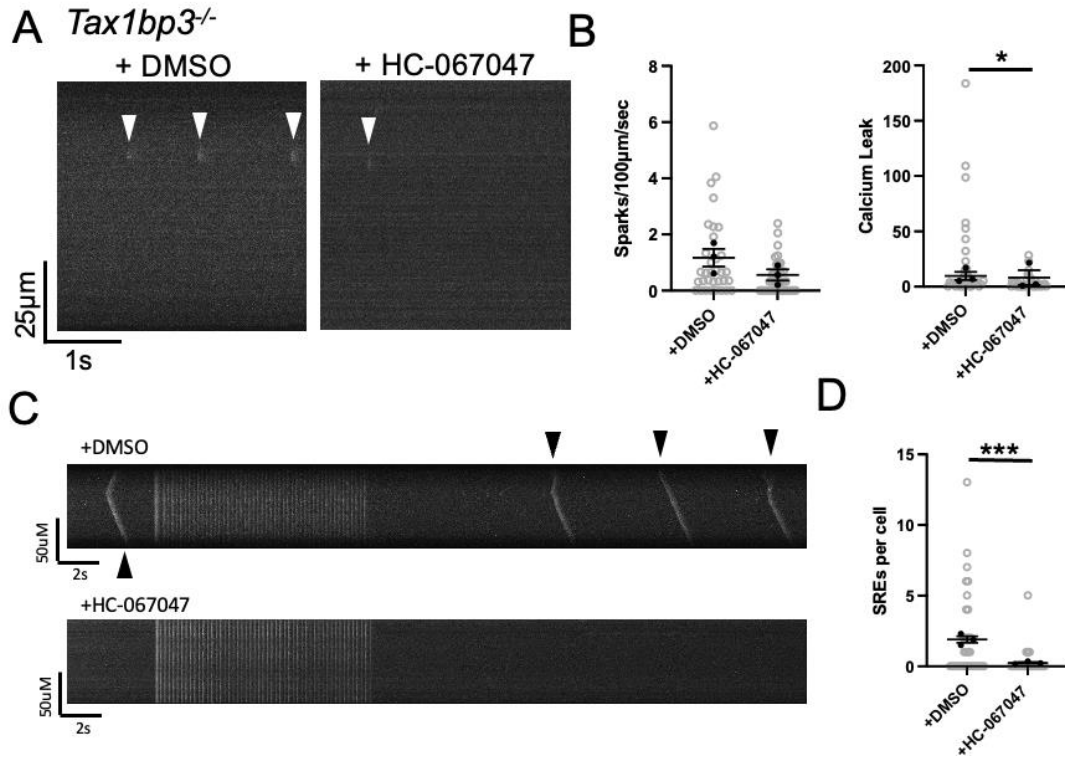


Figure 32: TRPV4 inhibition rescues Ca²⁺ leak in *Tax1bp3*^{-/-} mice

A). Representative line scans from live cell Ca²⁺ confocal imaging after 0.5Hz pacing from *Tax1bp3*^{-/-} mice with either DMSO or 1µM HC-067047 (white arrows denote Ca²⁺ sparks). B) Graph of the quantification of Ca²⁺spark frequency (mean ± s.e.m, n mice = 3; 3, n cells = 33; 35, not significant) and Ca²⁺ leak (mean ± s.e.m, n mice = 3; 3, n cells = 33; 35, p < 0.05). C) Representative confocal line scans with 5Hz pacing with either DMSO or 1µM HC-067047 (black arrows denote spontaneous release events (SREs)). D) Graph quantifying the number of SREs per ventricular cell (mean ± s.e.m, n mice = 3; 3, n cells = 35; 35, p < 0.001). * p < 0.05, ** p < 0.01, *** p < 0.001.

8. TRPV4 inhibition reduces Ca²⁺ leak in iPSC-CMs derived from a PKP2-positive ACM donor

To explore if TRPV4-mediated Ca²⁺ leak could be an underlying phenomenon in other patients with ACM, we moved to an iPSC-CM model derived from an ACM patient with a heterozygous PKP2-His773AlafsX8 (c.2197_2202delCACACCinsG) variant in *PKP2* (iPSC-CM^{PKP2-fs}) and validated that the line expressed iPSC and CM markers with IF (**Figure 33**). The donor has early onset ventricular tachycardia requiring ICD placement. The donor for the PKP2-fs iPSC line is a male who was diagnosed with ACM at 35 years of age following onset of VT. Genetic testing demonstrated a heterozygous variant in PKP2-His773AlafsX8 (c.2197_2202delCACACCinsG) which was assessed as likely pathogenic by ACMG criteria (Richards, Aziz et al. 2015). Cardiac MRI demonstrated a severely dilated RV with moderately reduced RV function (RVEF ~37%) with evidence of fatty replacement of the inferior portion of the RV free wall and diaphragmatic wall as well as evidence of fat involvement of the interventricular septum at the basal septum. He met 2010 modified Taskforce Criteria (Marcus, McKenna et al. 2010) and the 2019 Heart Rhythm consensus guidelines for ACM (Towbin, McKenna et al. 2019). He is status post ICD placement with recurrent ventricular arrhythmias. The PKP2-WT line derives from an unrelated, ostensibly healthy 41-year-old Caucasian male.

The loss-of-function variant in *PKP2* represents the most observed genetic subtype of ACM and is diagnostic by current ACMG criteria (Marcus, McKenna et al. 2010). Importantly, ACM-associated variants in *PKP2* have been previously linked with Ca²⁺ leak from Ryr2 (Cerrone, Montnach et al. 2017).

To determine whether these cardiac myocytes demonstrated increased Ca²⁺ leak, we first conducted live cell Ca²⁺ imaging and found that iPSC-CM^{PKP2-fs} had greater Ca²⁺ leak from the SR, driven largely by increased spark frequency, when compared to a sex-matched, healthy control

iPSC-CM line (iPSC-CM^{PKP2-WT}). Strikingly, exposure of these cells to HC-067047, and resultant TRPV4 inhibition suppressed this leak and normalized it to that of WT control levels (**Figure 34**). When combined with our previous findings, these results suggest that loss of *TAX1BP3* results in increased TRPV4 expression and translocation to the t-tubules, increased I_{TRPV4} , and increased store Ca^{2+} leak which allows for DAD-mediated ventricular arrhythmias (**Figure 35**). Finally, given the ability of TRPV4 inhibition to suppress Ca^{2+} leak in both the iPSC-CM^{M78T/del} and *Tax1bp3*^{-/-} mouse model, as well as a separate ACM iPSC-CM patient cell line derived from a donor with PKP2-mediated disease, this strategy could be a novel therapeutic target for treating arrhythmias associated with ACM more broadly.

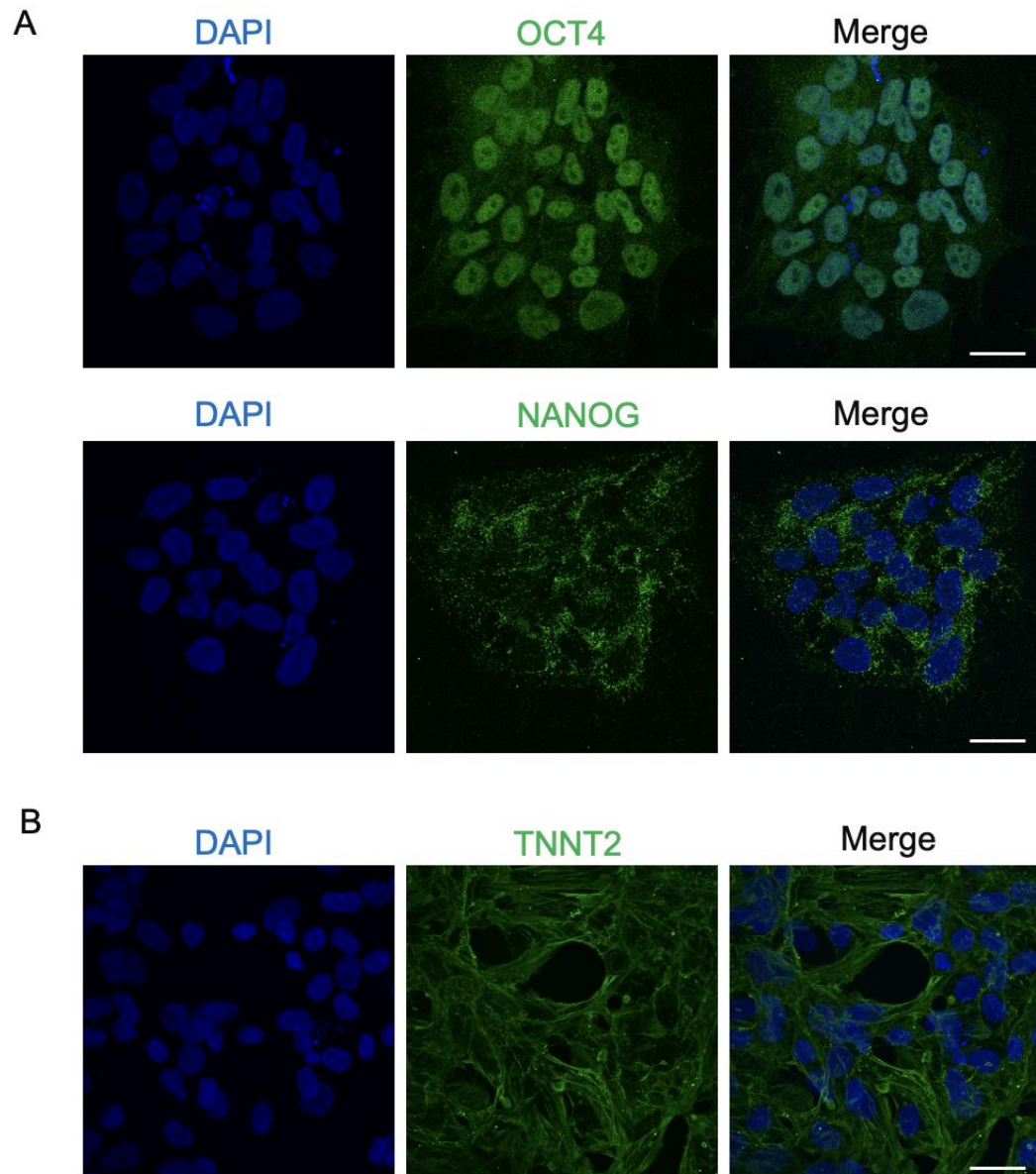


Figure 33: Figure 34: PKP2-fs iPSC and iPSC-CM validation

A) Immunofluorescence of iPSC markers OCT4 or NANOG and DAPI on the iPSC-CM^{PKP2-fs}. Scale bars =25µm B) Immunofluorescence of cardiomyocyte marker TNNT2 and DAPI on iPSC-CM^{PKP2-fs}, scale bar = 25µm.

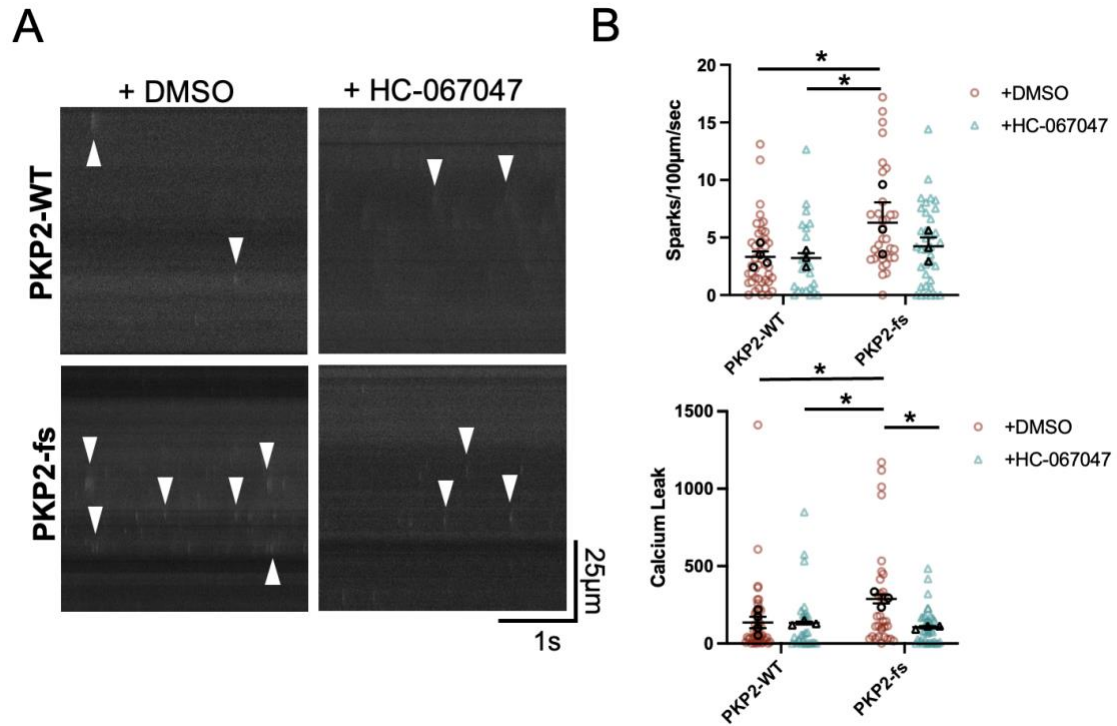


Figure 34: TRPV4 inhibition rescues Ca²⁺ leak in PKP2-fs iPSC-CMs

A) Representative images from live cell, Ca²⁺ imaging confocal line scans after 0.5Hz pacing from iPSC-CM^{PKP2-fs} and iPSC-CM^{PKP2-WT} after either DMSO (red circles) or 1µM HC-067047 (cyan triangles) exposure. B) Quantification of Ca²⁺ spark frequency (mean ± s.e.m, n differentiations = 3; 3; 3; 3, n cells = 34; 26; 32; 37, iPSC-CM^{PKP2-WT} +DMSO vs iPSC-CM^{PKP2-fs} + HC-067047, p = 0.0221) and Ca²⁺ leak (mean ± s.e.m, n differentiations = 3; 3; 3; 3, n cells = 34; 26; 32; 37, iPSC-CM^{PKP2-WT} + DMSO vs iPSC-CM^{PKP2-WT} + HC-067047, not significant, iPSC-CM^{PKP2-WT} + DMSO vs iPSC-CM^{PKP2-fs} + DMSO, p = 0.0365, iPSC-CM^{PKP2-WT} + HC-067047 vs iPSC-CM^{PKP2-fs} + DMSO, p = 0.0131, iPSC-CM^{PKP2-fs} +DMSO vs iPSC-CM^{PKP2-fs} + HC-067047, p = 0.0174.* p < 0.05, ** p < 0.01, *** p < 0.001.

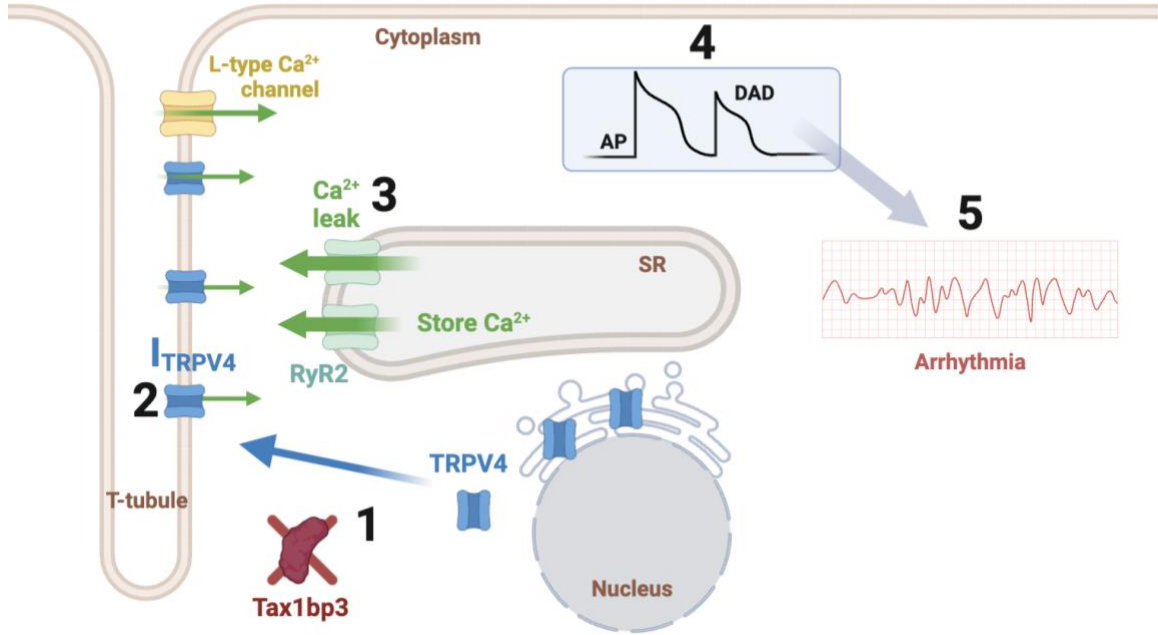


Figure 35: Proposed mechanism of TAX1BP3-mediated arrhythmia development

1) Loss of Tax1bp3 results in Trpv4 translocation to the t-tubules. 2) This leads towards development of I_{TRPV4} . 3) The increased Ca^{2+} triggers Ca^{2+} leak from the sarcoplasmic reticulum (SR) via RyR2 that 4) drives development of delayed after depolarizations (DADs). 5) This leads to triggered arrhythmogenesis of the myocardium.

9. Development of a novel arrhythmogenic exercise mouse model

Exercise accelerates disease progression in ACM and also increases risk for sudden cardiac death (Corrado, Basso et al. 2003, James, Bhonsale et al. 2013, Saberniak, Hasselberg et al. 2014, Ruwald, Marcus et al. 2015, Finocchiaro, Papadakis et al. 2016, Lie Ø, Dejgaard et al. 2018, Lüsebrink, Binzenhöfer et al. 2021, Bosman, Wang et al. 2022, Binzenhöfer, Clauss et al. 2024). It has also been proposed that exercise itself can cause AC, in addition to being a risk factor for the generation of arrhythmias (Prior and La Gerche 2020). Because of this, management of ACM includes exercise restriction, which is challenging to implement, detrimental to quality of life, and increases risks for other diseases, so there is a critical need to understand the impacts of exercise on ACM pathogenesis. Further, among pediatric patients, there's often an arrhythmic burden that precedes remodeling - but there are currently no models of this.

Because exercise is a known risk factor in ACM, we hypothesized that exercising the mice would increase arrhythmia predisposition and induce cardiac remodeling. To test this, after baseline echocardiograms and an initial swimming training period, we swam the mice for 90 minutes daily for 6 weeks and then performed repeat echocardiograms, intracardiac electrophysiology studies, and collected the hearts for histology (**Figure 36 and Table 4**).

During swimming, mice were removed from the pool when they could no longer keep their heads above water. The *Tax1bp3^{-/-}* mice had a higher number of instances when they had to be pulled out of the pool because and also had a greater amount of swimming time missed compared to the control mice due to often needing to be rescued early during the exercise (**Figure 37**). Interestingly, this was likely not due to heart failure as there were still no differences in echocardiograms or histology in the mice after swimming (**Figure 38**). Two animals died during the swimming: one homozygous and one heterozygous. Because we did not have telemetry on the

mice, we cannot be sure that the deaths were due to arrhythmias, although it seems likely given the lack of remodeling found in the surviving mice. There were no differences in surface ECGs after swimming (**Figure 39**), but as hypothesized, the percentage of *Tax1bp3*^{-/-} mice with induced ventricular arrhythmias during the EP studies increased to 50% compared to 30% without exercise (**Figure 40**).

To conclude, we found that loss of *Tax1bp3* in mice leads to greater ventricular arrhythmia predisposition compared with controls, which is increased following swimming exercise. There is another exercise model of ACM using Plakophilin conditional knockout mice, but in that model the mice also have cardiac remodeling. This provides an opportunity to use this model to study the impact of exercise on arrhythmia predisposition, independent of structural changes to the heart.



Figure 36: *Tax1bp3*^{-/-} exercise study design

Graphic of the swimming study design for *Tax1bp3*^{-/-} and *Tax1bp3*^{+/+} mice. The mice were given baseline echocardiograms before having a block of swimming 90 minutes per day (excluding weekend days) for 6 weeks total. After the 6 week block, the mice were given repeat echocardiograms followed by intracardiac electrophysiology studies. Hearts were collected and used for downstream histology. Figure and study design by Andrew Breglio.

Table 4: Mouse swimming schedule
Maximum swimming time in minutes per sessions.

	Monday	Tuesday	Wednesday	Thursday	Friday
Week 1	5	10	15	20	25
Week 2	30	35	40	45	50
Week 3	55	60	65	70	75
Week 4	80	85	90	90	90
Week 5	90	90	90	90	90
Week 6	90	90	90	90	90

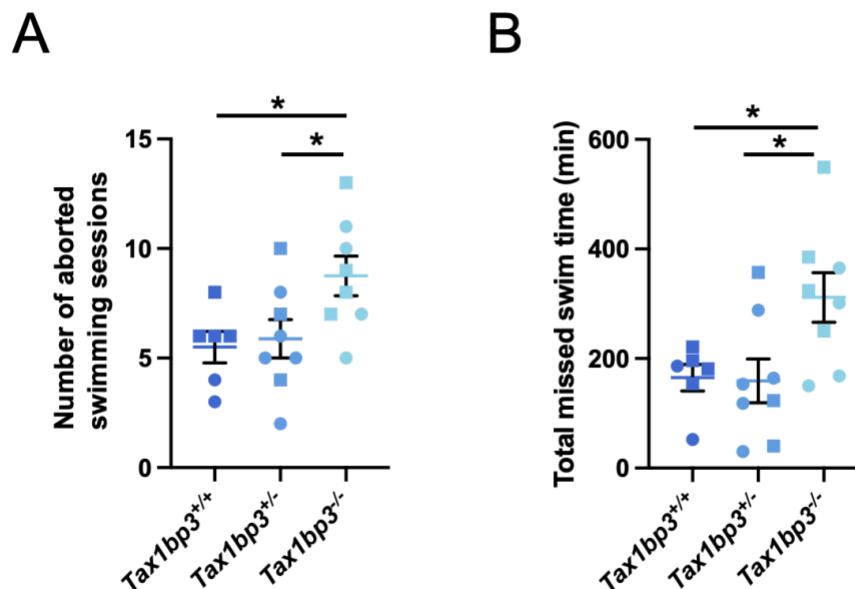


Figure 37: Swimming exercise tolerance is decreased in *Tax1bp3*^{-/-} mice

A) Quantification of the number of times a mouse was removed from swimming before the swimming time period was over (mean \pm s.e.m, n mice = 6; 8; 8, *Tax1bp3*^{+/+} vs. *Tax1bp3*^{-/-}: p = 0.0363, *Tax1bp3*^{+/-} vs. *Tax1bp3*^{-/-}: p = 0.0265). B) Quantification of the total number of minutes of swim time that was missed from the total amount planned (mean \pm s.e.m, n mice = 6; 8; 8, *Tax1bp3*^{+/+} vs. *Tax1bp3*^{-/-}: p = 0.0215, *Tax1bp3*^{+/-} vs. *Tax1bp3*^{-/-}: p = 0.0111).

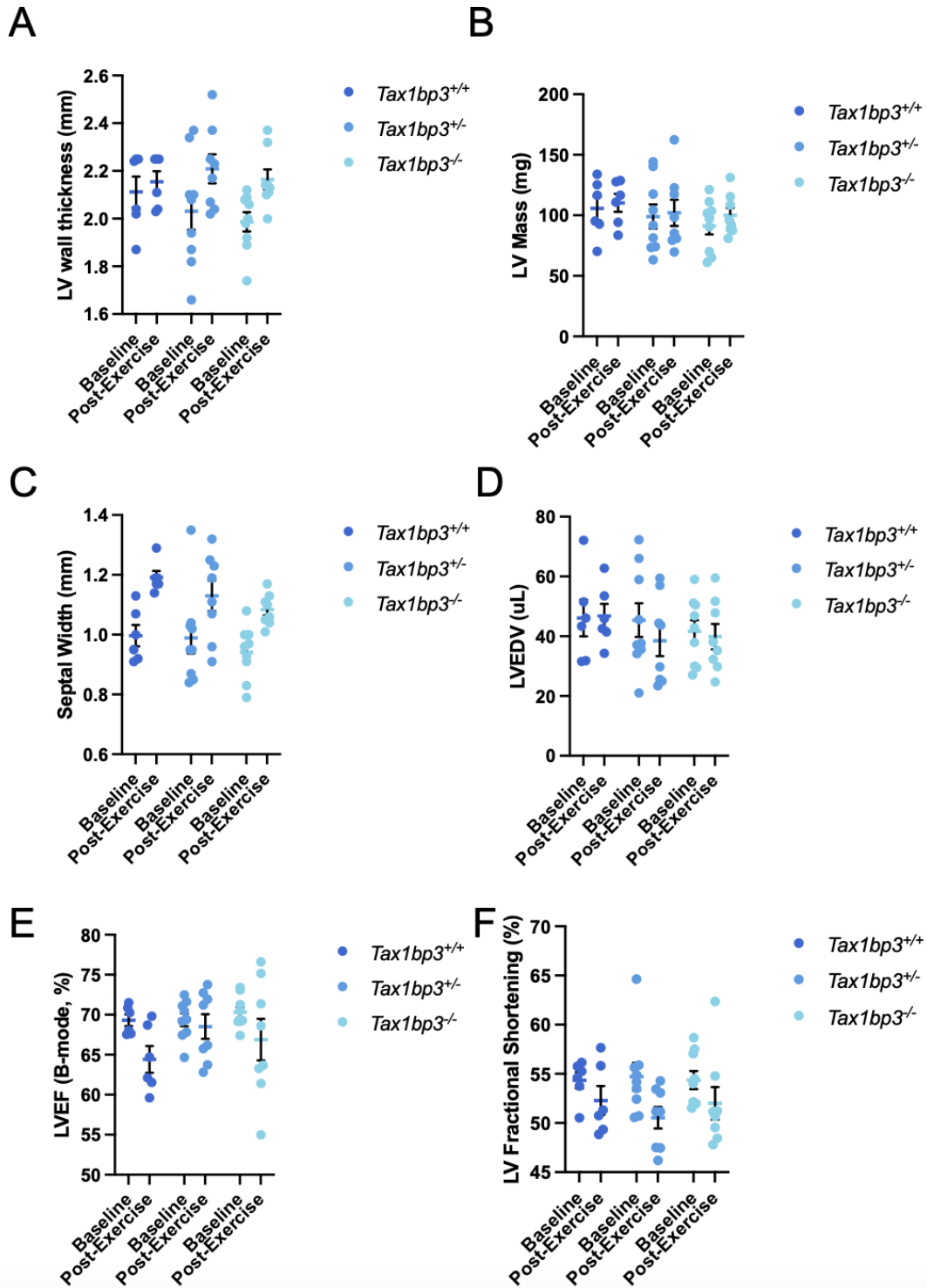


Figure 38: Transthoracic echocardiograms before and after swimming

A-D) Quantification of echocardiograms from *Tax1bp3*^{+/+}, *Tax1bp3*^{+/-}, and *Tax1bp3*^{-/-} mice before and after swimming of left ventricle (LV) anatomy: LV wall thickness, LV mass, septal width, and

LV end diastolic volume (LVEDV) E,F) Quantification of echocardiograms from *Tax1bp3*^{+/+} and *Tax1bp3*^{-/-} mice before and after swimming of left ventricle systolic function: LV ejection fraction (LVEF) and LV fractional shortening (mean ± s.e.m. n mice before exercise = 6; 9; 9, n mice after exercise = 6; 8; 8, not significant).

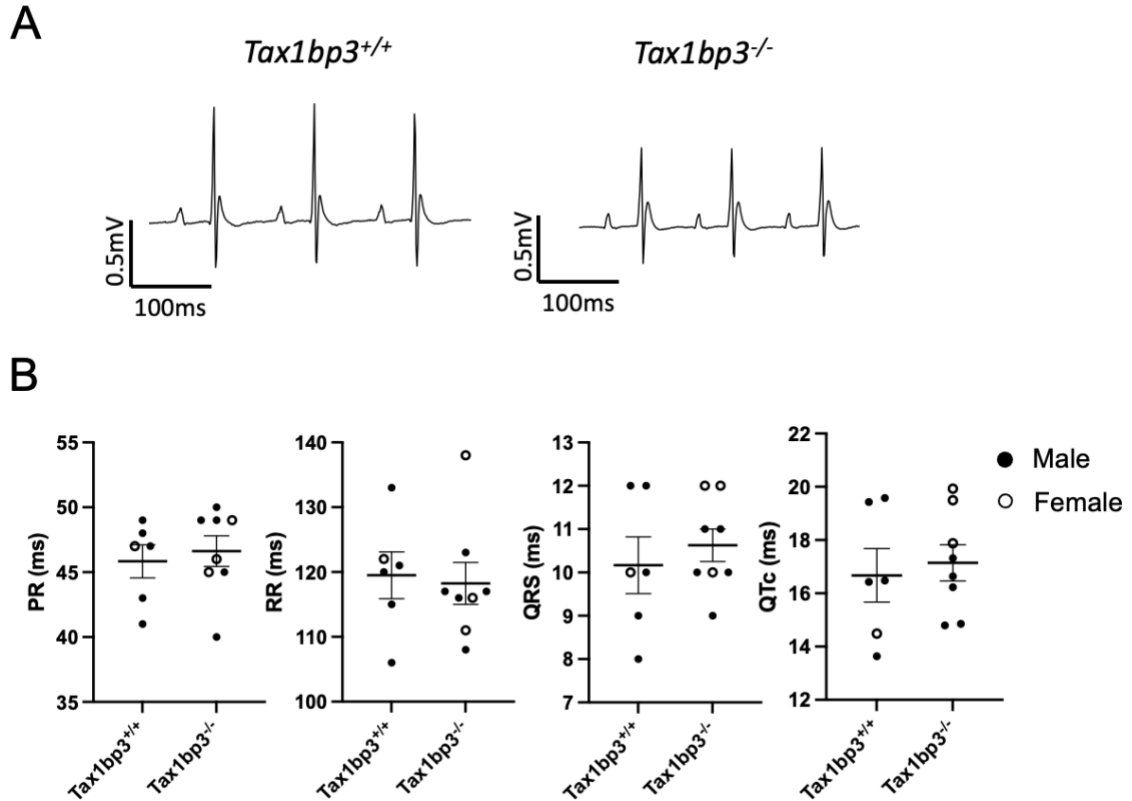


Figure 39: Surface ECGs after swimming

A) Example representative surface ECG traces of *Tax1bp3*^{+/+} and *Tax1bp3*^{-/-} mice after swimming exercise. B) Quantifications of PR, RR, QRS, and QTc intervals (mean ± s.e.m. n mice = 6, 8).

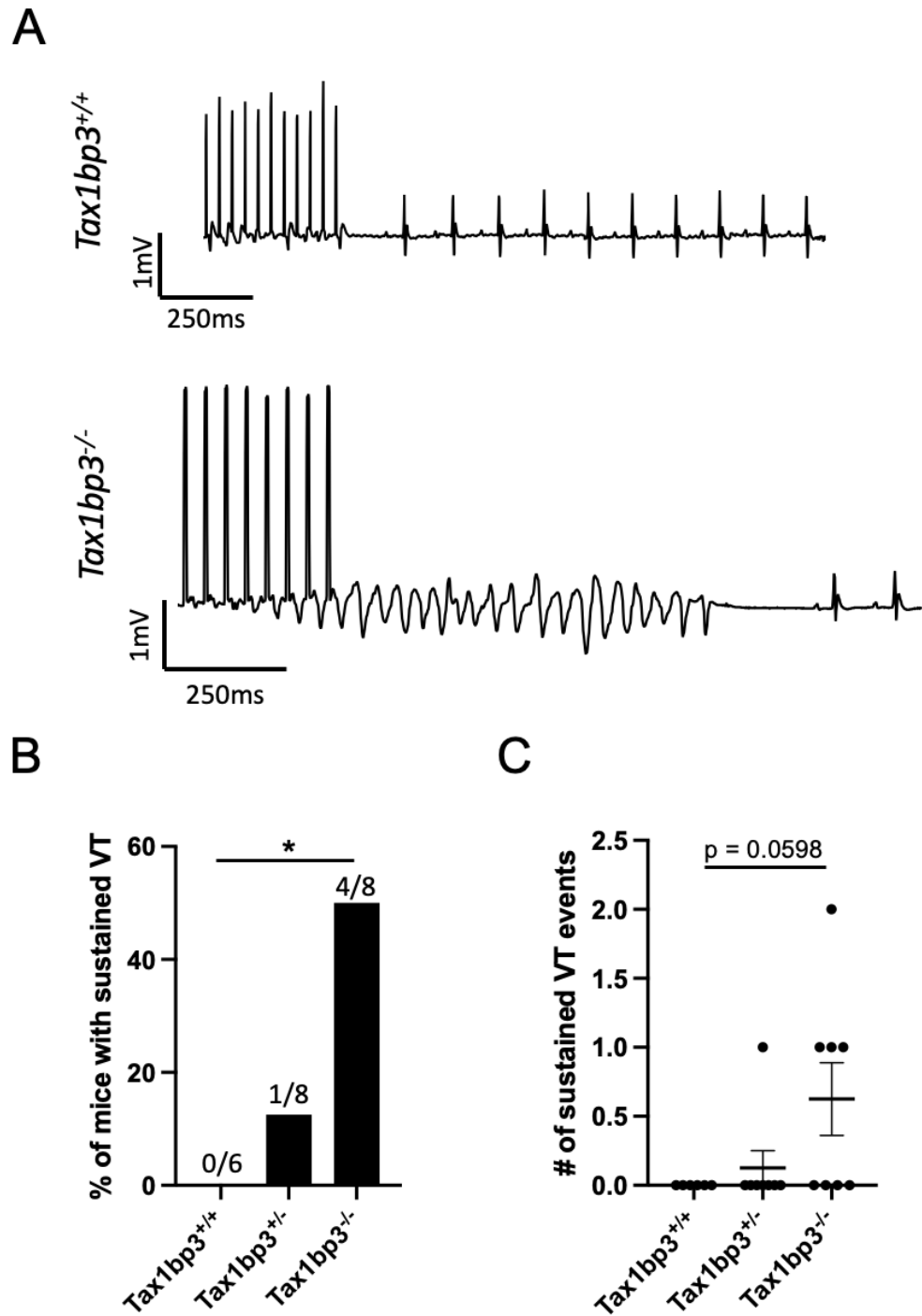


Figure 40: *Tax1bp3^{-/-}* mice have increased ventricular tachycardia with swimming exercise

A) Example surface ECG traces showing sinus rhythm (*Tax1bp3^{+/+}*) and sustained VT (*Tax1bp3^{-/-}*) following ventricular pacing. B) Quantification of the percentage of mice that had sustained VT

(*Tax1bp3*^{+/+} vs. *Tax1bp3*^{-/-} p = 0.0404). C) Quantification of the number of sustained VT events per mouse (mean ± s.e.m. n mice = 6, 8, 8). * p < 0.05, ** p < 0.01, *** p < 0.0

10. Conclusions and future directions

ACM is considered a genetic disease and most ACM-associated variants are in genes encoding components of the cardiac desmosome (*DSC2*, *DSG2*, *DSP*, *JUP*, *PKP2*) and comprise the bulk of genes investigated on clinical genetic testing panels. (Austin, Trembley et al. 2019) However, ACM development has been associated less commonly in variants within non-desmosomal genes, including in *TMEM43*, *CTNNA3*, *DES*, *LMNA*, *PLN*, *TTN*, and *SCN5A*. Inheritance is typically autosomal dominant, with rare cases of autosomal recessive forms that include Naxos disease and Carvajal syndrome (Protonotarios and Tsatsopoulou 2004). In the last decade, ES and genome sequencing have exponentially increased the identification of new Mendelian disease genes, enabling downstream studies to better understand disease pathophysiology (Lee, Deignan et al. 2014). Using exome sequencing, we identified a sibship with biallelic variants *TAX1BP3* which co-segregate with pediatric-onset ACM with complete penetrance. We generated iPSC-CMs from this sibship and found that the affected cells were arrhythmogenic with increased Ca^{2+} leak from the SR. Because both parents had normal cardiac evaluations, we made a *Tax1bp3*^{-/-} mouse to study the direct effects of genetic *Tax1bp3* loss. These mice showed increased Ca^{2+} leak and arrhythmia predisposition, recapitulating the cellular phenotype. We also found that TRPV4 changes localization in both models to sarcolemma and t-tubules. Inhibition of TRPV4 with the small molecule HC-067047 suppressed Ca^{2+} leak in iPSC-CMs from this family, *Tax1bp3*^{-/-} mouse isolated ventricular myocytes, and iPSC-CMs derived from an ACM patient harboring a PKP2 p.His773AlafsX8 variant, suggesting that TRPV4-mediated Ca^{2+} leak is a novel mechanism of ACM and that TRPV4 could be a new therapeutic target.

We have illustrated a novel genetic cause of ACM, but our study was limited to a single sibship, with our case-matching efforts yet to yield other similarly affected individuals.

Additional exploration of *TAX1BP3* in large genotype-negative cohorts of ACM patients may result in validation of this finding. Further reports of ACM or other cardiomyopathies in individuals with biallelic *TAX1BP3* variants would establish an association more definitively, and we believe that our study would increase the possibility of other centers looking at their gene-elusive cases. We consider the p.M78T/del genotype to be causative for ACM due to the strong correlation with the clinical phenotype and ACM-like phenotypes of fat accumulation and Ca²⁺ leak in the iPSC-CMs. *TAX1BP3* overexpression in the iPSC-CM^{M78T/del} was sufficient to rescue Ca²⁺ leak. Furthermore, knockout of *Tax1bp3* in the mouse heart was sufficient to cause Ca²⁺ leak and ventricular arrhythmias.

Prior to this study, the function of *TAX1BP3* in the heart had not yet been studied. There is a single report linking a homozygous *TAX1BP3* variant to dilated cardiomyopathy, indicating that changes to *TAX1BP3* function may not solely cause ACM and may cause other forms of cardiomyopathy (Reinstein, Orvin et al. 2015), a common phenomenon within cardiomyopathy genes. However, the affected brothers in this report also had septo-optic dysplasia with corresponding brain MRI findings and the relevance of these to *TAX1BP3* is unclear at this time. Additionally, knockdown of *TAX1BP3* in zebrafish has been shown to increase mortality rate of embryos and enlarge the head and pericardium (Besser, Leito et al. 2007). *TAX1BP3* is a relatively small protein of 124 amino acids (13.74 kDa) and is predicted to consist of a single PDZ domain (Cui, Hayashi et al. 2007). These domains are common protein interaction sites, and *TAX1BP3* has been shown to physically interact with other proteins with this domain such as β -catenin and rhotekin (Reynaud, Fabre and Jalinot 2000, Kanamori, Sandy et al. 2003, Lee and Zheng 2010). Notably, we did not see any changes to Wnt or Rho signaling in the iPSC-CM RNA-sequencing which suggests a novel role in the heart. A next step to explore this further would be do RNA-sequencing on the *Tax1pb3*^{-/-} mice compared with *Tax1pb3*^{+/+} as that could unveil differences

specific to *Tax1bp3*, since the iPSC lines have genetic deletions that also include genes other than TAX1BP3, plus remove any sex-specific effects. Proteomic studies to investigate TAX1BP3 binding partners in the heart would also be a critical next step.

There has long been debate regarding the origin of fibrofatty tissue in ACM (Kohela and van Rooij 2022). Although it appears that the iPSC-CMs have intracellular lipid droplets, we cannot exclude the possibility of a lineage shift of the iPSC-CMs towards an adipocyte-like cell, so more exploration of this model is needed. Further immunofluorescence studies could be performed to begin identifying the cellular identities of the cells that have greater lipid staining such as staining with adipocyte or fibroblast markers. We also did not see evidence of fibrofatty tissue in the *Tax1bp3*^{-/-} mice. Modeling ACM-like fibrofatty replacement in mice has historically been a challenge, likely due to differences in both the localization and generation of fat tissue in mice compared with humans (Yamaguchi, Cavallero et al. 2015, Kohela and van Rooij 2022). It is also possible that because we did not age out the mice past 6 months, we are modeling the concealed, arrhythmogenic phase of ACM, and not the later stage cardiac remodeling and heart failure. Sedentary *PKP2*-mediated ACM mouse models also often lack fat accumulation (Moncayo-Arlandi, Guasch et al. 2016, van Opbergen, Noorman et al. 2019, Camors, Roth et al. 2022). We could repeat the experiments and age the mice out to 12 months before collecting the hearts for histological analysis.

An unexpected finding is that the SR store is low while the transient amplitude is maintained. Typically, with a reduced SR store one would expect the transient amplitude to be decreased, as is the case in reduced EF heart failure models. It is possible that TAX1BP3-mediated Ca²⁺-changes are distinct. Specifically, the I_{TRPV4} is loading the cell with Ca²⁺, and thus maintaining calcium-induced calcium release (CICR) despite the lower SR store. The phenomenon is similar to the calcium dynamic in catecholaminergic polymorphic ventricular tachycardia (CPVT) wherein

the SR store is reduced and yet the cells maintain no change in transient amplitude (Word, Quick et al. 2021). As the *in vivo* model is arrhythmic with minimal cardiac remodeling, we believe that the Ca^{2+} dynamics in the setting of *TAXIBP3* loss aligns more with arrhythmia models like CPVT, rather than heart failure. To confirm that the SR store is in fact reduced and not a product of variable iPSC-CM differentiation and maturity, a future direction is to repeat these experiments in the *Tax1bp3*^{-/-} mice.

Of note, we find increased *TRPV4* mRNA expression, localization of Trpv4 to the dyad in *Tax1bp3*^{-/-} mice, and presence of I_{TRPV4} in iPSC-CM^{M78T/del} cells. A previous study had found in isolated neonatal rat ventricular myocytes that Trpv4 was predominately localized to the nucleus which we also found in our *Tax1bp3*^{+/+} mice (Zhao, Huang et al. 2012). TRPV4 is known to have a nuclear localization signal (Méndez-Gómez, Espadas-Álvarez et al. 2022). Proteins that have been implicated to affect TRPV4 trafficking include OS-9, PACSIN3, STIM1, and β -arrestin-1 and 2 (Cuajungco, Grimm et al. 2006, Wang, Fu et al. 2007, Shukla, Kim et al. 2010, Shin, Lee et al. 2015, Ying, Becard et al. 2015). Further studies will be necessary to determine what mediates the change in TRPV4 trafficking in this model.

Because of the rescue of Ca^{2+} leak in the PKP2-fs iPSC-CM model, it is possible that TRPV4-mediated arrhythmogenesis is a broader phenomenon in ACM. If so, it could be a novel therapeutic target for suppressing arrhythmogenesis, potentially even for other diseases that involve Ca^{2+} leak, such as catecholaminergic polymorphic ventricular tachycardia (Lehnart, Mongillo et al. 2008). This is an intriguing possibility given the report that TRPV4 inhibition suppresses atrial fibrillation in mice, which is also driven by Ca^{2+} leak (Liao, Wu et al. 2020). However, more studies are needed to understand how TRPV4 mediates calcium leak. It is possible that it is simply overloading the cytosol with calcium, leading to Ca^{2+} -induced Ca^{2+} leak of RyR2, and indeed, we do have increased cytosolic Ca^{2+} in our model. Another possibility is through calmodulin kinase II

(CaMKII). In an ischemia-reperfusion mouse model, TRPV4 activation induced CaMKII phosphorylation (Zhang, Lu et al. 2021), and increased CaMKII activity is associated with Ca²⁺ leak (Bers and Grandi 2009). It remains unknown how TRPV4 may directly, or indirectly, increase Ca²⁺ in cardiac myocytes. One possibility is that TRPV4 is directed to the membrane in these cells putting it in a physiologic to directly increased intracellular Ca²⁺ within the cardiac myocyte. It has been previously established that TRPV4 is expressed in the nucleus and perinucleus in cardiomyocytes (in mouse ventricular myocytes (Zhao, Huang et al. 2012, Jones, Peana et al. 2019) and in human iPSC-CMs (Qi, Li et al. 2015)) and that TRPV4 can change its localization and affect Ca²⁺ entry (Jones, Peana et al. 2019). Potentially TRPV4 translocation is a stress response, but it is not yet clear if this results in Ca²⁺ leak directly or indirectly. Understanding how *TAX1BP3* loss and the p.M78T variant results in changes in TRPV4 localization will need to be pursued in future studies. Additionally, more studies are also needed to test if TRPV4 inhibition will suppress the myocardial remodeling in ACM, however our study suggests that this strategy could be effective at suppressing arrhythmias.

To conclude, we have identified *TAX1BP3* loss as a novel genetic cause of autosomal recessive ACM. iPSC-CM^{M78T/del} lines have fat accumulation and are arrhythmogenic, the two hallmarks of ACM. We developed a *Tax1bp3*^{-/-} mouse model which is arrhythmogenic but lacks cardiac remodeling. We also found that TRPV4, a Ca²⁺ channel, is upregulated in iPSC-CM^{M78T/del} and mis-localized in *Tax1bp3*^{-/-} mice, and that these channels are sensitive to changing membrane current. Finally, we show that inhibiting TRPV4 with HC-067047 brings Ca²⁺ leak to WT levels in both the iPSC-CM and mouse models, as well as an additional ACM patient iPSC-CM model—suggesting that TRPV4 inhibition could be a potential therapeutic for ACM.

References

- Ackerman, M. J., S. G. Priori, S. Willems, C. Berul, R. Brugada, H. Calkins, A. J. Camm, P. T. Ellinor, M. Gollob, R. Hamilton, R. E. Hershberger, D. P. Judge, H. Le Marec, W. J. McKenna, E. Schulze-Bahr, C. Semsarian, J. A. Towbin, H. Watkins, A. Wilde, C. Wolpert and D. P. Zipes (2011). "HRS/EHRA Expert Consensus Statement on the State of Genetic Testing for the Channelopathies and Cardiomyopathies: This document was developed as a partnership between the Heart Rhythm Society (HRS) and the European Heart Rhythm Association (EHRA)." *Heart Rhythm* **8**(8): 1308-1339.
- Adzhubei, I. A., S. Schmidt, L. Peshkin, V. E. Ramensky, A. Gerasimova, P. Bork, A. S. Kondrashov and S. R. Sunyaev (2010). "A method and server for predicting damaging missense mutations." *Nat Methods* **7**(4): 248-249.
- Alsina, K. M., M. Hulsurkar, S. Brandenburg, D. Kownatzki-Danger, C. Lenz, H. Urlaub, I. Abu-Taha, M. Kamler, D. Y. Chiang, S. K. Lahiri, J. O. Reynolds, A. P. Quick, L. Scott, Jr., T. A. Word, M. D. Gelves, A. J. R. Heck, N. Li, D. Dobrev, S. E. Lehnart and X. H. T. Wehrens (2019). "Loss of Protein Phosphatase 1 Regulatory Subunit PPP1R3A Promotes Atrial Fibrillation." *Circulation* **140**(8): 681-693.
- Au - Li, N. and X. H. T. Au - Wehrens (2010). "Programmed Electrical Stimulation in Mice." *JoVE*(39): e1730.
- Austin, K. M., M. A. Trembley, S. F. Chandler, S. P. Sanders, J. E. Saffitz, D. J. Abrams and W. T. Pu (2019). "Molecular mechanisms of arrhythmogenic cardiomyopathy." *Nat Rev Cardiol* **16**(9): 519-537.
- Basso, C., B. Bauce, D. Corrado and G. Thiene (2012). "Pathophysiology of arrhythmogenic cardiomyopathy." *Nature Reviews Cardiology* **9**(4): 223-233.
- Benjamini, Y. and Y. Hochberg (1995). "Controlling the False Discovery Rate: A Practical and Powerful Approach to Multiple Testing." *Journal of the Royal Statistical Society. Series B (Methodological)* **57**(1): 289-300.
- Bennett, R. G., H. M. Haqqani, A. Berruezo, P. Della Bella, F. E. Marchlinski, C. J. Hsu and S. Kumar (2019). "Arrhythmogenic Cardiomyopathy in 2018-2019: ARVC/ALVC or Both?" *Heart Lung Circ* **28**(1): 164-177.
- Bers, D. M. and E. Grandi (2009). "Calcium/calmodulin-dependent kinase II regulation of cardiac ion channels." *J Cardiovasc Pharmacol* **54**(3): 180-187.

Besser, J., J. T. Leito, D. L. van der Meer and C. P. Bagowski (2007). "Tip-1 induces filopodia growth and is important for gastrulation movements during zebrafish development." *Dev Growth Differ* **49**(3): 205-214.

Binzenhöfer, L., S. Clauss, K. Strauß, J. Höpler, M. Kraft, S. Hoffmann, S. Brunner, P. Tomsits, D. Schüttler, S. Massberg, S. Käab and E. Lüsebrink (2024). "Life-time cumulative activity burden is associated with symptomatic heart failure and arrhythmic risk in patients with arrhythmogenic right ventricular cardiomyopathy: a retrospective cohort study." *EP Europace*.

Bolli, R. (2017). "New Initiatives to Improve the Rigor and Reproducibility of Articles Published in *Circulation Research*." *Circulation Research* **121**(5): 472-479.

Bosman, L. P., W. Wang, H. Lie Ø, F. H. M. van Lint, C. Rootwelt-Norberg, B. Murray, C. Tichnell, J. Cadrin-Tourigny, J. P. van Tintelen, F. W. Asselbergs, H. Calkins, A. Te Riele, K. H. Haugaa and C. A. James (2022). "Integrating Exercise Into Personalized Ventricular Arrhythmia Risk Prediction in Arrhythmogenic Right Ventricular Cardiomyopathy." *Circ Arrhythm Electrophysiol* **15**(2): e010221.

Bradford, W. H., J. Zhang, E. J. Gutierrez-Lara, Y. Liang, A. Do, T.-M. Wang, L. Nguyen, N. Matararachchi, J. Wang, Y. Gu, A. McCulloch, K. L. Peterson and F. Sheikh (2023). "Plakophilin 2 gene therapy prevents and rescues arrhythmogenic right ventricular cardiomyopathy in a mouse model harboring patient genetics." *Nature Cardiovascular Research* **2**(12): 1246-1261.

Burridge, P. W., E. Matsa, P. Shukla, Z. C. Lin, J. M. Churko, A. D. Ebert, F. Lan, S. Diecke, B. Huber, N. M. Mordwinkin, J. R. Plews, O. J. Abilez, B. Cui, J. D. Gold and J. C. Wu (2014). "Chemically defined generation of human cardiomyocytes." *Nature methods* **11**(8): 855-860.

Camors, E. M., A. H. Roth, J. R. Alef, R. D. Sullivan, J. N. Johnson, E. Purevjav and J. A. Towbin (2022). "Progressive Reduction in Right Ventricular Contractile Function Attributable to Altered Actin Expression in an Aging Mouse Model of Arrhythmogenic Cardiomyopathy." *Circulation* **145**(21): 1609-1624.

Cerrone, M., J. Montnach, X. Lin, Y. T. Zhao, M. Zhang, E. Agullo-Pascual, A. Leo-Macias, F. J. Alvarado, I. Dolgalev, T. V. Karathanos, K. Malkani, C. J. M. Van Opbergen, J. J. A. van Bavel, H. Q. Yang, C. Vasquez, D. Tester, S. Fowler, F. Liang, E. Rothenberg, A. Heguy, G. E. Morley, W. A. Coetzee, N. A. Trayanova, M. J. Ackerman, T. A. B. van Veen, H. H. Valdivia and M. Delmar (2017). "Plakophilin-2 is required for transcription of genes that control calcium cycling and cardiac rhythm." *Nat Commun* **8**(1): 106.

Chen, G., D. R. Gulbranson, Z. Hou, J. M. Bolin, V. Ruotti, M. D. Probasco, K. Smuga-Otto, S. E. Howden, N. R. Diol, N. E. Propson, R. Wagner, G. O. Lee, J. Antosiewicz-Bourget, J. M. Teng and J. A. Thomson (2011). "Chemically defined conditions for human iPSC derivation and culture." *Nat Methods* **8**(5): 424-429.

Chen, S., Y. Zhou, Y. Chen and J. Gu (2018). "fastp: an ultra-fast all-in-one FASTQ preprocessor." *Bioinformatics* **34**(17): i884-i890.

Cheng, J., A. Randall and P. Baldi (2006). "Prediction of protein stability changes for single-site mutations using support vector machines." *Proteins* **62**(4): 1125-1132.

Choi, Y. (2012). A fast computation of pairwise sequence alignment scores between a protein and a set of single-locus variants of another protein. *Proceedings of the ACM Conference on Bioinformatics, Computational Biology and Biomedicine*. Orlando, Florida, Association for Computing Machinery: 414-417.

Clasen, L., C. Eickholt, S. Angendohr, C. Jungen, D. I. Shin, B. Donner, A. Furnkranz, M. Kelm, N. Klocker, C. Meyer and H. Makimoto (2018). "A modified approach for programmed electrical stimulation in mice: Inducibility of ventricular arrhythmias." *PLoS One* **13**(8): e0201910.

Cooper, G. M., E. A. Stone, G. Asimenos, N. C. S. Program, E. D. Green, S. Batzoglou and A. Sidow (2005). "Distribution and intensity of constraint in mammalian genomic sequence." *Genome research* **15**(7): 901-913.

Corrado, D., C. Basso and D. P. Judge (2017). "Arrhythmogenic Cardiomyopathy." *Circulation Research* **121**(7): 784-802.

Corrado, D., C. Basso, G. Rizzoli, M. Schiavon and G. Thiene (2003). "Does sports activity enhance the risk of sudden death in adolescents and young adults?" *J Am Coll Cardiol* **42**(11): 1959-1963.

Cuajungco, M. P., C. Grimm, K. Oshima, D. D'Hoedt, B. Nilius, A. R. Mensenkamp, R. J. M. Bindels, M. Plomann and S. Heller (2006). "PACSINs Bind to the TRPV4 Cation Channel: PACSIN 3 MODULATES THE SUBCELLULAR LOCALIZATION OF TRPV4 *." *Journal of Biological Chemistry* **281**(27): 18753-18762.

Cui, H., A. Hayashi, H. S. Sun, M. P. Belmares, C. Cobey, T. Phan, J. Schweizer, M. W. Salter, Y. T. Wang, R. A. Tasker, D. Garman, J. Rabinowitz, P. S. Lu and M. Tymianski (2007). "PDZ protein interactions underlying NMDA receptor-mediated excitotoxicity and neuroprotection by PSD-95 inhibitors." *J Neurosci* **27**(37): 9901-9915.

Cunningham, F., P. Achuthan, W. Akanni, J. Allen, M R. Amode, I. M. Armean, R. Bennett, J. Bhai, K. Billis, S. Boddu, C. Cummins, C. Davidson, K. J. Dodiya, A. Gall, C. G. Girón, L. Gil, T. Grego, L. Haggerty, E. Haskell, T. Hourlier, O. G. Izuogu, S. H. Janacek, T. Juettemann, M. Kay, M. R. Laird, I. Lavidas, Z. Liu, Jane E. Loveland, J. C. Marugán, T. Maurel, A. C. McMahon, B. Moore, J. Morales, J. M. Mudge, M. Nuhn, D. Ogeh, A. Parker, A. Parton, M. Patricio, A. I. Abdul Salam, B. M. Schmitt, H. Schuilenburg, D. Sheppard, H. Sparrow, E. Stapleton, M. Szuba, K. Taylor, G. Threadgold, A. Thormann, A. Vullo, B. Walts, A. Winterbottom, A. Zadissa, M. Chakiachvili, A. Frankish, S. E. Hunt, M. Kostadima, N. Langridge, F. J. Martin, M. Muffato, E. Perry, M. Ruffier, D. M. Staines, S. J. Trevanion, B. L. Aken, A. D. Yates, D. R. Zerbino and P. Flicek (2018). "Ensembl 2019." *Nucleic Acids Research* **47**(D1): D745-D751.

Dobin, A., C. A. Davis, F. Schlesinger, J. Drenkow, C. Zaleski, S. Jha, P. Batut, M. Chaisson and T. R. Gingeras (2013). "STAR: ultrafast universal RNA-seq aligner." *Bioinformatics* **29**(1): 15-21.

Earley, S., T. J. Heppner, M. T. Nelson and J. E. Brayden (2005). "TRPV4 forms a novel Ca²⁺ signaling complex with ryanodine receptors and BKCa channels." *Circ Res* **97**(12): 1270-1279.

Finocchiaro, G., M. Papadakis, J. L. Robertus, H. Dhutia, A. K. Steriotis, M. Tome, G. Mellor, A. Merghani, A. Malhotra, E. Behr, S. Sharma and M. N. Sheppard (2016). "Etiology of Sudden Death in Sports: Insights From a United Kingdom Regional Registry." *J Am Coll Cardiol* **67**(18): 2108-2115.

Garcia-Gras, E., R. Lombardi, M. J. Giocondo, J. T. Willerson, M. D. Schneider, D. S. Khoury and A. J. Marian (2006). "Suppression of canonical Wnt/beta-catenin signaling by nuclear plakoglobin recapitulates phenotype of arrhythmogenic right ventricular cardiomyopathy." *J Clin Invest* **116**(7): 2012-2021.

Ginsburg, G. S., S. H. Shah and J. J. McCarthy (2007). "Taking cardiovascular genetic association studies to the next level." *J Am Coll Cardiol* **50**(10): 930-932.

Hoang-Trong, T. M., A. Ullah and M. S. Jafri (2015). "Calcium Sparks in the Heart: Dynamics and Regulation." *Res Rep Biol* **6**: 203-214.

Huber, W., V. J. Carey, R. Gentleman, S. Anders, M. Carlson, B. S. Carvalho, H. C. Bravo, S. Davis, L. Gatto, T. Girke, R. Gottardo, F. Hahne, K. D. Hansen, R. A. Irizarry, M. Lawrence, M. I. Love, J. MacDonald, V. Obenchain, A. K. Oles, H. Pagès, A. Reyes, P. Shannon, G. K. Smyth, D. Tenenbaum, L. Waldron and M. Morgan (2015). "Orchestrating high-throughput genomic analysis with Bioconductor." *Nat Methods* **12**(2): 115-121.

Ignatiadis, N., B. Klaus, J. B. Zaugg and W. Huber (2016). "Data-driven hypothesis weighting increases detection power in genome-scale multiple testing." *Nat Methods* **13**(7): 577-580.

Ioannidis, N. M., J. H. Rothstein, V. Pejaver, S. Middha, S. K. McDonnell, S. Baheti, A. Musolf, Q. Li, E. Holzinger, D. Karyadi, L. A. Cannon-Albright, C. C. Teerlink, J. L. Stanford, W. B. Isaacs, J. Xu, K. A. Cooney, E. M. Lange, J. Schleutker, J. D. Carpten, I. J. Powell, O. Cussenot, G. Cancel-Tassin, G. G. Giles, R. J. MacInnis, C. Maier, C.-L. Hsieh, F. Wiklund, W. J. Catalona, W. D. Foulkes, D. Mandal, R. A. Eeles, Z. Kote-Jarai, C. D. Bustamante, D. J. Schaid, T. Hastie, E. A. Ostrander, J. E. Bailey-Wilson, P. Radivojac, S. N. Thibodeau, A. S. Whittemore and W. Sieh (2016). "REVEL: An Ensemble Method for Predicting the Pathogenicity of Rare Missense Variants." *American journal of human genetics* **99**(4): 877-885.

James, C. A., A. Bhonsale, C. Tichnell, B. Murray, S. D. Russell, H. Tandri, R. J. Tedford, D. P. Judge and H. Calkins (2013). "Exercise increases age-related penetrance and arrhythmic risk in arrhythmogenic right ventricular dysplasia/cardiomyopathy-associated desmosomal mutation carriers." *J Am Coll Cardiol* **62**(14): 1290-1297.

James, C. A., J. D. H. Jongbloed, R. E. Hershberger, A. Morales, D. P. Judge, P. Syrris, K. Pilichou, A. M. Domingo, B. Murray, J. Cadrin-Tourigny, R. Lekanne Deprez, R. Celeghin, A. Protonotarios, B. Asatryan, E. Brown, E. Jordan, J. McGlaughon, C. Thaxton, C. L. Kurtz and J. P. van Tintelen (2021). "International Evidence Based Reappraisal of Genes Associated With Arrhythmogenic Right Ventricular Cardiomyopathy Using the Clinical Genome Resource Framework." *Circ Genom Precis Med* **14**(3): e003273.

Jones, J. L., D. Peana, A. B. Veteto, M. D. Lambert, Z. Nourian, N. G. Karasseva, M. A. Hill, B. R. Lindman, C. P. Baines, M. Krenz and T. L. Domeier (2019). "TRPV4 increases cardiomyocyte calcium cycling and contractility yet contributes to damage in the aged heart following hypoosmotic stress." *Cardiovasc Res* **115**(1): 46-56.

Kanamori, M., P. Sandy, S. Marzinotto, R. Benetti, C. Kai, Y. Hayashizaki, C. Schneider and H. Suzuki (2003). "The PDZ protein tax-interacting protein-1 inhibits beta-catenin transcriptional activity and growth of colorectal cancer cells." *J Biol Chem* **278**(40): 38758-38764.

Karczewski, K. J., L. C. Francioli, G. Tiao, B. B. Cummings, J. Alföldi, Q. Wang, R. L. Collins, K. M. Laricchia, A. Ganna, D. P. Birnbaum, L. D. Gauthier, H. Brand, M. Solomonson, N. A. Watts, D. Rhodes, M. Singer-Berk, E. M. England, E. G. Seaby, J. A. Kosmicki, R. K. Walters, K. Tashman, Y. Farjoun, E. Banks, T. Potterba, A. Wang, C. Seed, N. Whiffin, J. X. Chong, K. E. Samocha, E. Pierce-Hoffman, Z. Zappala, A. H. O'Donnell-Luria, E. V. Minikel, B. Weisburd, M. Lek, J. S. Ware, C. Vittal, I. M. Armean, L. Bergelson, K. Cibulskis, K. M. Connolly, M. Covarrubias, S. Donnelly, S. Ferriera, S. Gabriel, J. Gentry, N. Gupta, T. Jeandet, D. Kaplan, C. Llanwarne, R. Munshi, S. Novod, N. Petrillo, D. Roazen, V. Ruano-Rubio, A. Saltzman, M. Schleicher, J. Soto, K. Tibbetts, C. Tolonen, G. Wade, M. E. Talkowski, C. A. Aguilar Salinas, T. Ahmad, C. M. Albert, D. Ardissino, G. Atzmon, J. Barnard, L. Beaugerie, E. J. Benjamin, M.

Boehnke, L. L. Bonnycastle, E. P. Bottinger, D. W. Bowden, M. J. Bown, J. C. Chambers, J. C. Chan, D. Chasman, J. Cho, M. K. Chung, B. Cohen, A. Correa, D. Dabelea, M. J. Daly, D. Darbar, R. Duggirala, J. Dupuis, P. T. Ellinor, R. Elosua, J. Erdmann, T. Esko, M. Färkkilä, J. Florez, A. Franke, G. Getz, B. Glaser, S. J. Glatt, D. Goldstein, C. Gonzalez, L. Groop, C. Haiman, C. Hanis, M. Harms, M. Hiltunen, M. M. Holi, C. M. Hultman, M. Kallela, J. Kaprio, S. Kathiresan, B.-J. Kim, Y. J. Kim, G. Kirov, J. Kooner, S. Koskinen, H. M. Krumholz, S. Kugathasan, S. H. Kwak, M. Laakso, T. Lehtimäki, R. J. F. Loos, S. A. Lubitz, R. C. W. Ma, D. G. MacArthur, J. Marrugat, K. M. Mattila, S. McCarroll, M. I. McCarthy, D. McGovern, R. McPherson, J. B. Meigs, O. Melander, A. Metspalu, B. M. Neale, P. M. Nilsson, M. C. O'Donovan, D. Ongur, L. Orozco, M. J. Owen, C. N. A. Palmer, A. Palotie, K. S. Park, C. Pato, A. E. Pulver, N. Rahman, A. M. Remes, J. D. Rioux, S. Ripatti, D. M. Roden, D. Saleheen, V. Salomaa, N. J. Samani, J. Scharf, H. Schunkert, M. B. Shoemaker, P. Sklar, H. Soininen, H. Sokol, T. Spector, P. F. Sullivan, J. Suvisaari, E. S. Tai, Y. Y. Teo, T. Tiinamaija, M. Tsuang, D. Turner, T. Tusie-Luna, E. Vartiainen, J. S. Ware, H. Watkins, R. K. Weersma, M. Wessman, J. G. Wilson, R. J. Xavier, B. M. Neale, M. J. Daly, D. G. MacArthur and C. Genome Aggregation Database (2020). "The mutational constraint spectrum quantified from variation in 141,456 humans." *Nature* **581**(7809): 434-443.

Kersey, P. J., D. M. Staines, D. Lawson, E. Kulesha, P. Derwent, J. C. Humphrey, D. S. Hughes, S. Keenan, A. Kerhornou, G. Koscielny, N. Langridge, M. D. McDowall, K. Megy, U. Maheswari, M. Nuhn, M. Paulini, H. Pedro, I. Toneva, D. Wilson, A. Yates and E. Birney (2012). "Ensembl Genomes: an integrative resource for genome-scale data from non-vertebrate species." *Nucleic Acids Res* **40**(Database issue): D91-97.

Kim, C., J. Wong, J. Wen, S. Wang, C. Wang, S. Spiering, N. G. Kan, S. Forcales, P. L. Puri, T. C. Leone, J. E. Marine, H. Calkins, D. P. Kelly, D. P. Judge and H.-S. V. Chen (2013). "Studying arrhythmogenic right ventricular dysplasia with patient-specific iPSCs." *Nature* **494**(7435): 105-110.

Kohela, A. and E. van Rooij (2022). "Fibro-fatty remodelling in arrhythmogenic cardiomyopathy." *Basic Res Cardiol* **117**(1): 22.

Krahn, A. D., A. A. M. Wilde, H. Calkins, A. La Gerche, J. Cadrin-Tourigny, J. D. Roberts and H. C. Han (2022). "Arrhythmogenic Right Ventricular Cardiomyopathy." *JACC Clin Electrophysiol* **8**(4): 533-553.

Landrum, M. J., J. M. Lee, M. Benson, G. R. Brown, C. Chao, S. Chitipiralla, B. Gu, J. Hart, D. Hoffman, W. Jang, K. Karapetyan, K. Katz, C. Liu, Z. Maddipatla, A. Malheiro, K. McDaniel, M. Ovetsky, G. Riley, G. Zhou, J. B. Holmes, B. L. Kattman and D. R. Maglott (2018). "ClinVar: improving access to variant interpretations and supporting evidence." *Nucleic Acids Res* **46**(D1): D1062-d1067.

Landstrom, A. P., J. J. Kim, B. D. Gelb, B. M. Helm, P. J. Kannankeril, C. Semsarian, A. C. Sturm, M. Tristani-Firouzi and S. M. Ware (2021). "Genetic Testing for Heritable Cardiovascular Diseases in Pediatric Patients: A Scientific Statement From the American Heart Association." *Circulation: Genomic and Precision Medicine* **14**(5): e000086.

Lee, H., J. L. Deignan, N. Dorrani, S. P. Strom, S. Kantarci, F. Quintero-Rivera, K. Das, T. Toy, B. Harry, M. Yourshaw, M. Fox, B. L. Fogel, J. A. Martinez-Agosto, D. A. Wong, V. Y. Chang, P. B. Shieh, C. G. S. Palmer, K. M. Dipple, W. W. Grody, E. Vilain and S. F. Nelson (2014). "Clinical Exome Sequencing for Genetic Identification of Rare Mendelian Disorders." *JAMA* **312**(18): 1880-1887.

Lee, H.-J. and J. J. Zheng (2010). "PDZ domains and their binding partners: structure, specificity, and modification." *Cell Communication and Signaling* **8**(1): 8.

Lehnart, S. E., M. Mongillo, A. Bellinger, N. Lindegger, B. X. Chen, W. Hsueh, S. Reiken, A. Wronska, L. J. Drew, C. W. Ward, W. J. Lederer, R. S. Kass, G. Morley and A. R. Marks (2008). "Leaky Ca²⁺ release channel/ryanodine receptor 2 causes seizures and sudden cardiac death in mice." *J Clin Invest* **118**(6): 2230-2245.

Lek, M., K. J. Karczewski, E. V. Minikel, K. E. Samocha, E. Banks, T. Fennell, A. H. O'Donnell-Luria, J. S. Ware, A. J. Hill, B. B. Cummings, T. Tukiainen, D. P. Birnbaum, J. A. Kosmicki, L. E. Duncan, K. Estrada, F. Zhao, J. Zou, E. Pierce-Hoffman, J. Berghout, D. N. Cooper, N. Deflaux, M. DePristo, R. Do, J. Flannick, M. Fromer, L. Gauthier, J. Goldstein, N. Gupta, D. Howrigan, A. Kiezun, M. I. Kurki, A. L. Moonshine, P. Natarajan, L. Orozco, G. M. Peloso, R. Poplin, M. A. Rivas, V. Ruano-Rubio, S. A. Rose, D. M. Ruderfer, K. Shakir, P. D. Stenson, C. Stevens, B. P. Thomas, G. Tiao, M. T. Tusie-Luna, B. Weisburd, H. H. Won, D. Yu, D. M. Altshuler, D. Ardissino, M. Boehnke, J. Danesh, S. Donnelly, R. Elosua, J. C. Florez, S. B. Gabriel, G. Getz, S. J. Glatt, C. M. Hultman, S. Kathiresan, M. Laakso, S. McCarroll, M. I. McCarthy, D. McGovern, R. McPherson, B. M. Neale, A. Palotie, S. M. Purcell, D. Saleheen, J. M. Scharf, P. Sklar, P. F. Sullivan, J. Tuomilehto, M. T. Tsuang, H. C. Watkins, J. G. Wilson, M. J. Daly, D. G. MacArthur and C. Exome Aggregation (2016). "Analysis of protein-coding genetic variation in 60,706 humans." *Nature* **536**(7616): 285-291.

Liao, J., Q. Wu, C. Qian, N. Zhao, Z. Zhao, K. Lu, S. Zhang, Q. Dong, L. Chen, Q. Li and Y. Du (2020). "TRPV4 blockade suppresses atrial fibrillation in sterile pericarditis rats." *JCI Insight* **5**(23).

Lie Ø, H., L. A. Dejgaard, J. Saberniak, C. Rootwelt, M. K. Stokke, T. Edvardsen and K. H. Haugaa (2018). "Harmful Effects of Exercise Intensity and Exercise Duration in Patients With Arrhythmogenic Cardiomyopathy." *JACC Clin Electrophysiol* **4**(6): 744-753.

Love, M. I., W. Huber and S. Anders (2014). "Moderated estimation of fold change and dispersion for RNA-seq data with DESeq2." *Genome Biology* **15**(12): 550.

Lüsebrink, E., L. Binzenhöfer, S. Brunner, J. Hausleiter, S. Massberg, M. Orban and S. Kääh (2021). "How exercise can deteriorate the clinical course of an ARVC patient: a case report." *Eur Heart J Case Rep* **5**(11): ytab417.

Marcus, F. I., W. J. McKenna, D. Sherrill, C. Basso, B. Baucé, D. A. Bluemke, H. Calkins, D. Corrado, M. G. P. J. Cox, J. P. Daubert, G. Fontaine, K. Gear, R. Hauer, A. Nava, M. H. Picard, N. Protonotarios, J. E. Saffitz, D. M. Y. Sanborn, J. S. Steinberg, H. Tandri, G. Thiene, J. A. Towbin, A. Tsatsopoulou, T. Wichter and W. Zareba (2010). "Diagnosis of Arrhythmogenic Right Ventricular Cardiomyopathy/Dysplasia." *Circulation* **121**(13): 1533-1541.

McKoy, G., N. Protonotarios, A. Crosby, A. Tsatsopoulou, A. Anastasakis, A. Coonar, M. Norman, C. Baboonian, S. Jeffery and W. J. McKenna (2000). "Identification of a deletion in plakoglobin in arrhythmogenic right ventricular cardiomyopathy with palmoplantar keratoderma and woolly hair (Naxos disease)." *Lancet* **355**(9221): 2119-2124.

Méndez-Gómez, S., H. Espadas-Álvarez, I. Ramírez-Rodríguez, L. Domínguez-Malfavón and R. García-Villegas (2022). "The amino-terminal domain of TRPV4 channel is involved in its trafficking to the nucleus." *Biochem Biophys Res Commun* **592**: 13-17.

Moccia, F., F. Lodola, I. Stadiotti, C. A. Pilato, M. Bellin, S. Carugo, G. Pompilio, E. Sommariva and A. S. Maione (2019). "Calcium as a Key Player in Arrhythmogenic Cardiomyopathy: Adhesion Disorder or Intracellular Alteration?" *Int J Mol Sci* **20**(16).

Mohamed, B. A., N. Hartmann, P. Tirilomis, K. Sekeres, W. Li, S. Neef, C. Richter, E. M. Zeisberg, L. Kattner, M. Didié, K. Guan, J. D. Schmitto, S. E. Lehnart, S. Luther, N. Voigt, T. Seidler, S. Sossalla, G. Hasenfuss and K. Toischer (2018). "Sarcoplasmic reticulum calcium leak contributes to arrhythmia but not to heart failure progression." *Sci Transl Med* **10**(458).

Moncayo-Arlandi, J., E. Guasch, M. Sanz-de la Garza, M. Casado, N. A. Garcia, L. Mont, M. Sitges, R. Knöll, B. Buyandelger, O. Campuzano, A. Diez-Juan and R. Brugada (2016). "Molecular disturbance underlies to arrhythmogenic cardiomyopathy induced by transgene content, age and exercise in a truncated PKP2 mouse model." *Hum Mol Genet* **25**(17): 3676-3688.

Musunuru, K., R. E. Hershberger, S. M. Day, N. J. Klinedinst, A. P. Landstrom, V. N. Parikh, S. Prakash, C. Semsarian and A. C. Sturm (2020). "Genetic Testing for Inherited Cardiovascular Diseases: A Scientific Statement From the American Heart Association." *Circ Genom Precis Med* **13**(4): e000067.

O'Connell, T. D., M. C. Rodrigo and P. C. Simpson (2007). "Isolation and culture of adult mouse cardiac myocytes." *Methods Mol Biol* **357**: 271-296.

Orgeron, G. M. and H. Calkins (2016). "Advances in the Diagnosis and Management of Arrhythmogenic Right Ventricular Dysplasia/Cardiomyopathy." *Current Cardiology Reports* **18**(6): 53.

Picht, E., A. V. Zima, L. A. Blatter and D. M. Bers (2007). "SparkMaster: automated calcium spark analysis with ImageJ." *Am J Physiol Cell Physiol* **293**(3): C1073-1081.

Prior, D. and A. La Gerche (2020). "Exercise and Arrhythmogenic Right Ventricular Cardiomyopathy." *Heart Lung Circ* **29**(4): 547-555.

Protonotarios, N. and A. Tsatsopoulou (2004). "Naxos disease and Carvajal syndrome: cardiocutaneous disorders that highlight the pathogenesis and broaden the spectrum of arrhythmogenic right ventricular cardiomyopathy." *Cardiovasc Pathol* **13**(4): 185-194.

Qi, Y., Z. Li, C.-W. Kong, N. L. Tang, Y. Huang, R. A. Li and X. Yao (2015). "Uniaxial cyclic stretch stimulates TRPV4 to induce realignment of human embryonic stem cell-derived cardiomyocytes." *Journal of Molecular and Cellular Cardiology* **87**: 65-73.

Reinstein, E., K. Orvin, E. Tayeb-Fligelman, H. Stiebel-Kalish, S. Tzur, A. L. Pimienta, L. Bazak, T. Bengal, L. Cohen, D. D. Gatton, C. Bormans, M. Landau, R. Kornowski, M. Shohat and D. M. Behar (2015). "Mutations in TAX1BP3 Cause Dilated Cardiomyopathy with Septo-Optic Dysplasia." *Human Mutation* **36**(4): 439-442.

Reynaud, C., S. Fabre and P. Jalinot (2000). "The PDZ protein TIP-1 interacts with the Rho effector rhotekin and is involved in Rho signaling to the serum response element." *J Biol Chem* **275**(43): 33962-33968.

Richards, S., N. Aziz, S. Bale, D. Bick, S. Das, J. Gastier-Foster, W. W. Grody, M. Hegde, E. Lyon, E. Spector, K. Voelkerding and H. L. Rehm (2015). "Standards and guidelines for the interpretation of sequence variants: a joint consensus recommendation of the American College of Medical Genetics and Genomics and the Association for Molecular Pathology." *Genet Med* **17**(5): 405-424.

Ruwald, A. C., F. Marcus, N. A. Estes, 3rd, M. Link, S. McNitt, B. Polonsky, H. Calkins, J. A. Towbin, A. J. Moss and W. Zareba (2015). "Association of competitive and recreational sport participation with cardiac events in patients with arrhythmogenic right ventricular

cardiomyopathy: results from the North American multidisciplinary study of arrhythmogenic right ventricular cardiomyopathy." *Eur Heart J* **36**(27): 1735-1743.

Saberniak, J., N. E. Hasselberg, R. Borgquist, P. G. Platonov, S. I. Sarvari, H. J. Smith, M. Ribe, A. G. Holst, T. Edvardsen and K. H. Haugaa (2014). "Vigorous physical activity impairs myocardial function in patients with arrhythmogenic right ventricular cardiomyopathy and in mutation positive family members." *Eur J Heart Fail* **16**(12): 1337-1344.

Shashi, V., K. Schoch, R. Spillmann, H. Cope, Q. K. Tan, N. Walley, L. Pena, A. McConkie-Rosell, Y. H. Jiang, N. Stong, A. C. Need and D. B. Goldstein (2019). "A comprehensive iterative approach is highly effective in diagnosing individuals who are exome negative." *Genet Med* **21**(1): 161-172.

Shin, S. H., E. J. Lee, J. Chun, S. Hyun and S. S. Kang (2015). "Phosphorylation on TRPV4 Serine 824 Regulates Interaction with STIM1." *Open Biochem J* **9**: 24-33.

Shukla, A. K., J. Kim, S. Ahn, K. Xiao, S. K. Shenoy, W. Liedtke and R. J. Lefkowitz (2010). "Arresting a transient receptor potential (TRP) channel: beta-arrestin 1 mediates ubiquitination and functional down-regulation of TRPV4." *J Biol Chem* **285**(39): 30115-30125.

Sikkel, M. B., D. P. Francis, J. Howard, F. Gordon, C. Rowlands, N. S. Peters, A. R. Lyon, S. E. Harding and K. T. MacLeod (2017). "Hierarchical statistical techniques are necessary to draw reliable conclusions from analysis of isolated cardiomyocyte studies." *Cardiovasc Res* **113**(14): 1743-1752.

Stephens, M. (2016). "False discovery rates: a new deal." *Biostatistics* **18**(2): 275-294.

Tadros, H. J., C. Y. Miyake, D. L. Kearney, J. J. Kim and S. W. Denfield (2023). "The Many Faces of Arrhythmogenic Cardiomyopathy: An Overview." *Appl Clin Genet* **16**: 181-203.

Tang, H. and P. D. Thomas (2016). "PANTHER-PSEP: predicting disease-causing genetic variants using position-specific evolutionary preservation." *Bioinformatics* **32**(14): 2230-2232.

Towbin, J. A., W. J. McKenna, D. J. Abrams, M. J. Ackerman, H. Calkins, F. C. C. Darrieux, J. P. Daubert, C. de Chillou, E. C. DePasquale, M. Y. Desai, N. A. M. Estes, 3rd, W. Hua, J. H. Indik, J. Ingles, C. A. James, R. M. John, D. P. Judge, R. Keegan, A. D. Krahn, M. S. Link, F. I. Marcus, C. J. McLeod, L. Mestroni, S. G. Priori, J. E. Saffitz, S. Sanatani, W. Shimizu, J. P. van Tintelen, A. A. M. Wilde and W. Zareba (2019). "2019 HRS expert consensus statement on evaluation, risk stratification, and management of arrhythmogenic cardiomyopathy." *Heart Rhythm* **16**(11): e301-e372.

Uhlén, M., L. Fagerberg, B. M. Hallström, C. Lindskog, P. Oksvold, A. Mardinoglu, Å. Sivertsson, C. Kampf, E. Sjöstedt, A. Asplund, I. Olsson, K. Edlund, E. Lundberg, S. Navani, C. A. Szigartyo, J. Odeberg, D. Djureinovic, J. O. Takanen, S. Hober, T. Alm, P. H. Edqvist, H. Berling, H. Tegel, J. Mulder, J. Rockberg, P. Nilsson, J. M. Schwenk, M. Hamsten, K. von Feilitzen, M. Forsberg, L. Persson, F. Johansson, M. Zwahlen, G. von Heijne, J. Nielsen and F. Pontén (2015). "Proteomics. Tissue-based map of the human proteome." *Science* **347**(6220): 1260419.

van Opbergen, C. J. M., B. Narayanan, C. B. Sacramento, K. M. Stiles, V. Mishra, E. Frenk, D. Ricks, G. Chen, M. Zhang, P. Yarabe, J. Schwartz, M. Delmar, C. D. Herzog and M. Cerrone (2024). "AAV-Mediated Delivery of Plakophilin-2a Arrests Progression of Arrhythmogenic Right Ventricular Cardiomyopathy in Murine Hearts: Preclinical Evidence Supporting Gene Therapy in Humans." *Circulation: Genomic and Precision Medicine* **17**(1): e004305.

van Opbergen, C. J. M., M. Noorman, A. Pfenniger, J. S. Copier, S. H. Vermij, Z. Li, R. van der Nagel, M. Zhang, J. M. T. de Bakker, A. M. Glass, P. J. Mohler, S. M. Taffet, M. A. Vos, H. V. M. van Rijen, M. Delmar and T. A. B. van Veen (2019). "Plakophilin-2 Haploinsufficiency Causes Calcium Handling Deficits and Modulates the Cardiac Response Towards Stress." *Int J Mol Sci* **20**(17).

Vaser, R., S. Adusumalli, S. N. Leng, M. Sikic and P. C. Ng (2016). "SIFT missense predictions for genomes." *Nat Protoc* **11**(1): 1-9.

Voigt, N., J. Heijman, Q. Wang, D. Y. Chiang, N. Li, M. Karck, X. H. T. Wehrens, S. Nattel and D. Dobrev (2014). "Cellular and molecular mechanisms of atrial arrhythmogenesis in patients with paroxysmal atrial fibrillation." *Circulation* **129**(2): 145-156.

Voigt, N., N. Li, Q. Wang, W. Wang, A. W. Trafford, I. Abu-Taha, Q. Sun, T. Wieland, U. Ravens, S. Nattel, X. H. Wehrens and D. Dobrev (2012). "Enhanced sarcoplasmic reticulum Ca²⁺ leak and increased Na⁺-Ca²⁺ exchanger function underlie delayed afterdepolarizations in patients with chronic atrial fibrillation." *Circulation* **125**(17): 2059-2070.

Wang, Y., X. Fu, S. Gaiser, M. Köttgen, A. Kramer-Zucker, G. Walz and T. Wegierski (2007). "OS-9 Regulates the Transit and Polyubiquitination of TRPV4 in the Endoplasmic Reticulum." *Journal of Biological Chemistry* **282**(50): 36561-36570.

Wehrens, X. H., S. E. Lehnart, F. Huang, J. A. Vest, S. R. Reiken, P. J. Mohler, J. Sun, S. Guatimosim, L. S. Song, N. Rosembli, J. M. D'Armiento, C. Napolitano, M. Memmi, S. G. Priori, W. J. Lederer and A. R. Marks (2003). "FKBP12.6 deficiency and defective calcium release channel (ryanodine receptor) function linked to exercise-induced sudden cardiac death." *Cell* **113**(7): 829-840.

Word, T. A., A. P. Quick, C. Y. Miyake, M. K. Shak, X. Pan, J. J. Kim, H. D. Allen, M. Sibrian-Vazquez, R. M. Strongin, A. P. Landstrom and X. H. T. Wehrens (2021). "Efficacy of RyR2 inhibitor EL20 in induced pluripotent stem cell-derived cardiomyocytes from a patient with catecholaminergic polymorphic ventricular tachycardia." *J Cell Mol Med* **25**(13): 6115-6124.

Yamaguchi, Y., S. Cavallero, M. Patterson, H. Shen, J. Xu, S. R. Kumar and H. M. Sucov (2015). "Adipogenesis and epicardial adipose tissue: a novel fate of the epicardium induced by mesenchymal transformation and PPAR γ activation." *Proc Natl Acad Sci U S A* **112**(7): 2070-2075.

Yang, Y., D. M. Muzny, J. G. Reid, M. N. Bainbridge, A. Willis, P. A. Ward, A. Braxton, J. Beuten, F. Xia, Z. Niu, M. Hardison, R. Person, M. R. Bekheirnia, M. S. Leduc, A. Kirby, P. Pham, J. Scull, M. Wang, Y. Ding, S. E. Plon, J. R. Lupski, A. L. Beaudet, R. A. Gibbs and C. M. Eng (2013). "Clinical Whole-Exome Sequencing for the Diagnosis of Mendelian Disorders." *New England Journal of Medicine* **369**(16): 1502-1511.

Ying, L., M. Becard, D. Lyell, X. Han, L. Shortliffe, C. I. Husted, C. M. Alvira and D. N. Cornfield (2015). "The transient receptor potential vanilloid 4 channel modulates uterine tone during pregnancy." *Sci Transl Med* **7**(319): 319ra204.

Zhang, S., K. Lu, S. Yang, Y. Wu, J. Liao, Y. Lu, Q. Wu, N. Zhao, Q. Dong, L. Chen and Y. Du (2021). "Activation of transient receptor potential vanilloid 4 exacerbates myocardial ischemia-reperfusion injury via JNK-CaMKII phosphorylation pathway in isolated mice hearts." *Cell Calcium* **100**: 102483.

Zhang, Z., T. Q. Huang, I. Nepliouev, H. Zhang, A. S. Barnett, P. B. Rosenberg, S. I. Ou and J. A. Stiber (2017). "Crizotinib Inhibits Hyperpolarization-activated Cyclic Nucleotide-Gated Channel 4 Activity." *Cardioncology* **3**.

Zhao, Y., H. Huang, Y. Jiang, H. Wei, P. Liu, W. Wang and W. Niu (2012). "Unusual localization and translocation of TRPV4 protein in cultured ventricular myocytes of the neonatal rat." *Eur J Histochem* **56**(3): e32.

Biography

Robin Perelli completed her Bachelor of Arts degree at Cornell University in Linguistics and Near Eastern studies in May 2013. After working in the private sector, she obtained a master's degree from North Carolina State University in Physiology in June 2016. In 2016 she worked as a summer research assistant at the North Carolina State University School of Veterinary Medicine in Christopher Dekaney's laboratory, where she established a fluorescence in situ hybridization flow cytometry method to study acute intestinal injury and repair. Afterwards, she joined the laboratory of Jeremy Kay in the Department of Neurobiology at Duke University where she was the Duke Eye Center Microscopy Core manager and Research Technician. There, she investigated the effects of oxygen tension on astrocytes and blood vessels in the developing retina. She began her PhD at Duke University School of Medicine in August 2019 and joined the laboratory of Andrew Landstrom, where she studied the mechanisms of heritable arrhythmias and cardiomyopathies.